Experimentelle Physik

Alignment of ALICE TRD Modules Using Cosmic Ray Data

Diplomarbeit

von

Eva Sicking

Westfälische Wilhelms-Universität Münster
Institut für Kernphysik

— Februar 2009 —

Contents

1. Introduction

In 2009, the Large Hadron Collider (LHC) will presumably start its operation at the research center CERN[1] in Geneva. After the start-up of the LHC on September 10th 2008, an incident occurred nine days later which damaged a couple of segments of the collider, but a new start-up is already planned and currently scheduled for September 2009. Collisions of protons as well as collisions of lead-ions will be part of the LHC program for the next years.

ALICE[2] is one of six experiments at the LHC and it is especially designed for heavy-ion collisions. One of the most outstanding phenomena that can be studied via ALICE is the quark-gluon plasma (QGP), a state of matter assumed to have existed shortly after the Big Bang.

The QGP was searched for at the colliders AGS[3], SPS[4] and RHIC[5]. At AGS, nuclear matter was studied below the critical temperature. Later the experiments at SPS have found traces of a new phase, at RHIC further evidence of a new state of matter was found. The Large Hadron Collider (LHC) will permit collisions at particle energies that have never been reached before. Thus, it will allow insight into energy regions beyond SPS and RHIC.

One of the central detector components of ALICE is the Transition Radiation Detector (TRD). The main purposes of the TRD are the improved separation of electrons and pions and the reconstruction of their tracks. The cylindrical detector consists of eighteen super-modules which undergo final assembly in the institute for nuclear physics at Münster university. One super-module contains thirty independent detector chambers. As part of the assembly process, tracks of cosmic rays are recorded and reconstructed to provide an initial calibration of the detector modules.

Due to limited accuracy during assembly and due to time-driven deformations, the real position of the chambers can differ from their positions in the ideal geometry. In order to minimize a loss of accuracy during conversion of detector signals into spatial positions, the deviations have to be corrected. This increases the detector efficiency and the precision of the reconstructed tracks and vertices.

In this thesis, alignment procedures from the official alignment framework, applied to cosmic ray data taken in Münster, are described. Using straight tracks of cosmic rays, the correction of the module positions will be calculated. The success of the alignment

[1] CERN: European Organization for Nuclear Research.
[2] ALICE: A Large Ion Collider Experiment.
[3] AGS: Alternating Gradient Synchrotron, at the Brookhaven National Laboratory (BNL).
[4] SPS: Super Proton Synchrotron, CERN in Geneva.
[5] RHIC: Relativistic Heavy Ion Collider, BNL.

procedure will be evaluated by calculating the tracking resolution before and after aligning the sub-modules in the software framework. A method to calculate the tracking resolution will be introduced for this purpose. By selecting well-defined tracks for the alignment calculation, the procedures will be optimized.

In the following chapter, an introduction to the theoretical basics of high energy physics will be given. The Large Hadron Collider and the ALICE experiment will be discussed in Chapter 3, the Transition Radiation Detector will be described in Chapter 4. In the fifth chapter, the properties and composition of cosmic ray data will be presented. In addition, the Münster setup for the data taking of cosmic rays with a TRD super-module will be explained. In Chapter 6, an introduction to the standard tracking for ALICE and the stand-alone tracking algorithm for the TRD will be given. The topics of the seventh chapter are the alignment procedure, its application to cosmic ray data taken in Münster and the optimization of the procedure.

2. Theoretical Background

2.1 Basic Constituents of Matter

Already 400 B.C. it was assumed that all matter is made-up from basic constituents. When searching for these basic constituents of matter, smaller and smaller particles were found which appear to be divisible as well:
In the 19^{th} century it was discovered that all matter consists of atoms. About 100 elements were known, organized by their properties into a limited amount of groups, described by the periodic table. This gave a hint that atoms have an inner structure and are divisible. With the discovery of the electron and of radioactivity, a new way for the investigation of matter was found. In the early 20^{th} century, a scattering experiment of helium nuclei in a gold foil showed that the atom consists of a small nucleus with a cloud of electrons surrounding it. But the nucleus is also divisible: After the discovery of the neutron, the nucleus was found to be composed of protons and neutrons, the so-called nucleons.
In 1930, a new particle, the neutrino, was postulated to describe the β-decay of nuclei. Altogether four particles were known which could account for most observed phenomena of atoms and nuclei at that time: the proton, the neutron, the electron, and the neutrino. In the 1950s and 1960s, accelerator experiments discovered that protons and neutrons are just the most frequent representatives of many existing particles, the so called hadrons. Due to repeating properties of some hadrons, an inner structure was postulated, including smaller constituents, the so-called quarks. The quark model provided an answer about the composition of the hadrons. In the model, all hadrons consist of two or three quarks, which divides the hadrons in mesons and baryons [Pov04][MK02].

2.2 The Standard Model

In the *standard model* (SM), two kinds of particles, the quarks and the leptons, are the constituents of all matter, and four different forces describe the interaction between these particles. Within the model they are indivisible, point-like particles. The quarks and the leptons can be classified into three so-called generations, each containing two different particles. Table 2.1 shows all particles.

The six different quarks are called *up*, *down*, *strange*, *charm*, *top*, and *bottom* quark. They carry a color charge, named red, blue, or green, which is related to their strong interaction, and an electric charge of $-1/3\,e$ or $2/3\,e$. The leptons are divided into the *electron*, the *muon* and *tauon* with an electric charge of $-e$, and the related neutral neutrinos ν_e, ν_μ,

	Quarks			**Leptons**		
Generation	Name	Charge	Mass	Name	Charge	Mass
1	u	2/3 e	1.5 - 4 MeV/c^2	e^-	-e	0.511 MeV/c^2
	d	-1/3 e	4 - 8 MeV/c^2	ν_e	0	$\leq$ 3 eV/c^2
2	c	2/3 e	1.15 - 1.35 GeV/c^2	μ^-	-e	105 MeV/c^2
	s	-1/3 e	80 - 130 MeV/c^2	ν_μ	0	$\leq$ 0.19 MeV/c^2
3	t	2/3 e	174.3 $\pm$ 5.1 GeV/c^2	τ^-	-e	1.78 GeV/c^2
	b	-1/3 e	4.1 - 4.4 GeV/c^2	ν_τ	0	$\leq$ 18.2 MeV/c^2

Table 2.1: Quarks and leptons in the Standard Model [Ams08].

and ν_τ. Each of these twelve particles also has an anti-particle. Altogether 24 particles are nowadays seen as the basic constituents of matter.
The four existing and known fundamental forces are the *gravitation*, the *weak* and the *strong nuclear forces*, and the *electro-magnetic force*. Each force is mediated by its force carriers. The force carriers of the Standard Model are *gauge bosons*. The SM describes the weak and strong nuclear force and the electro-magnetic force, but not the gravitation. The forces and their gauge bosons are listed in Table 2.2.

Force	relative Strength	Gauge Boson	Applies on
Strong nuclear	1	Gluons	Quarks
Electromagnetic	$\sim 10^{-2}$	Photons	All charged particles
Weak nuclear	$\sim 10^{-7}$	$W^{\pm}, Z^0$	Quarks, leptons
Gravitation	$\sim 10^{-39}$	Gravitons (?)	All massive particles

Table 2.2: The fundamental forces in the Standard Model and the gravitation. The graviton as an gauge boson of the gravitation is only postulated but not found.

2.3 The Quark-Gluon Plasma

The interaction between quarks is strong at large distances and weakens at smaller ones. These two phenomena are called *confinement* and *asymptotic freedom*. At low temperatures and low densities, the strongly interacting partons, quarks and gluons, are confined in a small space region inside hadrons. When the temperature and/or the density of nuclear matter becomes very high, the partons transform into a deconfined phase of matter,

called *quark-gluon plasma* (QGP) [Sta07].
Figure 2.1 shows the phase diagram of nuclear matter. The axes are the temperature T and the chemical potential μ_b, which is a measure of the net baryon density ρ. ρ is defined as the number of baryons minus the number of anti-baryons per volume unit [Eck05]. If μ_b increases, so does ρ.
According to quantum chromodynamics, the theory of the strong force, a phase transition from hadronic to partonic matter should occur at a critical temperature T_c and energy density ε_c. The confined partons become quasi-free. For $\mu_b = 0$, the transition temperature from nuclear to partonic matter can be estimated as $\sim$ 170 MeV [PPR04]. One phase diagram is presented in Figure 2.1. The solid lines indicate first-order phase transitions, while the dashed line indicates a possible region of a continuous but rapid, so-called *crossover*, phase transition. The circle in between gives the second-order critical endpoint of a line of first-order transitions. The experiments at LHC are predicted to generate a high-temperature, low-density QGP, which will freeze out on the crossover phase transition.

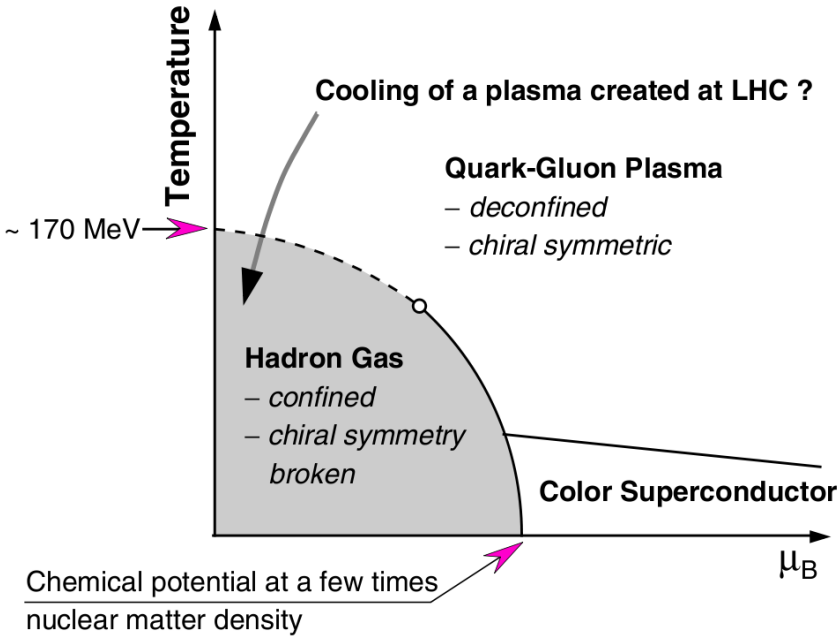

Figure 2.1: The phase diagram of QCD: the solid line indicate expected first-order transition. The dashed line indicates a possible region of a continuous but rapid crossover transition. The open circle gives the second-order critical endpoint of a line of first-order transitions, which may be located closer to the $\mu_B = 0$ axis [PPR04].

2.4 Generating the QGP in Heavy-Ion Collisions

According to today's accepted theories, shortly after the big bang quarks and gluons were free in the quark-gluon plasma. While the universe expanded and cooled down, the partons combined to hadronic matter.
Today the average temperature and density in the universe are much lower. One opportunity to study the QGP with its properties is to produce such a state of matter in heavy-ion collisions. In these collisions, a shortly living *fireball* is produced, in which high densities and temperatures can be reached. In order to interpret the generated system and its behavior as the behavior of the QGP, the system under consideration must not only behave like individual elementary particles or a group of elementary particles. Therefore the collision particles should consist of a large number of particles, such that the medium in the fireball reaches an equilibrium state [Sta07].
So collisions can give evidence on the properties of nuclear matter, explain the phase diagram of nuclear matter, and also give hints on the evolution of the universe.
In Figure 2.2, a simulated collision between two nuclei is shown, divided into four steps of time evolution. In panel 2.2(a) the Lorentz contracted nuclei flying towards each other are shown. In panel 2.2(b) the collision is shown where the partons collide and the nuclei penetrate each other. The QGP can be generated in the region between the diverging fractions of the nuclei as shown in panel 2.2(c). The partons freeze out and combine to hadrons, this is shown in panel 2.2(d). Overall a huge amount of hadrons, leptons, and photons is emitted in the collision.

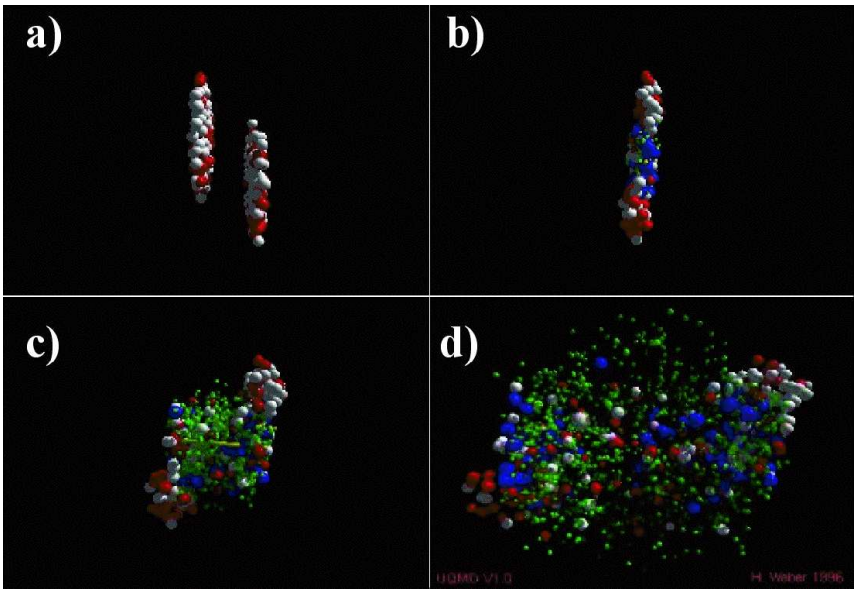

Figure 2.2: Simulation of the time evolution of a collision between two heavy nuclei. Due to the Lorentz–contraction the two nuclei appear as two thin discs in the laboratory frame [Web96].

2.5 Signatures of the QGP

In order to investigate the QGP, many observables in a heavy-ion collision are measured and combined to an overall picture of the collision. Some observables which can be measured with ALICE are multiplicity, spectra and correlations of particles, fluctuations, jets, and direct photons. Furthermore dileptons, and heavy quark and quarkonium production can be observed.
A short overview of some of the most promising signatures of the QGP is given in the following. But not only one signature is able to identify the QGP. Only the composition of all observables enables to identify the QGP and to estimate properties of it.

Quarkonia Modification
In nuclear collisions, pairs of charm quarks ($c\overline{c}$) and bottom quarks ($b\overline{b}$) can be produced. The production rates scale with the number of binary collisions.
The pairs can combine to quarkonia states, for example $c\overline{c}$ combine to J/Ψ. The charmonium states are bound by energies of the order of a few hundred MeV. These binding energies are comparable with the mean energies of the plasma. This implies that the probability for charmonium to break up is very large within this medium. The plasma screens the interaction between the $c\overline{c}$ pair, the two quarks dissolve in the medium and are likely to combine with any other quark of the plasma at freeze-out. Light quarks like u, d and s are more likely to be produced in the collision than heavier quarks, thus instead of combining to a charmonium again, D-mesons with open charm are created [Mat86]. The suppression of J/Ψ production as an evidence for the deconfinment of quarks and gluons was already measured in the year 2000 with the NA50 experiment in Pb-Pb collisions at the CERN-SPS [Abr00] and in the year 2005 with the PHENIX[1] experiment at RHIC [Adc05]. At higher collision energies, reachable at LHC, many more $c\overline{c}$ pairs will be produced. Therefore it is possible that charm quarks from different origins form a charmonium [Sta07]. For bottomonium a suppression is expected for LHC energies [PPR04].

Open heavy flavor production
With a measurement of open charm and open bottom, such as D and B-mesons, the absolute cross section of charm and bottom production can be estimated. It is possible to measure the leptonic component of their decays and the hadronic decay channels. The results can also be used as baseline measurement for the quarkonia suppression.

Strangeness Enhancement
Kaons are the lightest strange particles. Because of the conservation of strangeness in the

[1] PHENIX: Pioneering High Energy Nuclear Interaction eXperiment.

strong interaction, only pairs of strange particles can be created. The amount of energy required for the production of a pair of Kaons is 987 MeV.
In the QGP $s\overline{s}$-pairs can be created directly with a required energy of comparably low 300 MeV, the mass of $s\overline{s}$. The s and the $\overline{s}$ will recombine with other quarks to form strange particles. The number of strange particles increases [PPR04].

Jet Quenching
Since the QGP is a strongly interacting medium, quarks or gluons traveling through the quark-gluon plasma lose more energy than they would lose through hadronic matter. In heavy-ion collisions, amongst others, a pair of very energetic quarks or gluons can be produced in early hard scattering processes. Both partons travel in opposite azimuthal direction. These pairs of particles propagate through the medium produced in the collision and loose energy or are completely absorbed. Those partons fragment into jets. By detecting and studying the attenuation of these jets, information about properties of the produced medium can be extracted [PPR04].

Photons
Photons as well as leptons do not interact strongly with the QGP. If the particles are created before or at the formation of the QGP, they provide a look into this early phase of the collision. The spectrum of photons is built of thermal photons from black body radiation of the hot matter generated in the collision and of prompt photons from hard processes of the collision.
The photons can be directly measured in calorimeters of ALICE or by measuring e^+e^- pairs produce due to conversion of these photons [PPR04].

3. LHC and ALICE

3.1 The Large Hadron Collider (LHC)

The Large Hadron Collider (LHC) is a particle accelerator at the European Organization for Nuclear Research (CERN) research center in Geneva, Switzerland. Currently being commissioned it will presumably start operation in summer 2009. It will then be the largest particle accelerator ever built on earth.

LHC is an accelerator ring with a circumference of 26.659 kilometers, located up to 100 meters underneath earth's surface. It is made of eight arcs and eight access points some of which serve as experimental areas. At four of these points the experiments are placed [LHC08].

The LHC comprises of two beam pipes designed to accelerate particles in opposite directions. At four interaction points, the beams cross and accelerated particles can be collided. Protons will clash with a center of mass energy[1] of up to 14 TeV per proton (p) pair and lead ions (Pb) with a maximum of 5.5 TeV per nucleon pair. In comparison to RHIC, today's leading heavy ion accelerator, the LHC has a center of mass energy 30 times higher and therefore opens the way to new physical discoveries.

The LHC dipole magnets become superconducting below a temperature of 10 K. Cooled with helium to 1.9 K and with a current of 11 700 A a magnetic field of 8.3 T is generated [LHC08].

The particles circulate around the ring in well-defined bunches. In the final configuration each beam will consist of 2808 bunches of particles and each bunch will contain in average 100 billion particles. But per bunch crossing only about 20 collisions between these 200 billion particles will occur. Bunches will cross on average about 40 million times per second, so the LHC will generate up to 600 million particle collisions per second. The design luminosity of the LHC is $10^{34}\mathrm{cm}^{-2}\mathrm{s}^{-1}$ for p+p collisions. The generated particles can pass several selection criteria with triggers. The remaining tracks are reconstructed in the experiments [LHC08].

At LHC there are four main experiments to examine various physics topics. Their positions at the LHC are presented in Figure 3.1. The main aim of the CMS[2] and ATLAS[3] experiments is to find the Higgs boson, the particle supposed to generate mass according to the standard model. In addition, they search for particles predicted by supersymmetric

[1] The energy in a collision is measured by the energy of the two colliding particles in their center of mass system, in the case of colliding protons expressed by $\sqrt{s}$ and in the case of ions the energy is given per nucleon pair and given by $\sqrt{s_{\mathrm{NN}}}$.

[2] CMS: Compact Muon Solenoid.

[3] ATLAS: A Toroidal Lhc ApparatuS.

extensions of the standard model.
The LHCb[4] investigates CP-violating processes with b-quarks. These three experiments use p+p collisions for their measurements. ALICE, the experiment discussed in this thesis, is optimized for investigation of strongly interacting matter, the phase transition of matter to the quark-gluon plasma (QGP), the phase diagram of nuclear matter and its physics. The measurements will be done mainly with Pb+Pb collisions. p+p collisions will provide a reference measurement.
TOTEM[5], a smaller fifth experiment, will measure the total cross section, elastic processes and diffractive processes of LHC collisions. It shares an interaction point with the CMS.
LHCf[6] is the sixth experiment at LHC. It will measure particles produced very close to the direction of the beams in the proton-proton collisions at the LHC. It is placed near ATLAS.
Beside of the experiments' main topics, cosmic rays can be measured simultaneously. Thus all LHC experiments can generate new results for astrophysics, especially for cosmic ray interactions at high energies [PPR04] [LHC08].

3.2 A Large Ion Collider Experiment - ALICE

ALICE is able to identify hadrons, leptons and photons over a wide range of particle momenta and at high particle densities. It also allows to reconstruct short lived particles and their decay vertices. The setup of ALICE is shown in Figure 3.2.
ALICE will perform measurements in both p+p and Pb+Pb collisions. The p+p-collisions can be used as reference data for the Pb+Pb collisions but are also interesting in their own right.
In Figure 3.2, a schematic picture of ALICE can be seen. The experiment is built at the so-called Point 2 experimental area in the French town St. Genis-Pouilly. ALICE consists of different detector components. They can be divided into three main groups: the detectors in the so called central barrel, the Muon spectrometer and the forward detectors.
Beginning with the detectors placed in the central barrel, which are the detectors at central rapidity, the components are described in the order of radial position in the following:
The Inner Tacking System (ITS) consists of six layers of high resolution silicon detectors. It is divided into Silicion Pixel Detectors (SPD), Silicon Drift Detectors (SDD) and Silicon Strip Detectors (SSD). The main tasks of the ITS are to localize the primary and secondary vertices with high precision. Also tracking and particle identification are

[4]LHCb: Large Hadron Collider beauty experiment.
[5]TOTEM: Total Cross Section, Elastic Scattering and Diffraction Dissociation.
[6]LHCf: Large Hadron Collider forward.

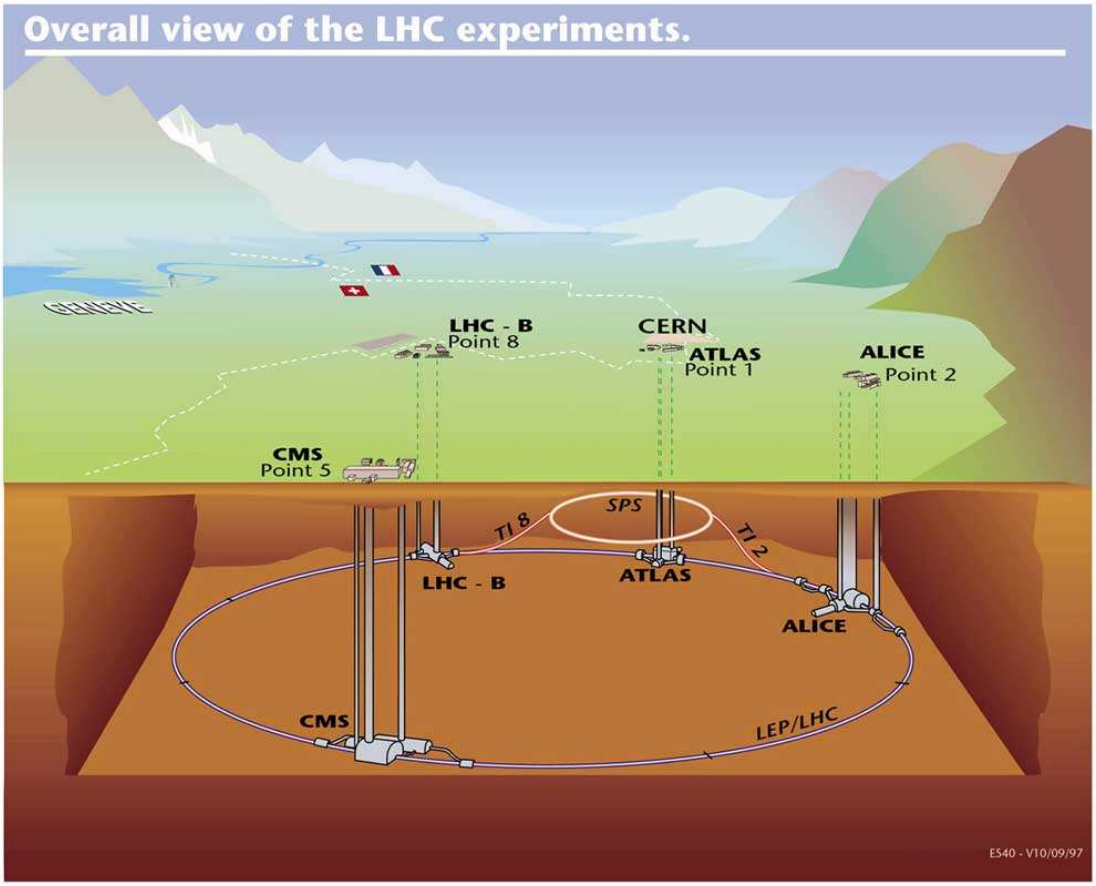

Figure 3.1: Overall view of all LHC experiments [CDS09].

provided by the ITS. The results are combined with results of other detector components to improve spatial and momentum resolution of the tracking.
The next component in radial direction is the Time Projection Chamber (TPC) representing the main tracking detector. Combined with other detectors it provides charged particle momentum measurements. Especially a good two-track separation, particle identification and vertex determination were considered during the design of the TPC.
The Transition Radiation Detector's (TRD) main aim is the separation of electrons and pions. The TRD also works as a tracking detector. As the TRD is in the focus of this thesis, the TRD and its functionality will be explained in more detail in Chapter 4
The Time Of Flight (TOF) detector identifies particles by recording the transit time between the interaction point and the detector surface. Its time resolution is better than 100 picoseconds. Especially π, K and p will be measured with this detector.

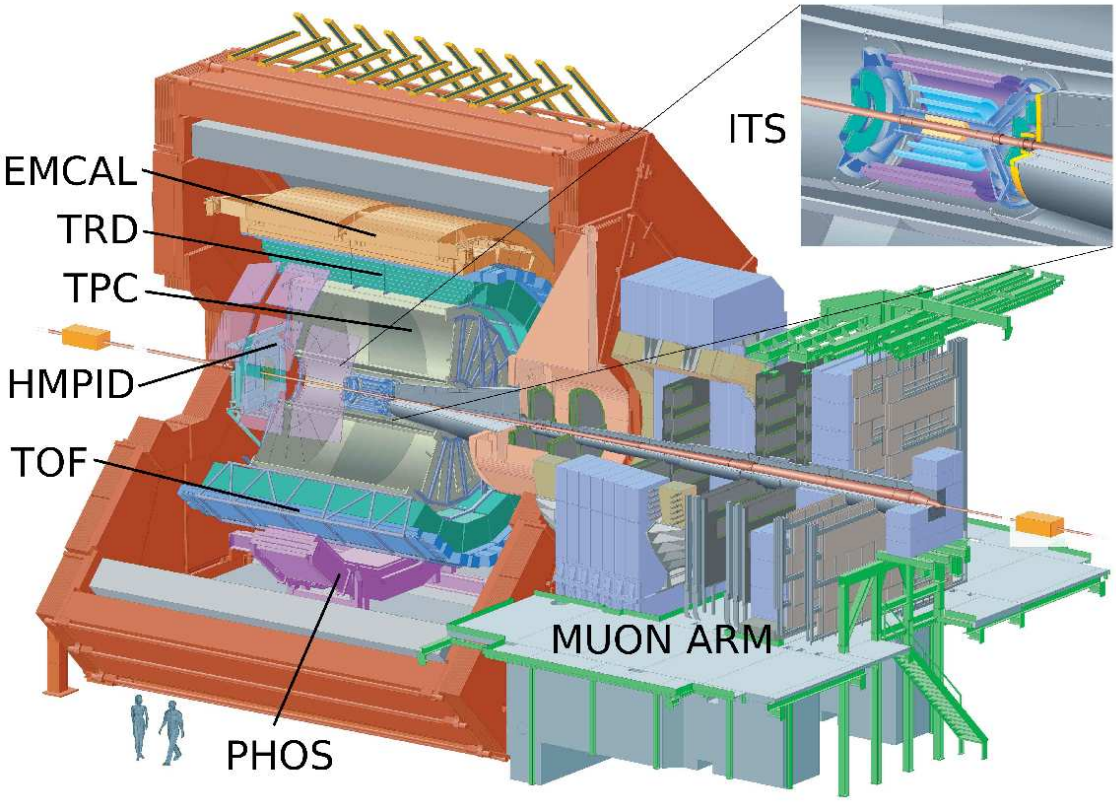

Figure 3.2: Schematic view of the ALICE detector [ALI09].

The detector components described so far have full azimuthal coverage at central rapidity[7] ($|\eta| \leq 0.9$). They are placed within the L3 magnet.
The L3 Solenoid magnet is operated at room temperature. It is an octagonal steel yoke with an aluminum coil and can be closed by pole cap doors. With an operating current of 30 kA a magnetic field of 0.5 T can be generated. The central barrel is covered by a nearly homogeneous magnetic field. Due to the Lorentz force bending charged particles in a magnetic field, it is possible to measure the momentum of the particles.
In addition to the components in central barrel described so far, there are detectors covering small sections in ϕ. One detector is the High Momentum Particle Identification Detector (HMPID) for identification hadrons with $p_{\mathrm{T}} \geq 1 \frac{\mathrm{GeV}}{\mathrm{c}}$. With HMPID the overall particle identification (PID) capability of ALICE at high particle momenta is enhanced.
An electromagnetic calorimeter is the Photon Spectrometer (PHOS) built of high density crystals. The thermal and dynamical properties of the initial collision phase can be measured. This is done via measurements of low-p_{T} direct photons. Jet quenching can be

[7] For ultra relativistic particle the rapidity y can be approximated with the pseudorapidity η. It can be calculated by $\eta = -ln[\tan \frac{\theta}{2}]$, while θ is the angle between the momentum $\overrightarrow{p}$ and the beam axis. It can also be expressed in $\eta = \frac{1}{2} ln[\frac{|\overrightarrow{p}|+p_L}{|\overrightarrow{p}|-p_L}]$. Here p_L is the longitudinal component of the momentum.

observed with the measurement of high-p_T π^0 and γ-jet correlations.
The Electromagnetic Calorimeter (EMCal) is a Pb-scintillator sampling calorimeter. It is mounted on the magnet coil and covers $|\eta| \leq 0.7$ and $\triangle\phi = 107°$. It is placed almost opposite in azimuthal to the PHOS calorimeter. The construction has started in 2008.
ALICE COsmic Ray DEtector (ACORDE) is placed on top of the L3 magnet. It is an array of plastic scintillator counters, which provides a trigger signal for the tracking detectors in case of a cosmic shower.
To measure the initial collision geometry the Photon Multiplicity Detector (PMD) and Forward Multiplicity Detectors (FMD) are used. The PMD measures the multiplicity and spatial distribution of photons in the forward rapidity of $2.3 \leq \eta \leq 3.7$. With this information an estimation about transverse electromagnetic energy and the so called reaction plane can be made.
The FMD is designed to measure the charged particles produced in the collisions and emitted at small angles relative to the beam direction. It is the primary detector to measure the multiplicity of charged particles produced in the interaction in forward direction.

The Muon Spectrometer with its own dipole magnet is placed along the beam line in negative direction on the z-axis. It covers a pseudo-rapidity region of $-4.0 \leq \eta \leq -2.5$. It consists of an absorber, four Muon Trackers, a Muon Filter (Wall) and a Muon Trigger. It is placed around the dipole magnet.

To measure the initial configuration of a collision, the Zero Degree Calorimeter (ZDC) is used. Two ZDCs are placed 115 meters away from the interaction point (one for each direction of the z-axis). On each side are two detector components to measure neutrons and protons. With the ZDC it is possible to measure the energy and the number of spectators, particles which have not interacted in the collision. This helps distinguishing between central and peripheral collisions and measuring the centrality.
The V0 and T0 detectors measure – as the FMD – the number of particles produced in the collision and their spatial distribution. The T0 also measures the interaction time and provides the start time to the TOF detector [PPR04, TP108].

3.3 The ALICE Research Program

ALICE is supposed to investigate the phase diagram of nuclear matter and the quark-gluon plasma. This is done by measuring a variety of physics observables:
Global event characteristics such as particle multiplicity, the centrality of the collision, the energy density and the nuclear stopping will be measured. With so called soft physics measurements, the chemical composition of the created particles at the time of chemical

freeze-out will be analyzed. This is done by observing the particle and resonance production, the particle ratios and spectra and the strangeness enhancement. Furthermore, reaction dynamics like the transverse and the elliptic flow, Hanbury-Brown-Twiss correlations and event by event dynamical fluctuations are measured. Jets and direct photons are hard probes, allowing studies on initial conditions of the collision and on the created medium and its response to traversing particles. Last but not least heavy flavors are under investigation to make statements about the QGP. Therefore quarkonia, open charm and open beauty production are measured.
There will also be a p+p and a p+Pb program. These are necessary as reference data for better interpretation of heavy-ion collisions. In addition, ALICE will have stand alone detailed p+p studies [PPR04].

4. The ALICE Transition Radiation Detector

4.1 Tasks and Requirements

Many observables of the QGP require the correct identification and reconstruction of electrons in the large pion background produced in a heavy-ion collision. For an improved separation of electrons and pions, the Transition Radiation Detector was added to the ALICE setup [TRD99].
The measurement of electrons enables the study of production of light and heavy vector mesons, the continuum of the di-electrons, semi-leptonic decays of hadrons with open charm and open beauty, and the correlation of $D\bar{D}$ and $B\bar{B}$ pairs. In addition, jets with high E_T can be measured with the TRD.
In order to provide precise measurements, special design considerations are made: The pion rejection capability should reach a factor of 100 for particles with momenta above 1 GeV/c. The position resolution should be good such that the momentum resolution reaches a level of 5 % for particles with 5 GeV/c [PPR04]. The radiation length of the TRD has to be minimized in order to reduce bremsstrahlung leading to incorrect momentum determination. In addition, the probability of photon conversions is reduced with reduced radiation length, which is especially important for the measurements of EMCal, PHOS, and TOF. In order to take measurements at high multiplicities of about $\mathrm{d}N_{\mathrm{ch}}/\mathrm{d}\eta = 8000$ as an upper limit, the detector granularity should be high. The granularity in bending direction defines the transverse momentum resolution [TP108].
The TRD has a pseudorapidity coverage of $-0.84 \leq \eta \leq 0.84$ and an azimuthal coverage of 360°. Its radial position is between $2.90 \leq r \leq 3.68$ m [TP108].

4.2 Transition Radiation

Transition radiation (TR) is produced by charged particles when they cross the interface of two media of different dielectric constants. The probability of a particle to generate TR depends on the ratio of its energy to the rest energy of a particle. The ratio is called relativistic Lorentz factor

$$\gamma = \frac{E}{m_0 \cdot c^2}. \tag{4.1}$$

Particles with $\gamma > 1000$ have a high probability to generate detectable TR. For electrons and positrons with a rest energy of 511 keV this is an energy of 511 MeV, for $\pi^{\pm}$ it is about 140 GeV [Ams08]. Mainly particles within the energy range of 1-100 GeV originating from

collisions, are important for the interpretation of the data. In this energy range just the $e^{\pm}$ generate TR. Therefore the TR can be used as additional information in the particles identification (PID).
The more interfaces are crossed, the higher is the probability of a relativistic particle to produce TR. Detectors which are using the TR for particle identification have therefore so-called radiators composed of many thin layers or of inhomogeneous material.
Furthermore the wave length of the generated radiation depends on the velocity. Particles with low velocities generate TR with wave lengths in the absorption range of the radiator materials. Particles with $\gamma > 1000$ generate TR consisting of gamma ray photons, which can penetrate and leave the medium. It is possible to detect these X-rays in the region beyond the radiator.

4.3 TRD Layout

The Transition Radiation Detector is divided into 540 chambers, which are the smallest independent detector components of the TRD. The detector is arranged cylindrically around the beam line, which represents the z-axis. It is divided into 18 segments in the ϕ direction, which is the angle around the beam line. One of these segments is called TRD super-module. Each super-module consists of 30 chambers with five stacks arranged in z direction and six chambers in each stack. Figure 4.1 shows the whole TRD with a super-module and a chamber displaced to clarify the layout. The figure also shows a photo of a half assembled super-module, taken in the assembly hall in Münster.

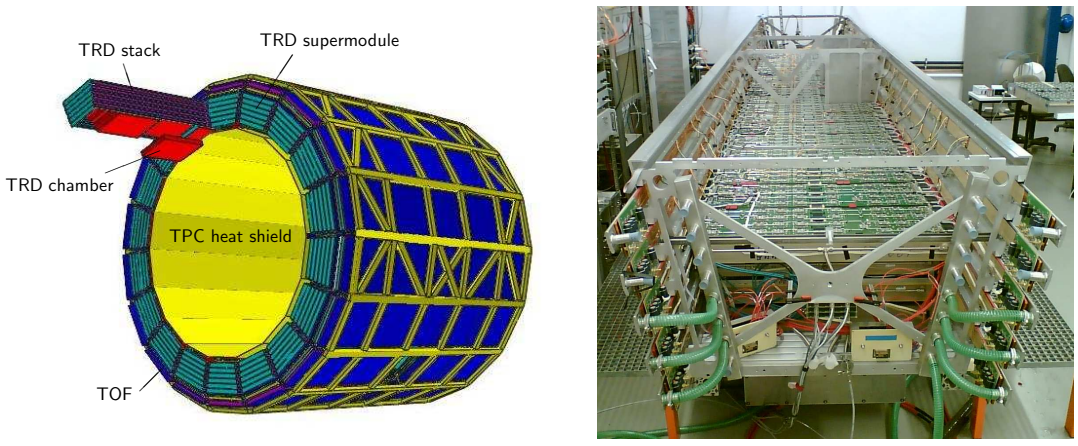

Figure 4.1: Left panel: Schematic view of the TRD in the ALICE space frame. The detector consists of 18 super-modules. Each contains 30 readout chambers, arranged in 5 stacks and 6 layers. The TRD is surrounded by the TOF detector. Inside the TRD, the TPC is placed [TP108]. Right panel: One super-module during assembly in Münster. Three layers are installed.

4.4 TRD Chamber Layout and Operation Principle

Figure 4.2 shows a cross section of a TRD chamber. Each detector chamber consists of a sandwich radiator, a drift region, and a multi-wire proportional chamber section with pad readout. The pad plane is supported by a honeycomb carbon-fiber sandwich back panel. The read out electronics is directly mounted on the back panel. With the water cooling system on top, the total thickness of a chamber is 125 mm [TP108].

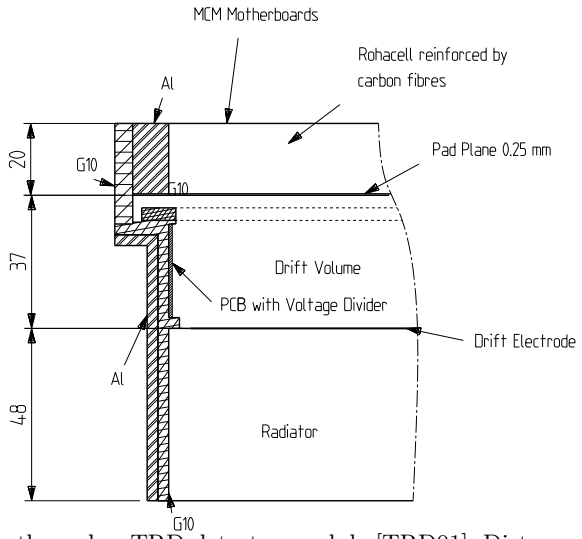

Figure 4.2: Cross section through a TRD detector module [TRD01]. Distances are given in mm.

4.4.1 Radiator

On one hand the radiator of the TRD has to provide a high transition radiation yield and on the other hand mechanical stability. It is constructed in a sandwich design consisting of polypropylene fiber mats and Rohacell foam sheets. The mats are 3.2 cm thick. Above and underneath the mat, two foam sheets, each of 0.8 cm thickness, are placed. Relativistic particles produce in average 1.45 X-ray photons of Transition Radiation (TR) when traversing the interfaces of the radiator [TRD01].

4.4.2 The Readout Chamber

The readout chamber is a time projection chamber (TPC), build out of a drift region and a multi-wire proportional chamber. The drift electrode is on the backside of the radiator. The drift region is 30 mm long, it ends at the cathode-wires. The electrical drift field is 700 V/cm. The amplification region reaches from the anode wires to the pad plane. On the side of the back panel facing the gas volume, the readout pads are placed. The readout pads have a rhomboid shape with an average area of about 6 cm^2. In average the extent of the pads in z direction is 8.8 cm and in y direction it is 0.7 cm [TRD01]. The

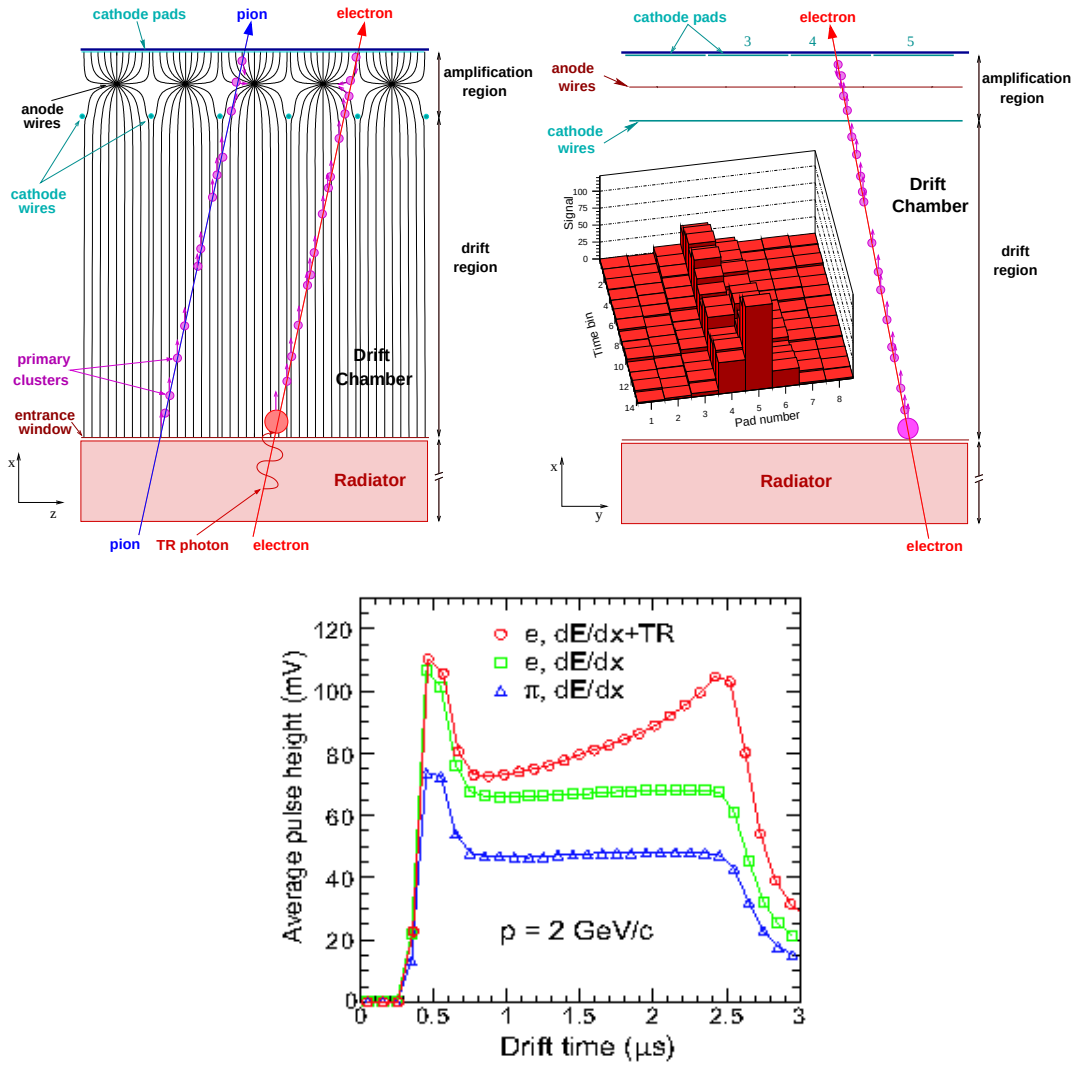

Figure 4.3: Top left panel: basic setup of an ALICE TRD chamber in rz direction crossed by an electron and a pion. Only the high energetic electron generates transition radiation in the radiator. This is part of the principle of particle separation of the TRD [TRD01]. Top right panel: a detector module in $r\phi$ direction. Bottom panel: average pulse height as function of the drift time for pions (triangles) and electrons without radiator (squares) and electrons with radiator (circles) for 2 GeV/c particles [TP108].

central chamber of a layer consists of 12, the others of 16 pad rows in z direction. Each pad row is built out of 144 pads in $r\phi$ direction.

The upper panels of Figure 4.3 show the basic setup of a TRD chamber traversed by a pion and an electron in rz and $r\phi$ projection. The drift volume is filled with a gas mixture of Xe/CO_2(85 %/15 %). The charge number of xenon is very high. Thus the radiation length for X-ray photons in the gas is low comparable to the length of the drift region.
The incident particles ionize the counting gas and produce transition radiation in the

radiator if it exceeds the threshold of $\gamma > 1000$ [TRD01]. In Figure 4.3, this is the case for the electron. The produced X-rays ionize the high-Z counting gas efficiently. The TR ionizes the counting gas in the drift region, too [TRD01]. All electrons originating from ionization processes drift towards the cathode wires and enter the amplification region. After gas amplification in the surroundings of the anode wires the signal is induced on the read-out pads.
The charge signal is recorded as a discrete function of time as described in the top left panel of Figure 4.3. Here all ionization electrons from the drift region are detected as a function of time, which is converted to the place of formation via the nearly constant drift velocity. Afterwards, in the track reconstruction, the time information can be converted to a radial position of the formation of the signal. The y and the z position of the particle at a given time can be calculated by the positions of the pads, where the signal is induced. The average pulse height for particles of 2 GeV as function of time is presented in the bottom panel of Figure 4.3. After an amplification peak, which represents the charge coming from underneath and above the anode wire, the signal of the drift plateau is visible. The pulse height is plotted for electrons and pions, for electrons it is shown with and without the TR speak. Electrons lose more energy on average, which can be explained with the Bethe-Bloch equation [Ams08]. The separation of electrons and pions is based on the deposited charge. In addition, the time information can be exploited in order to improve the electron identification. With likelihood methods and neural networks, the electron probability of each single particle is calculated [And04, Wil06].
Combining the information, the track of the particle can be reconstructed and also the particle species can be determined.

Pad Response Function

In order to enhance the precision in position resolution, the information of several pads with independent charge readout can be combined. The electrons produced in the process of ionization are collected at the anode wires and induce a detectable signal in the divided pad plane. The detected charge of particle tracks is distributed over more than one pad. In order to calculate the coordinates of the trajectory of the particle, the measured signals of the pads can be converted. An empirical formula for the induced charge distribution describes the average behavior in symmetric MWPCs along the anode wire. This method is called Mathieson formalism, it results in the so-called pad response function (PRF) [Adl04, TRD01]. Figure 4.4 shows the measured PRF with a Gaussian fit for the pads in a TRD layer [Wul09].

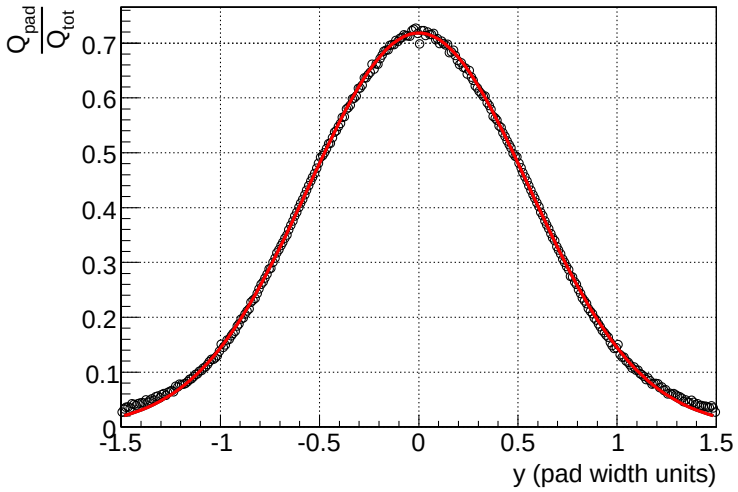

Figure 4.4: The pad response function for a TRD layer with a pad width of W = 6.35 mm [Wul09].

Time Response Function

The shape of the signal is influenced by the electronics and by the drift chamber itself. An overall time response function (TRF) describes the output of the chamber and its electronics.
Traversing particles ionize the counting gas. The electrons drift to the amplification region and are measured as explained in Chapter 4.4.2. In addition, the following aspects influence the shape of the signal: The remaining ions generate a space charge, which generates so-called *ion tail* in the detected signal. The electrons do not drift isochronally, their drift time and velocity depend on the transversal distances of the electrons to the anode wires. The response of the preamplifier shaper implemented in the multi chip modules changes the shape of the generated signal.
The sum of these effects results in the absolute time response. Figure 4.5 shows a result of a simulation [TRD01]. The signal is non-Gaussian because of the ion tail and shaping in the electronics.

4.4.3 Front-End Electronics

An overview of the front-end electronics is presented in Figure 4.6.
The readout of the ALICE TRD is processed with more than a million channels. In order to handle the information of the channels, devices such as a charge sensitive PreAmplifier/ShAper (PASA), an analog digital concerter (ADC), and digital circuitry where data are processed and stored in event buffers for subsequent readout are used. The data processing is performed during drift time by the Tracklet PreProcessor (TPP) in order to prepare the information necessary for the Tracklet Processor (TP). At the end of the drift

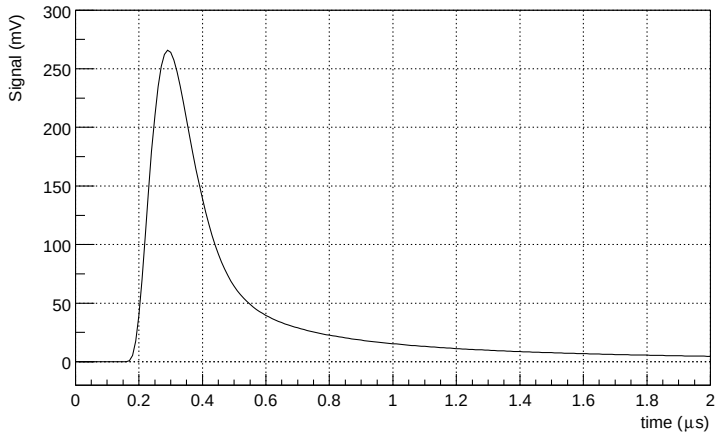

Figure 4.5: The time response function [TRD01].

time, the Tracklet Processor, a micro CPU implemented as Multiple Instruction Multiple Data (MIMD) processor operating at 120 MHz, determines potential tracklets. These tracklets are shipped to a Global Tracking Unit (GTU), which combines them to tracks and processes the trigger information for the TRD [TRD01].

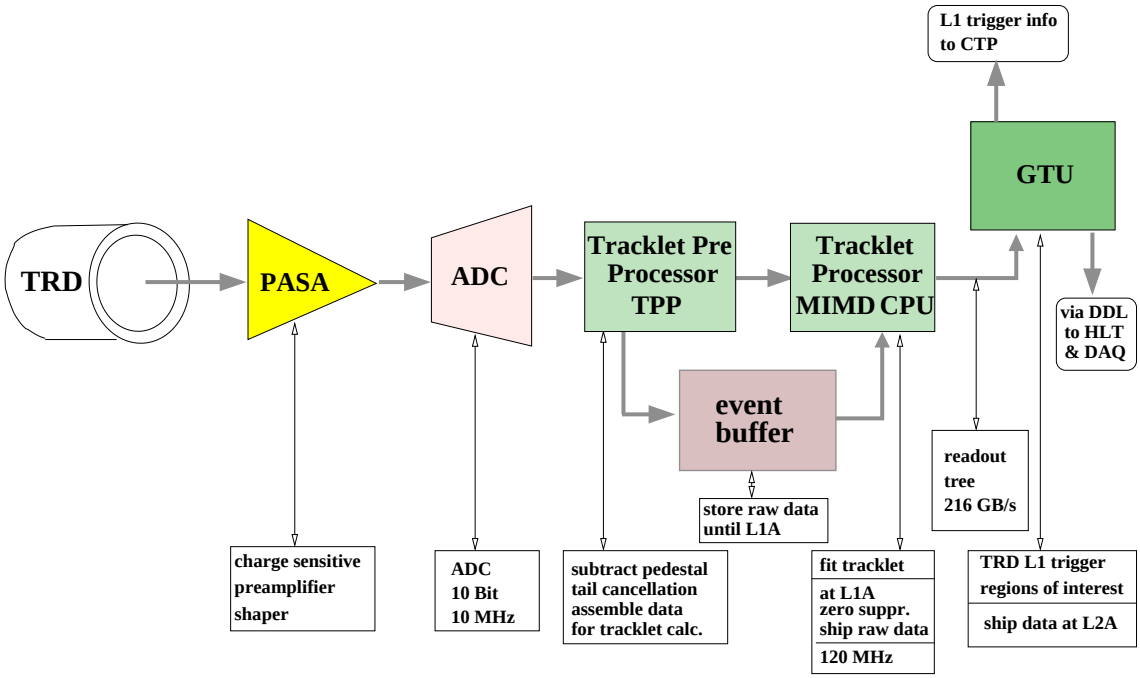

Figure 4.6: Schematic overview of the readout electronics of the TRD [TP108]. All components except the GTU are placed on the TRD chambers. The ADC, the TPP, the event buffer, and the MIMD CPU are combined to one chip, which determines the tracklets of the chamber. Therefore the chip has the function of the local tracking unit (LTU).

5. Calibration of Super Modules with Cosmic Rays

5.1 Cosmic Rays

Cosmic rays can be divided into *primary* cosmic rays, which come from the space and hit the terrestrial atmosphere, and *secondary* cosmic rays, which are produced in the interaction of primaries with atmospheric particles [Ams08].

5.1.1 Primary Cosmic Rays

Primary cosmic rays mainly consist of protons, electrons, helium, as well as ions and nuclei of carbon, oxygen, iron and other end products of stellar nucleosynthesis. About 79 % of the primary nucleons are protons and about 70 % of the rest of them are nucleons bound in helium nuclei [Ams08]. The exact composition is energy dependent. Beside particles from the sun, the main part of these so-called primaries comes from outside of the solar system. They have a half-life in the order of million years or longer and are accelerated at astrophysical sources.
The flux of the primary cosmic radiation is on average constant in the universe, but close to earth it alters. This is due to the influence of magnetic fields on the trajectories of the particles. The incoming particles are mainly influenced by the solar wind when entering the solar system. Due to this magnetized plasma the particles can be decelerated, which leads to an exclusion of low energy particles. They do not reach the inner solar system and thus the earth's atmosphere. In addition, the magnetic of the earth field affects the cosmic rays. Low energy particles do not manage to penetrate this field, thus they do not reach the top of the atmosphere. Since the solar and the terrestrial magnetic field alter as a function of time and location, the spectra of the primary cosmic radiation reaching the top of the atmosphere depend both on time and location. For example, the magnetic field of the rotating earth is shaped by the solar wind. The main part of the terrestrial magnetic field has therefore a cycle of 24 hours. The solar activity has an alternating cycle of eleven years, which can be observed by watching the sunspots. Due to interaction with the atmospheric gas, the remaining primaries barely reach the surface, but some particles still do.

The differential energy spectrum multiplied by $E^{2.7}$ for all particles of the primary cosmic rays is shown in Figure 5.1. With the scaling, different steepnesses within the spectrum are better visible. The shape of the spectrum can be described with the power

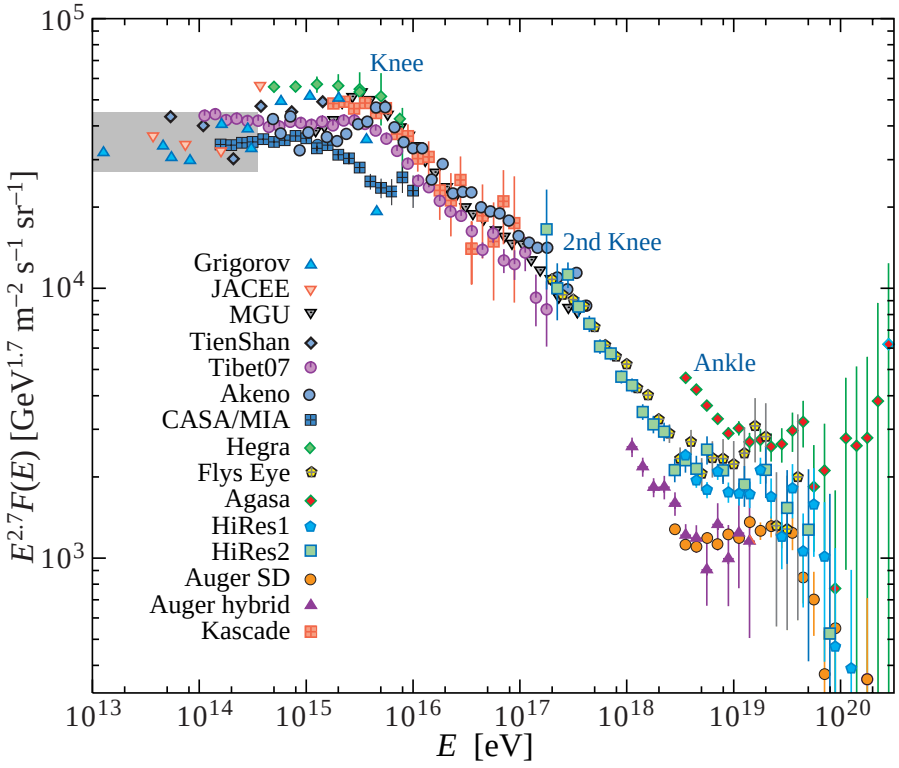

Figure 5.1: The all-particle spectrum from air shower measurements. The shaded area shows the range of the direct cosmic spectrum measurements [Ams08].

law in Equation 5.1:

$$\frac{\mathrm{d}N}{\mathrm{d}E} = \text{const} \cdot E^{\gamma}. \tag{5.1}$$

For different energy ranges, different values of the exponent γ, the so-called spectral index, describe the spectrum. The spectrum has a kink at 10^{15} to 10^{16} eV, which is called *knee*. The spectral index γ changes with increased energy at this point of the spectrum from 2.7 to 3.1. At higher energies, around 10^{17} to 10^{18} eV, a further kink, the *second knee*, occurs. The kink at 10^{19} eV is called *ankle*.

The origin of these changes in the spectral index are not completely understood. One of several attempts to explain this behavior is the following: the cosmic radiation of the different parts of the spectrum can have different origins. The main part of cosmic particles with energies below the knee could originate from galactic sources, whereas the particles having energies above the knee come from extragalactic ones. Particles with energies above the ankle could probably be suppressed, because such energetic particles interact with the photons of the cosmic microwave background (CMB). They loose their energy by producing pairs of pions and e^+e^- pairs in these interactions [Gre66]. The particles with energies

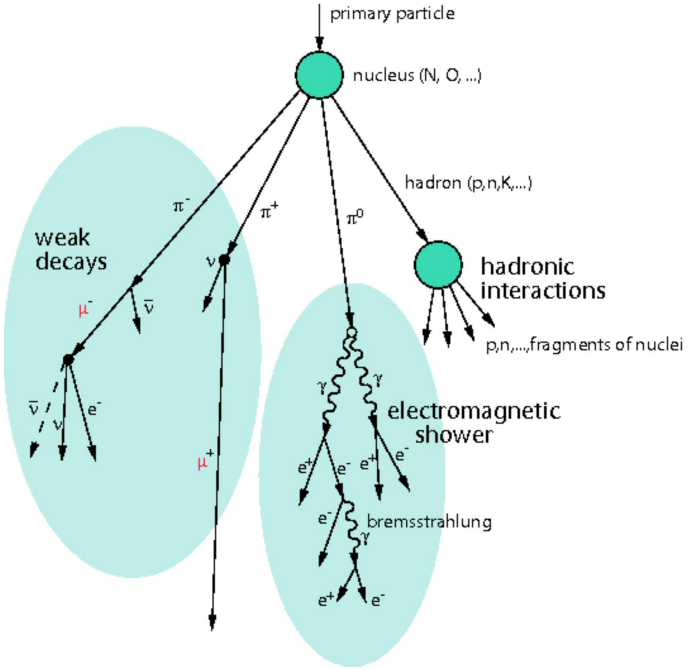

Figure 5.2: Sketch of the interaction of a cosmic ray with the atmospheric gas molecules and the caused shower of particles [Hop04].

above the second knee can be influenced by the onset of these inelastic interactions with the CMB [Ams08].

5.1.2 Cosmic Rays in the Atmosphere

Except for protons and electrons, the cosmic particles in the atmosphere are products of interactions and the subsequent decays. The primary particles hit the atmosphere and interact with its nuclei. In these interactions showers of new particles are generated. Figure 5.2 shows three different kinds of particle production in the atmosphere. When a primary proton hits the atmosphere, the primary particle interacts with an atom of the atmosphere in a nucleon-nucleon interaction. Different secondary particles with lower energies are generated in this process. These particles are baryons as well as neutral and charged mesons.

In the *hadronic interaction* the hadrons can interact with the gas as the primary particle has done it. With a repetition of the effects, a hadronic shower can be generated. If a shower is generated, it consists of a hadronic core with many pions.

The neutral pions act as source for *electro-magnetic showers*, because they decay into photon pairs. These high energy photons subsequently produce electron-positron pairs. Also, the particles emit bremsstrahlung which can again generate electron-positron pairs. In an air shower, the main fraction of particles are e^+ and e^-. $\mu^\pm$ are also produced, but

the amount is about 10 times less. The generated particles of one shower cover a wide area at the ground. The electro-magnetic fraction of the particles has a short reach and is therefore called soft component of the cosmic radiation.
Due to the *weak interaction*, charged mesons like $\pi^{\pm}$ and $K^{\pm}$ decay mainly to muons and neutrinos.
In conclusion, the secondary cosmic radiation consists of the particles generated in hadronic interactions, weak decays and electromagnetic showers. Due to short lifetimes most of them do not reach the ground. Muons an neutrinos with higher half-lives are the most detected at sea level.
Figure 5.3 shows the vertical flux of the major cosmic ray components in the atmosphere. As the detection probability of the neutrinos is low, the most detected particles at sea level are $\mu^{\pm}$.

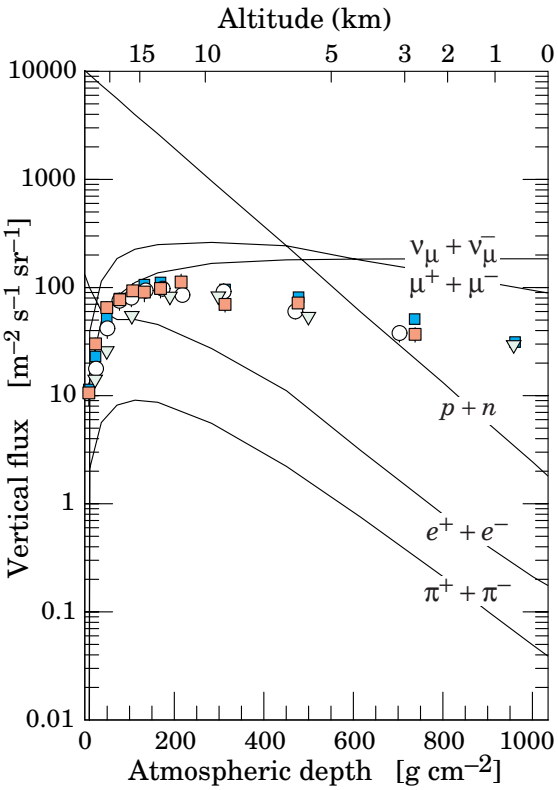

Figure 5.3: Vertical fluxes of cosmic rays in the atmosphere with $E \geq 1\,\mathrm{GeV}$. The points show measurements of negative muons with $E_\mu \geq 1\,\mathrm{GeV}$ [Ams08].

5.1.3 Cosmic Rays at Sea Level

Muons are the most numerous charged particles detected at the earth's surface, with a fraction of 79 % of all secondary cosmic ray particles. Muons decay via weak interaction to

$$\mu^- \rightarrow e^- + \overline{\nu_e} + \nu_\mu \tag{5.2}$$

$$\mu^+ \rightarrow e^+ + \nu_e + \overline{\nu_\mu}. \tag{5.3}$$

Their half-time is $\tau_\mu = 2.197 \cdot 10^{-6}$ s [Ams08] and their mean velocity is $v = 0.99983 \cdot c$, with c being the speed of light. Due to the relativistic time dilation, a muon, which decays after its half-time, can travel 33 kilometers before decaying. Most muons are produced in the atmosphere, more precisely at a height of about 15 kilometers. Therefore the muons can reach the surface of earth, if their entrance angles are not to high, because this extents the distance to the surface by the factor $1/\cos\vartheta$[1].
Before the muons reach the surface, they lose 2 GeV in ionizing processes. The mean energy at sea level is about 4 GeV, and the angular distribution has a shape of $\sim \cos^2\vartheta$ [Ams08]. Figure 5.4 shows the muon spectrum at sea level for 2 different angels ϑ. For large angles, the low energy muons decay before reaching the ground.

[1] ϑ is the inclination angle of a cosmic particle. It is defined with respect to the vertical not regarding the orientation in cardinal points. ϑ does not equal θ which is the projection of ϑ to the zx-plane of the super-module, which will be introduced in Figure 5.6.

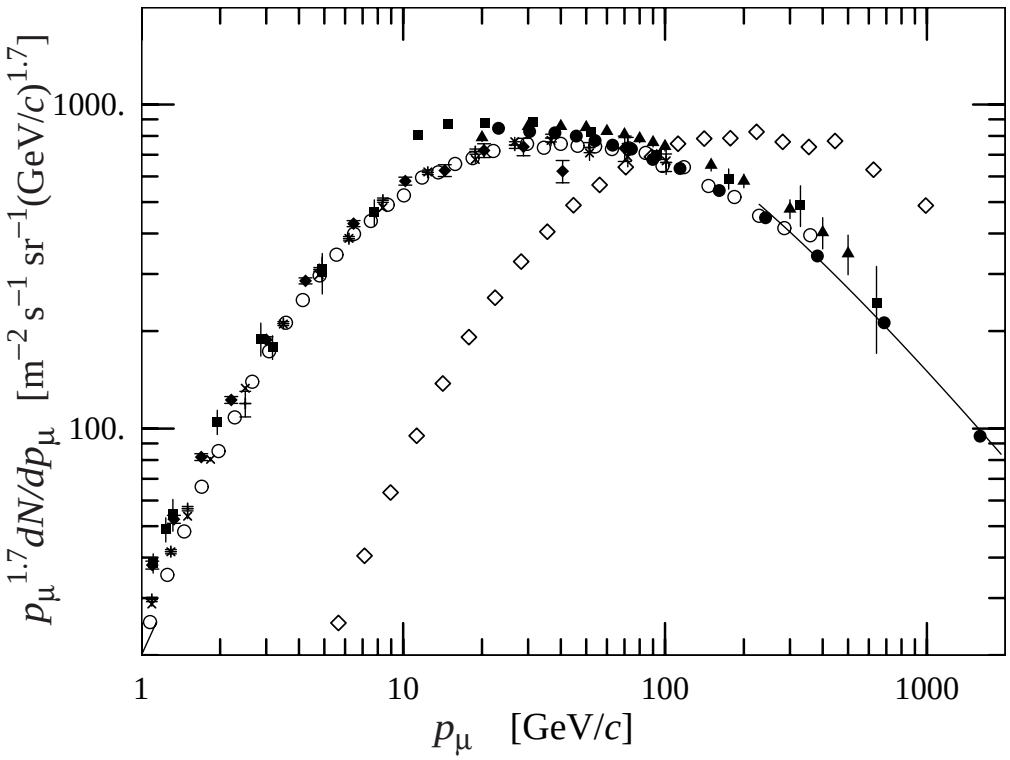

Figure 5.4: Spectrum of muons at $\vartheta = 0°$(♦, ■, ▼, ▲, ×, ○, ●) and $\vartheta = 75°$(◇) [Ams08]. The different symbols represent results of measurements of different experiments.

5.2 Cosmic Trigger

The *Cosmic Trigger* is one of the instruments used for the calibration of TRD super-modules [Bat07].

5.2.1 Tasks of the Cosmic Trigger

Cosmic rays represent a natural source of high energetic radiation. Due to the low terrestrial magnetic field and the high velocities of most of the particles, the trajectories of the incoming particles are almost straight. With a sufficient rate of cosmic events selected by the trigger and the information on the shape of their trajectories, the TRD super-modules can be tested with cosmic radiation. Beside of a test of the operational reliability of each independent detector chamber with its Read Out Boards (ROB), special calibration tasks can be executed:

Gain calibration:

Each pad inside a TRD super-module should give the same signal for the same deposited energy of a certain particle. Therefore the amplification in each compound of a PreAm-

plifier/ShAper (PASA) followed by an Analog-Digital-Converter (ADC) has to be tuned. The values for all compounds provide so-called gain tables.

Alignment of the TRD chambers:

In order to reconstruct tracks of the particles with a good position and momentum resolution, it is important to know the exact position of each TRD chamber. During the assembly the accuracy in positioning the chambers is limited. Cosmic tracks as straight tracks are helpful to correct built-in displacements of the chambers. It is possible to evaluate the displacements and store the corrected geometry in a database. The procedure for correcting the geometry is called alignment. This is described in more detail in Chapter 7.

5.2.2 Design and Setup

Figures 5.5 and 5.6 show the front and the side view of the setup, the super-module and the Cosmic Trigger.

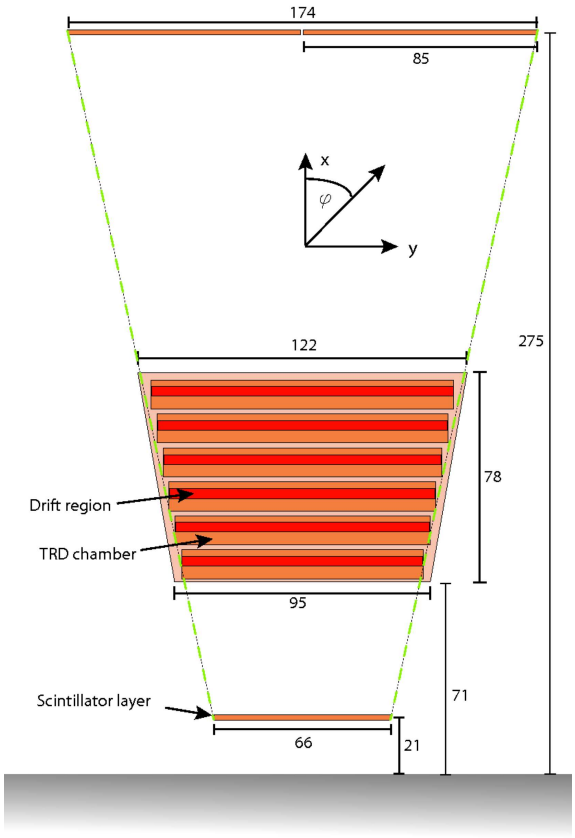

Figure 5.5: Front view of the Cosmic Trigger with a TRD super-module in between in the local coordinate system of TRD [Bat07].

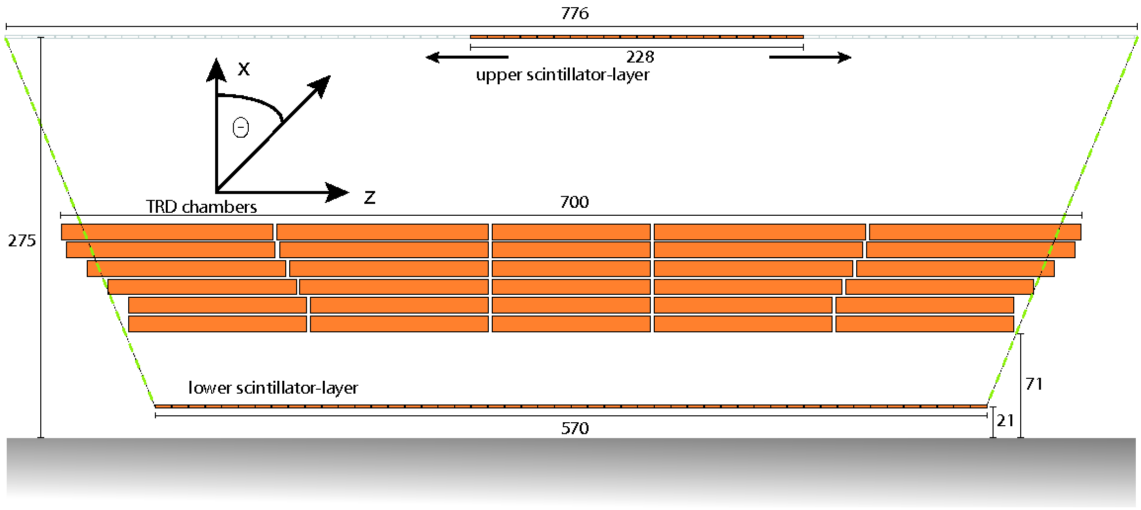

Figure 5.6: Side view of the Cosmic Trigger with a TRD super-module in between in the local coordinate system of TRD [Bat07].

Two operating modes of the Cosmic Trigger are selectable. One mode just uses the signals of the lower layer as a so-called pretrigger for the TRD which comes to its own trigger decision after the pretrigger signal. A second mode is the coincidence mode. The principle of the coincidence mode, which is used in the following, is to check for coincidental signals in the two detector layers of the Cosmic Trigger. Coincidental signals will occur if one particle crosses both layers one after another in a certain time window. The super-module is placed between the detector layers. The geometry of the Cosmic Trigger is chosen in a way that all coincidental hits of the trigger planes are equivalent to a full transit of a particle through the super-module.

The trigger signal passes copper cables and a logic circuit. As soon as the condition of coincident signals is fulfilled, a trigger signal is sent to the super-module and data taking is started for this event.

The Cosmic Trigger is composed of scintillators and photomultipliers. Once a charged cosmic particle transits one scintillator, photons are generated in the plastic scintillator. These photons propagate in the scintillator. Reaching the connected photomultiplier, the optical signal is transformed into an electrical one. As soon as the signal is above a tunable trigger threshold, a logic signal is sent to the trigger circuit. All signals of the upper layer are added to one logical value, as well as all signals of the lower detector layer. The resulting signals are compared in an AND-circuit. Once the AND-condition of the trigger setup is fulfilled, a trigger signal is send to all detector chambers of the super-module and the tracks of the transiting particles can be recorded.

Since the upper layer is shorter than the long side of the super-module, it is not possible to cover the super-module for the coincident method with the upper layer fixed at one

position. In order to obtain tracks in the whole detector, it is necessary to move the upper trigger component during data taking. Therefore the upper layer is movable.

5.2.3 Acceptance of the Cosmic Trigger

The condition of a coincidental signal in both detector layers is fulfilled by one particle crossing the two detectors and so the track of the particle can be measured. The signals in the TRD super-module are converted and stored as described in Chapter 4. It is also possible that more than one particle hits the super-module at the same time. For example, as soon as a shower of particles is generated by a primary cosmic particle, the trigger signal is generated due to one of the secondary particles, but many particles can cross the detector at the same time. Thus, it is possible to get more than one track per event.
In Figure 5.7, the number of reconstructed tracks per event is shown. Due to a limited detection efficiency and a limited tracking efficiency, the reconstructed number of tracks is lower than the real number of particles crossing the detector.
In a dataset with a minimum of one track per event, the events with a single track inside dominate the spectrum of the reconstructed tracks. Events with one track represent 94% of all plotted events. Events with two tracks contribute with 4.7 %. The remaining fraction of the data set holds up to 44 tracks in a single event. Figure 5.8 shows one event with many tracks. It represents a projection of a super-module to the xy-plane. Not all tracks visible in this plot are also reconstructed. This is due to the still limited tracking efficiency.

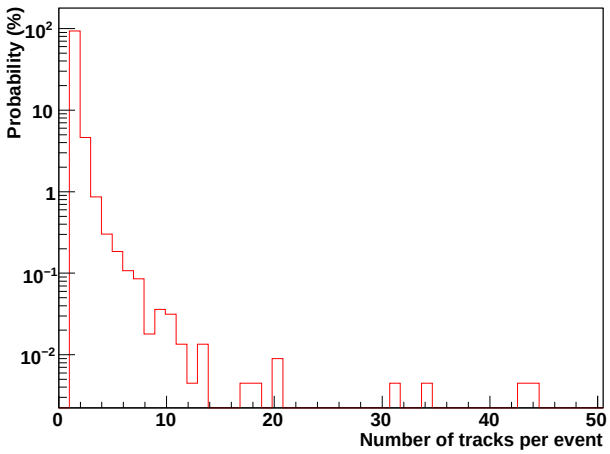

Figure 5.7: Probability of number of detected tracks per event triggered by the Cosmic Trigger.

Besides the possibility to store more tracks at once, the angular acceptance of the trigger is important. Only particles hitting both detector layers can generate a trigger signal. Therefore the angular distribution of events containing only one track is limited.

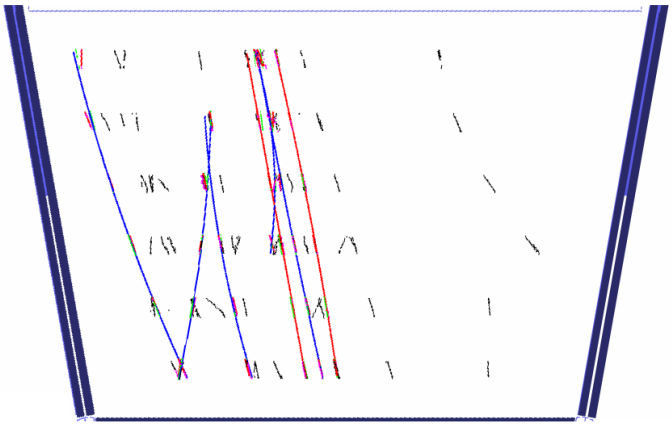

Figure 5.8: A cosmic event detected with a TRD super-module including many tracks.

Since the lower trigger has a wide range in z, the associated angle θ is not the limiting factor. But the geometry in the perpendicular direction y and its angle ϕ cut the acceptance of the trigger. As visible in the front view of the trigger setup in Figure 5.5, the maximum track angle in this projection can be generated by particles transiting the left-most point of the upper trigger and the right-most point of the lower trigger and vice versa. The distance between the detector layers is 2.5 m and the distance between the upper edge and the opposite lower edge is 1.2 m. This leads to a maximum angle of $\phi = 25°$. The angular distribution of simultaneously read-out tracks is wider, because they are read-out without the condition of hitting the detector layers. The resulting angular distribution is therefore a convolution of the angular distribution of cosmic particles at sea level $\sim \cos^2 \vartheta$, and the condition that a track must hit at least four layers and the trigger layers.
Figures 5.9, 5.10, and 5.11 show the projected interaction points of the tracks with the trigger detector layers and the angular distributions of the cosmic tracks in y direction.

In Figure 5.9, the entries represent all events not regarding the number of tracks. There are some tracks which do not hit the trigger detector region. Also the angular distribution has entries above the maximum value $\phi = 25°$ expected for 1-track events. In order to test, if events with only one track fulfill this cut in ϕ, Figure 5.10 is drawn. Here only the events with one reconstructed track are visible. The angular distribution is as anticipated, it is limited by $\pm 25°$. But a few interaction points of the tracks with the detector layers are placed outside the trigger region. As visible in the color palette, only few of such tracks occur, as the blue dots represent only a few entries. Due to the limited reconstruction efficiency, it is possible that another particle, which is not reconstructed, generates the trigger signal. A more inclined second particle is recorded simultaneously. It does not need to hit the detector layers. Because of the fact that these tracks are so rare in this data set, their impact is not clearly visible in the ϕ-distribution.

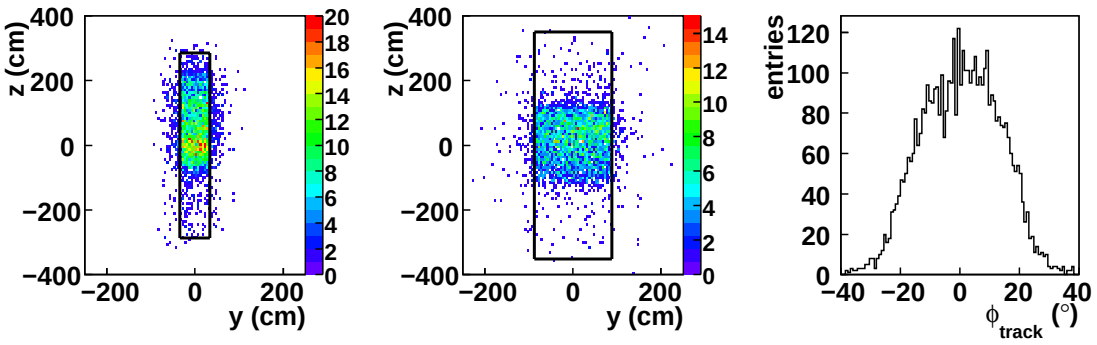

Figure 5.9: The data points are for all events with a minimum of one track. Left panel: the upper trigger layer defined through the black rectangle. Middle panel: the lower trigger layer defined through the black rectangle. Right panel: the track angle ϕ, which is the projection of the track angle to the xy-plane.

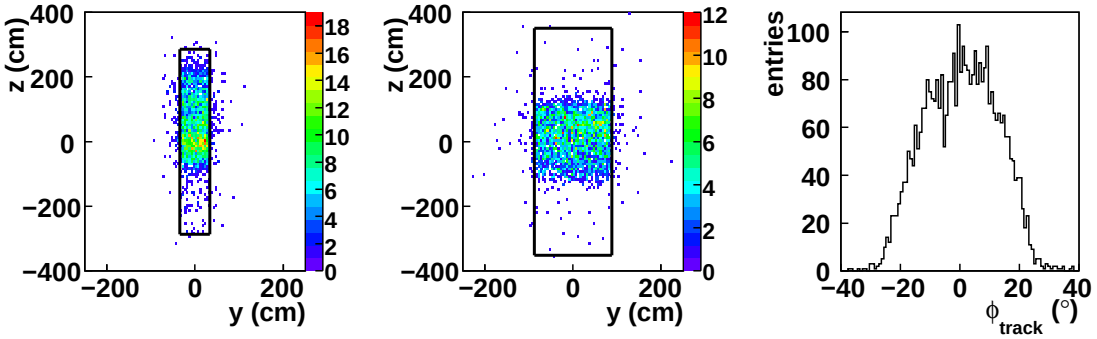

Figure 5.10: The data points are for all events with exactly 1 track. Left panel: the upper trigger layer defined through the black rectangle. Middle panel: the lower trigger layer defined through the black rectangle. Right panel: the track angle ϕ, which is the projection of the track angle to the xy-plane.

A second effect could also explain the outlying hits in Figure 5.10. The coincident signal can be a random coincidence with a simultaneously transiting particle with a huge track angle. The detector is read out, although no single particle hits both detector layers, but two particles pass one layer each at the same time or the detector noise generates the trigger signal at random. The probability for a random event can be calculated [Bat07]: the signal width of a trigger signal is 20 ns. The trigger rate in the upper layer averages to 1600 Hz and the rate of the lower layer is around 1100 Hz. This leads to a rate of random readouts of

$$R_{\text{random}} = 20\,\text{ns} \cdot 1600\,\text{Hz} \cdot 1100\,\text{Hz} = 3.5 \cdot 10^{-2}\,\text{Hz}. \tag{5.4}$$

Simultaneously, a cosmic particle has to transit the detector in the case of a random read out. The trigger rate using the coincidence method is around 80 Hz. Thus just a fraction of much lower than 0.044 % of all events is a random read-out. This coincidence is very

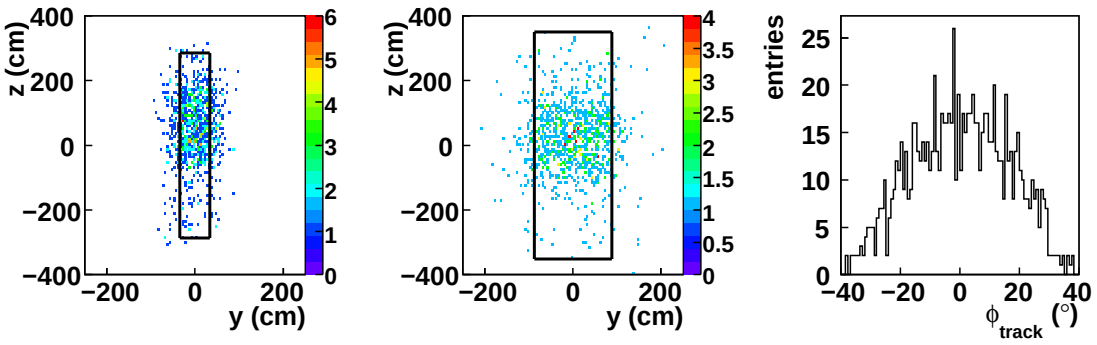

Figure 5.11: The data points are for all events with more than one track. Left panel: the upper trigger layer defined through the black rectangle. Middle panel: the lower trigger layer defined through the black rectangle. Right panel: the track angle ϕ, which is the projection of the track angle to the xy-plane.

unlikely. In conclusion, this effect contributes to the outlying hits, but it is very rare.
The last Figure 5.11 shows all events with more than one track. In such events, the track of the trigger particle and the other tracks can be reconstructed.
It is not possible to distinguish the trigger particle from the other ones with the reconstruction information, except for the assumptions concerning the interaction points with the detector layers, but more than half of the entries are recorded in addition to the trigger particle. The angular distribution is much wider than the distribution of the former spectra. The distribution is not cut by the trigger detector.
In conclusion, the properties of the recorded particles can be explained. The distributions are symmetric. Each detector component works as expected.

6. Standard and Stand-Alone Tracking

6.1 Objects Built during Reconstruction

During reconstruction the data is converted into different objects. *Digits* are digitized signals measured by the read-out pads of the detectors. The *cluster* is a set of digits in space, which are presumably generated by the same particle. The reconstructed *space point* is the estimated position where the particle crossed the sensitive plane of the detector. It is calculated as the center of gravity of the cluster using the pad response function. A linear fit to all clusters of one chamber is called *tracklet*. The reconstructed *track* is defined by a set of 5 parameters, which describe the trajectory of the particle, and the corresponding covariance matrix at a given point in space. The output of the reconstruction is stored in the `Event Summary Data` (ESD). The file is called `AliESDs.root`. Extra information, such as reconstructed tracks of local tracking algorithms, detector clusters, or energy deposits, of the tracks can be written into a file called `AliESDfriends.root` [Hri06]. During the development of the TRD tracking code, a data stream called `TRD.TrackerDebug.root` was implemented in order to check for the proper operation of the tracking. This debug stream allows to monitor coordinates of clusters, tracklets and tracks, track parameters describing the helix shape, and likelihood values [Ber09].

6.2 Global Geometry

The ALICE global coordinate system is a right handed system with its z-axis coinciding with the beam direction and orientated in direction opposite to the muon arm. The x-axis points to the center of the LHC ring and the y-axis points upwards. The origin of the coordinate system is defined by the nominal intersection point of the beams on the z-axis, where the central membrane of the TPC is placed [TP108]. Figure 6.1 shows this system.

6.3 Standard Tracking in ALICE's Central Tracking Detectors

The offline standard tracking is based on a Kalman Filter (KF). The global reconstruction begins with cluster finding in all of the ALICE central detectors, the ITS, TPC, and TRD. Information on the TOF, EMCal and PHOS, later used for the PID, are determined, too. It starts simultaneously with the most precise tracking devices, the TPC and the ITS. The first tracking pass in the TPC starts at large radii of the TPC. Potential tracks, the so

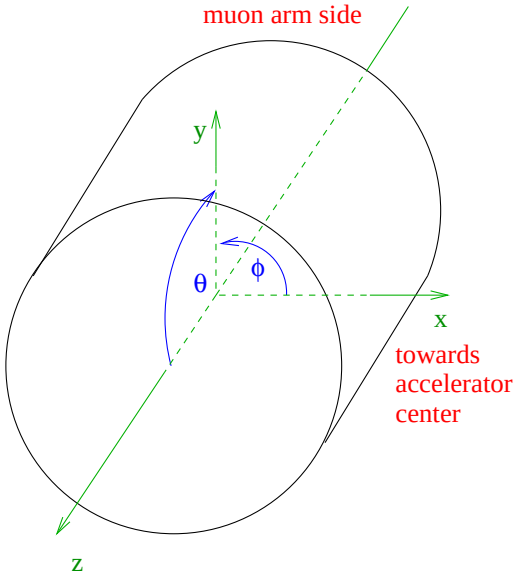

Figure 6.1: The global coordinate system of ALICE defined by the axes x, y, and z and angles ϕ and θ. ALICE is adumbrated with a cylindrical body. The muon arm of ALICE is placed at negativ z.

called *seeds*, in this region are prolongated to the inner region of the TPC. With each step, new clusters are associated to a seed, if new clusters are available. Thus, the precision of the track parameters increases with each step.
From the TPC the track is matched to those found in the ITS, where a separate track finding was processed. Caused by the large η acceptance of the ITS, the p_{T}-cut-off of the TPC, or dead zones in the TPC, some tracks cannot be found in the detector components at radii beyond the ITS. At this step a first estimation of the primary vertex position is done.
After the first reconstruction pass, the tracking is restarted from the vertex back to the outer region of TPC. An extrapolation of the track from the TPC to the TRD is processed in the next step. Here, the clusters of the TRD are attached to the track, which improves the momentum resolution. Next, the tracks are extrapolated to the TOF, the HMPID and the PHOS, where additional PID information is calculated and attached to the track. In the last step, the tracks are refitted backwards to the primary vertex with a Kalman Filter. In addition, a second vertex reconstruction is done in this step [Hri06] [Fas08].

6.4 Local Coordinate System

In order to perform tracking without the information of other detectors, a stand-alone tracking algorithm for the TRD was implemented. Stand-alone tracking plays an important role in the HLT tracking as well as in the reconstruction of the test beam data or the data taken with the cosmic setup in Münster.

6.4.1 Local Geometry

In order to simplify the algorithm of the local tracking, a local coordinate system for the TRD has been introduced. Each super-module has the same coordinate system in the so-called *local tracking coordinates*. This coordinate system is explained in Figure 6.2. An angle α is assigned to each super-module which defines its azimuthal position in the TRD. By rotating the super-modules from their positions in the global system to the position of $\alpha = 0°$, the global system can be transformed to the local tracking system.
In the local tracking coordinates the origin, the z-axis and the angle θ are the same as in the global coordinate system. The x-coordinate is perpendicular to the beam line and for each TRD super-module perpendicular to its pad plane. The y-axis is also perpendicular to the beam line and points upwards as presented in Figure 6.2. The angle in the xy-plane starting at the x-axis is ϕ. This system is also a right-handed coordinate system.

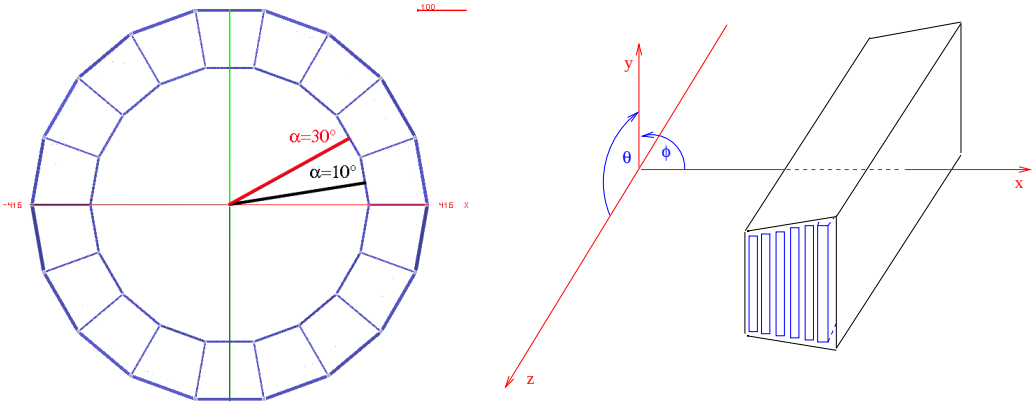

Figure 6.2: Left panel: projection of the space frame including the TRD to the xy-plane. The rotation angle α in this plane defines the positions of the super-modules. Two angles are shown as example. Right panel: in the local tracking coordinate system of the TRD, defined by the x, y, and z-axis, and the angle ϕ and θ, each super-module is positioned at $\alpha = 0°$. The ϕ of the local coordinate system can be calculated by $\phi_{\text{local}} = \phi_{\text{global}} - \alpha$.

6.4.2 Pad Tilting Corrections for the y Coordinate

The read-out pads have a larger length in the z-direction than in the y-direction. On average, the length of the pads in z-direction is 8.8 cm and in y-direction it is 0.7 cm [TRD01]. Therefore, the position resolution is less precise in z than in y. In order to increase the precision of the resolution in z-direction, the pads of the pad plane are slightly tilted by $\varphi_{\text{T}} = \pm 2°$ with respect to the z-axis.
The advantage of this geometry is that with combining the information of the z-coordinates of all layers and assuming a helix shape for the trajectory of the traversing particle, a more precise resolution in z can be reached. The pad tilting is shown in Figure 6.3.

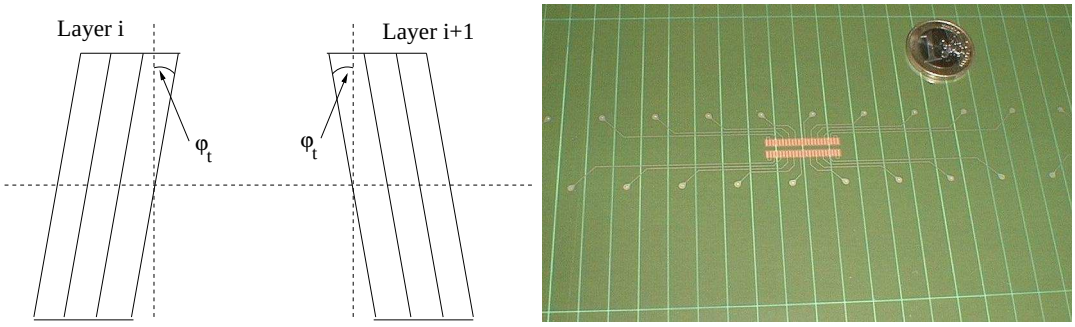

Figure 6.3: Pad tilting. Left Panel: schematic picture of the pad plane for all layers with consecutive layer numbers. The pads are tilted with $\varphi_t = \pm 2°$ [TRD01]. Right Panel: picture of the pad plane [PIH09].

Due to the pad tilting the measured y- and z-coordinates of a space point in a single layer are correlated. Thus, the disadvantage of the tilting is that the y-coordinate has to be corrected. The corrected coordinate y' can be calculated with Equation 6.1. In Figure 6.4 the transformation is shown:

$$y' = y - \tan(\varphi_t) \cdot (z_{\text{center}} - z_{\text{real}}), \tag{6.1}$$

where z_{center} is the z-coordinate of the center of the pad.

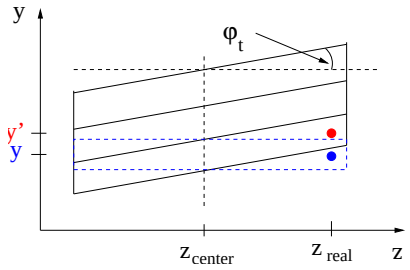

Figure 6.4: Visualization of the coordinate transformation y to y'. The blue dashed rectangle represents the pad without tilting and the blue point the measured point at (y,z). The red point is placed at the corrected position (y',z).

6.5 TRD Stand-Alone Tracking

6.5.1 Track Finding

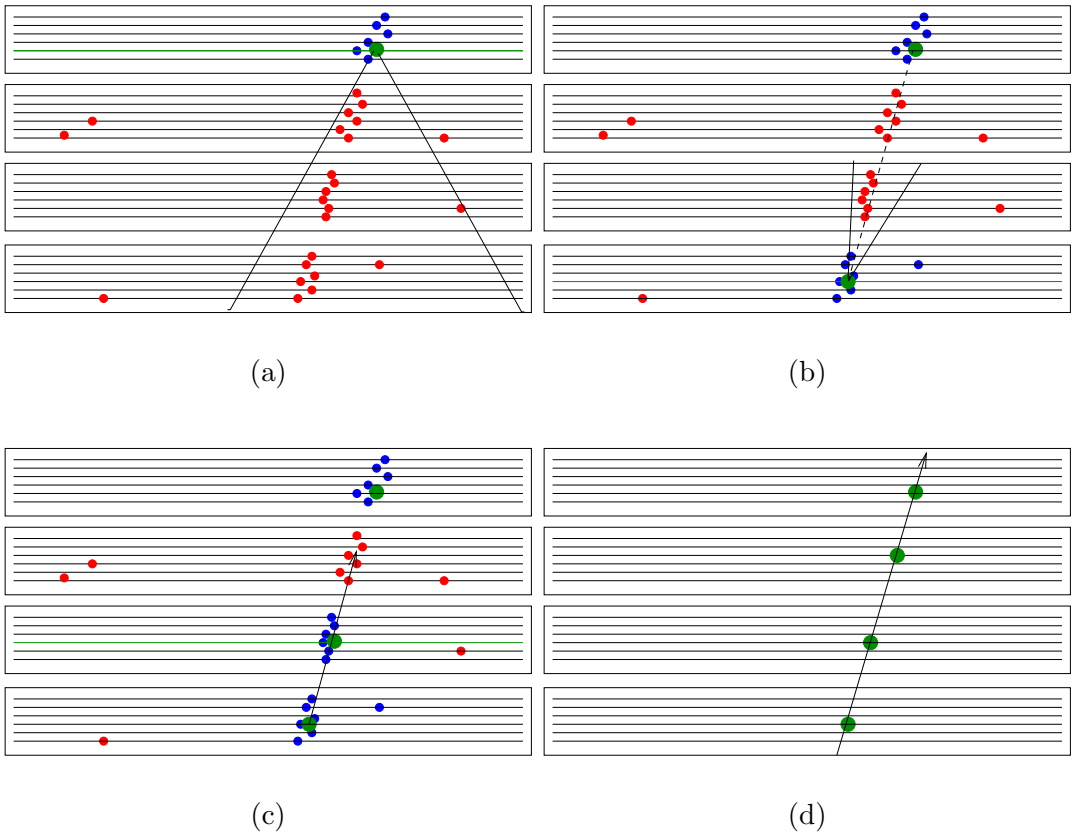

Figure 6.5: Track finding dealing with simplified clusters, called seeding clusters [Fas08]. The clusters can be generated by a traversing particle or by detector noise. The green points represent so-called seeding clusters, which are found by projecting selected clusters of a chamber to a reference plain of the chamber. Their position is defined by the center of the projected cluster distribution around a maximum. Maxima are expected to be placed around the midpoint of a tracklet. The seeding clusters of used to perform a first track fit. The points are assumed to be on a Rieman circle given by Equation 6.2.

In Figure 6.5 the concept of track finding in a stack is explained. In the following the chambers are named with numbers beginning with No.1 for the lowest chamber in Figure 6.5. In each track finding step, four chambers are considered. Combinations of consecutive chambers are favored and combinations with large gaps between the chambers are suppressed. In the chosen chambers so-called *seeding clusters* are searched as input for a first Riemann circle fit. The seeding clusters are found by projecting selected clusters of a chamber to a reference plain of the chamber. Their position is defined by the center of the projected cluster distribution around a maximum. Maxima are expected to be placed around the midpoint of a tracklet. The seeding clusters are starting points for the track

finding.
To minimize the effect of inefficiency and dead detector areas, the reconstruction is repeated for different combinations of chambers. In a final pass, clusters that belong to two tracks are either assigned to one of the two tracks or the tracks are combined to one track [Fas08].
Figure 6.5 (a): the fourth chamber of the four is taken as starting point. All found seeding clusters are considered as possible origin of a track. Starting at one found seeding cluster a pyramid-shaped volume is defined. The opening angle of the volume restricts the maximum inclination of a track. In ϕ-direction the angle is $\phi_{\max} = 48°$ and for the θ-direction the opening angle is $\theta_{\max} = 65°$. Chamber one is scanned, in order to find clusters within the cut criteria.
Figure 6.5 (b): the clusters found in chamber one are projected to a reference plain in the chamber. At their central point, the new seeding cluster, a new pyramid is created. The center of the pyramid is defined by the line between the starting seeding clusters of the previous step and the seeding clusters of chamber one. The seeding cluster of chamber two is calculated with all clusters in the defined area.
Figure 6.5 (c): the cluster position is extrapolated to chamber three in order to find the seeding cluster of that chamber. A path is defined to allow bending of the track by the magnetic field. All clusters which are next to this path in chamber three are used to calculate the seeding cluster of chamber three. The maximum distance to the path is set to 3 cm in y-direction and 20 cm in z-direction.
Figure 6.5 (d): all four seeding clusters, the complete seeding configuration, are used to perform a first track fit.

6.5.2 Rieman Circle Fit for Seeding Clusters

In the stand-alone tracking (SAT) a Riemann parametrization is used to describe the track in the xy-plane as a circle. A linear parametrization is used for the xz-plane. The quadratic relation of Equation 6.2 describes a circle and can be translated to a linear equation. This can be fitted with a fast linear fitter. The translation is presented in the following:

$$(x - x_0)^2 + (y - y_0)^2 - R^2 = 0, \tag{6.2}$$

where (x_0, y_0) is the center of the circle and R is the radius. The following transformations simplify the former equation to a linear one in so called conformal coordinates:

$$(x^2 + y^2) - 2(xx_0 + yy_0) + (x_0^2 + y_0^2) - R^2 = 0, \tag{6.3}$$

$$1 - \frac{2x}{x^2 + y^2} \cdot x_0 - \frac{2y}{x^2 + y^2} \cdot y_0 + \frac{1}{x^2 + y^2}(x_0^2 + y_0^2 - R^2) = 0, \tag{6.4}$$

$$1 - ux_0 - vy_0 + t(x_0^2 + y_0^2 - R^2) = 0, \tag{6.5}$$

using this transformations for the last step

$$u = \frac{2x}{x^2+y^2}, \tag{6.6}$$

$$v = \frac{2y}{x^2+y^2}, \tag{6.7}$$

$$t = \frac{1}{x^2+y^2}. \tag{6.8}$$

With this transformation

$$\frac{1}{y_0} - u\frac{x_0}{y_0} - v + t\frac{(x_0^2+y_0^2-R^2)}{y_0} = 0, \tag{6.9}$$

and using

$$a = -\frac{1}{y_0}, \tag{6.10}$$

$$b = \frac{x_0}{y_0}, \tag{6.11}$$

$$c = \frac{R^2-x_0^2-y_0^2}{y_0}, \tag{6.12}$$

this final equation can be evaluated:

$$a + ub + tc + v = 0. \tag{6.13}$$

All found seeding configurations composed of the seeding clusters of the four layers 6.5.1 are fitted with the linear fit described by Equation 6.13. This is done in the function `AliTRDtrackerV1::MakeSeeds()`. The coordinates can be monitored with its debug stream `MakeSeeds0` which is written to the file `TRD.TrackerDebug.root` [Bel04, Fas08]. The described, simplified track calculation allows the rejection of bad potential tracks at an early stage of the tracking. Track specific constants are taken out of a class `AliTRDrecoParam`. AliTRDrecoParams contain cut parameters to decide whether to accept the track or not. The tuning of these values for different data sets taken in high flux or low flux environments is currently under investigation [Fas08].

6.5.3 3-Dimensional Tilted Riemann Fit for Real Clusters

With the reference calculation of the circle fit described by Equation 6.13, it is now possible to find the associated clusters of the tracks. The clusters of the remaining layers are now also attached to the extrapolated track. Taking the pad tilting into account, the z-resolution can be improved. In each chamber a linear reference fit is calculated, which is called the tracklet.
The cluster finding and the calculation of the tracklet is done iteratively: first the pad which is hit by the track fit and the tracklet fit is chosen. All clusters belonging to the

pads are attached.
If the quality of the tracklet fit is not sufficient, a second iteration is performed by shifting the expected position in z-direction towards the neighboring pad row. With that, pad crossing is taken into account. After this step, a linear fit in y-direction considering the pad tilt is performed [Fas08].
For the new track fit of all found clusters, the following parametrization is used. Then, the parametrization are put to Equation 6.13, which is here presented again in short and in long form:

$$\begin{aligned} a + ub + tc + v &= 0 \\ \Longleftrightarrow 1 - \frac{2x}{x^2+y^2} \cdot x_0 - \frac{2y}{x^2+y^2} \cdot y_0 + \frac{1}{x^2+y^2}(x_0^2 + y_0^2 - R^2) &= 0, \end{aligned}$$

y is the measured y-coordinate of the clusters. The true y-coordinate called y' can be calculated with the correction for tilted pads:

$$y' = y - \tan(\varphi_t) \cdot (z_\mathrm{c} - z_\mathrm{track}). \tag{6.14}$$

With this correlation between the y and z-coordinate, it is possible increase the z-resolution. Approximately, the z_track position depends linearly on x [Bel04]:

$$z_{track} = z_0 + \frac{\mathrm{d}z}{\mathrm{d}x}(x - x_\mathrm{ref}) = d + e(x - x_\mathrm{ref}). \tag{6.15}$$

$d = z_0$ is the offset, x_ref is the position of the track at the reference point, and $e = {}^{\mathrm{d}z}/_{\mathrm{d}x}$ is the slope. Also the following approximation is applied:

$$x^2 + y^2 \approx x^2 + y'^2. \tag{6.16}$$

Altogether with Equation 6.13 the parameterizations lead to:

$$a + bu' + ct' + dv' + ew' - 2(y' + \tan(\varphi_\mathrm{t})z_c) = 0, \tag{6.17}$$

using the following transformation:

$$t' = \frac{1}{x^2 + y'^2}, \tag{6.18}$$

$$u' = \frac{2x}{x^2 + y'^2}, \tag{6.19}$$

$$v' = \frac{2\tan(\varphi_\mathrm{t})}{x^2 + y'^2}, \tag{6.20}$$

$$w' = \frac{2\tan(\varphi_\mathrm{t})(x - x_{ref})}{x^2 + y'^2}, \tag{6.21}$$

and

$$\begin{aligned} a &= -\frac{1}{y_0}, \\ b &= \frac{x_0}{y_0}, \\ c &= \frac{R^2 - x_0^2 - y_0^2}{y_0}, \\ d &= z_0, \\ e &= \frac{\mathrm{d}z}{\mathrm{d}x}. \end{aligned}$$

Equation 6.17 describes the trajectory of the particle with a linear formula. A fast linear fit can be performed. It is called `RiemannTiltFit`. The precision of the fit can be described with the width of the residuals between cluster position and fitted track position.
This tracking step allows to reject potential tracks which do not fulfill requirements defined by the AliTRDrecoParams. The tuning of this reconstruction parameters for this tracking step is under investigation, too.
The clusters processed in this step are streamed to `MakeSeeds1`. These clusters are used in the following to calculate the position resolution of the super-module. At this early step the tracking efficiency is very high, at later steps many tracks are rejected.

6.6 Cluster Resolution

The cluster resolution of the TRD tracks is the width of the distribution of deviations between clusters and the track. It is given by the intrinsic detector resolution and by the tracking procedure. After calibration of the super-modules with an alignment procedure, the resolution should improve. The alignment procedure is described in Chapter 7. In the following, one possibility of calculating the cluster resolution is presented. For a better understanding, the corrected y-coordinate is called y in the following instead of y'.

Figure 6.6 shows the deviations between track and cluster coordinates before and after the correction for pad tilting[1]. For the following investigations the correction is taken into account.

The cluster resolution depends on the track angles ϕ and θ. In the following, just the resolution in y-direction as a function of ϕ is analyzed. If a track has an angle of $\phi = 0°$, the accuracy of the track reconstruction is limited by the resolution in y. If

[1]The clusters are from the debug stream `MakeSeeds1`.

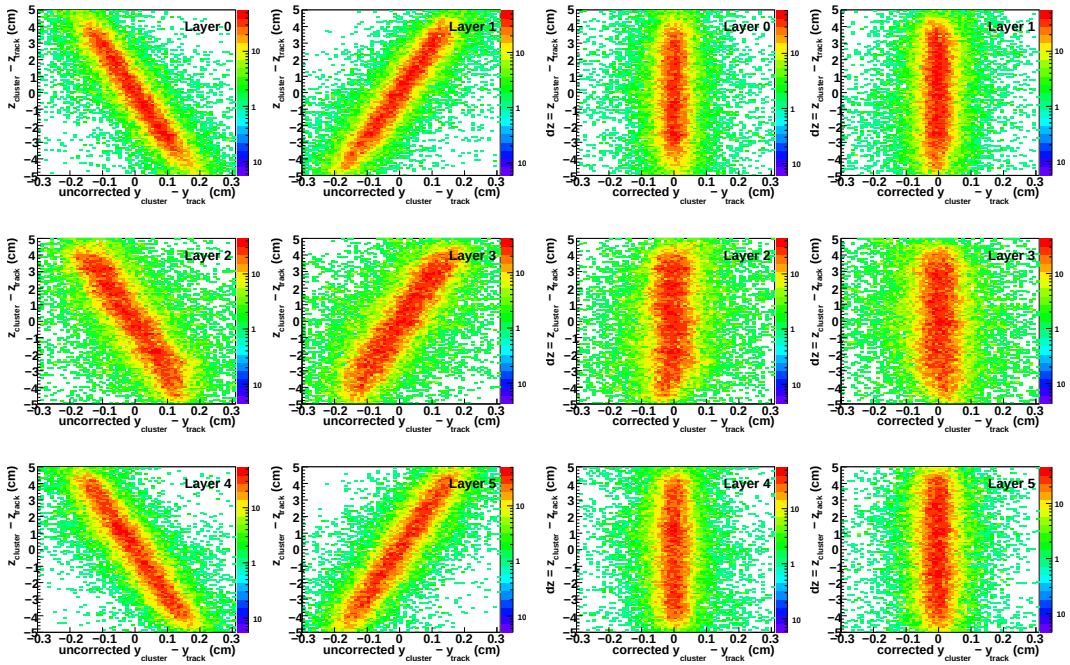

Figure 6.6: Correlations between the displacements of cluster coordinate and tracklet coordinate calculated for coordinates with and without tilted pad correction.

the track angle is not zero, also the uncertainty of the x-direction influences the result. Consequently, the measurable resolution is a combination of both resolutions:

$$\sigma_{y,\text{combined}} = \sqrt{\sigma_{\text{x}}^2 \cdot \tan^2 \phi + \sigma_y^2}. \tag{6.22}$$

The resolution can be determined with the distribution of $\mathrm{d}y = y_{\text{cluster}} - y_{\text{track}}$. The width of the distribution is the resolution σ_y of the detector integrated over all track angles.
The track-angle dependent resolution can be determined with the correlation of the residuals and the track angle ϕ. Figure 6.7 shows this correlation for cosmic ray data taken in Münster.
In order to calculate the distribution $\sigma_y(\phi)$, each bin in ϕ of the Figure 6.7 is projected to the y-axis of the histogram and plotted. One of these histograms is presented in Figure 6.8.

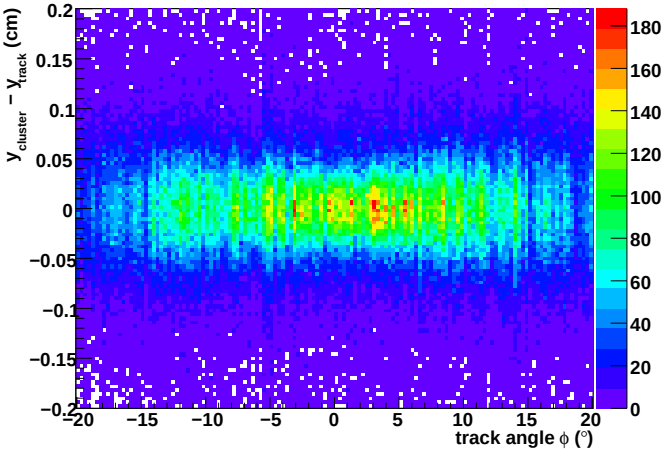

Figure 6.7: Deviations of $y_{\text{cluster}} - y_{\text{track}}$ as a function fo the track angle ϕ.

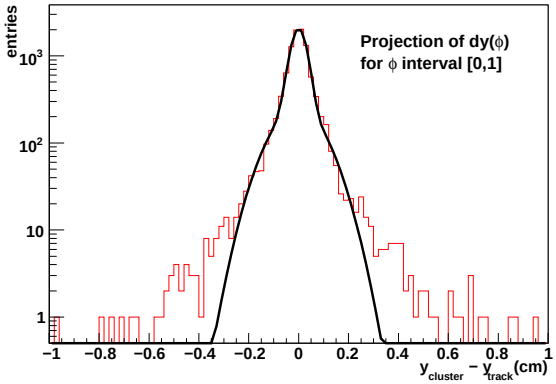

Figure 6.8: Projection of Figure 6.7 to its vertical axis for the ϕ intervall [0,1].

The distribution is fitted with a combination of two Gaussians. The narrower, inner Gauss represents the residuals of real clusters to the reconstructed tracks. Falsely attached clusters are not rejected in the MakeSeed1 step of the reconstruction. Therefore the Gaussian of the real clusters is superimposed by a second Gaussian of falsely associated clusters, which is much wider.
After fitting all projections, the $\sigma_{\phi-\text{slice}}$ of the inner Gauss function is plotted as a function of the track angle ϕ. The result is used to estimate the combined resolution and to find systematic errors in calibration and reconstruction of the cosmic ray data. In the distribution a minimum of σ is expected at $\phi = 0°$ for no magnetic field. The distribution of $\sigma_{y,\text{combined}}(\phi)$ is fitted with Equation 6.22. ϕ is the argument and σ_y and σ_x are the fit parameters.

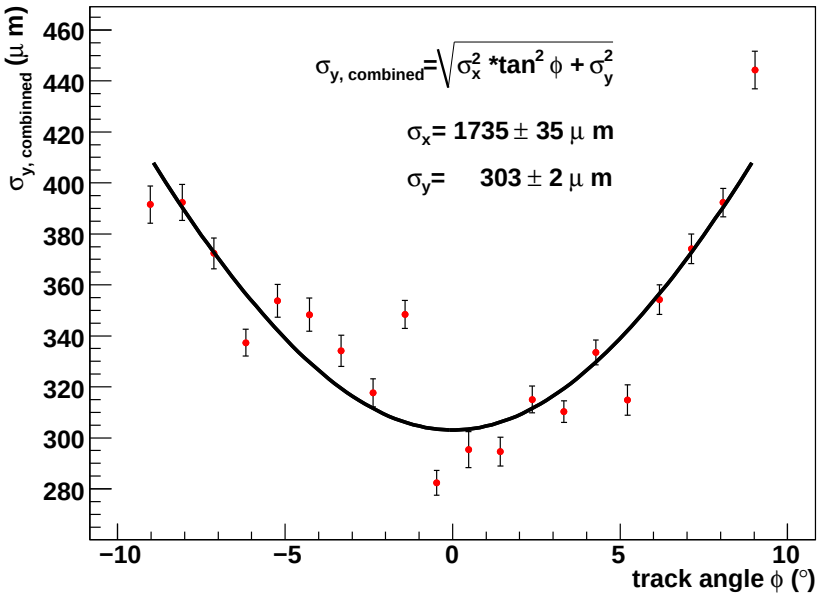

Figure 6.9: $\sigma_{y,\text{combined}}(\phi)$ calculated with data from the MakeSeeds1 debug stream. The error bars represent the uncertainties of the fit parameter σ.

The fit parameters provide an estimate for the resolution at $\phi = 0°$. The value is $\sigma_y = 303 \pm 2\,\mu$m. The point resolution was also calculated with the raw data of one chamber using a linear fit. The value of $\sigma_{\text{y,raw}}$ has values between $160\,\mu$m and $200\,\mu$m for different TRD layers [Wul09]. Due to the different pad widths, the resolution varies with the layer. The degradation of the result with reconstructed data of the debug stream can be explained by the misalignment of the chambers. After correcting the misalignments the resolution is calculated again and is compared to this value. This is done in Chapter 7.

7. TRD Alignment

The alignment is done via a set of procedures combining all information on the detector geometry with the offline geometry, whose compound is then used in simulation and reconstruction of tracks. The offline geometry is based on the drawings of the detectors. But due to limited accuracy in the assembly processes and time-driven deformations, such as twisting and sinking due to thermal and mechanical stress, the real position of the detector modules can differ from their positions in the ideally planned geometry.
In order to minimize the loss of accuracy during conversion of detector signals into spatial positions, the deviations have to be corrected. This increases the detector efficiency and the precision of the reconstructed tracks and vertices.
The corrections of the chamber positions to the ideal geometry are called alignment constants. They can be calculated for each alignable volume in its reference system (RS). Procedures of the official alignment framework are explained and used in the following. They allow to calculate and store the alignment constants in the Offline Conditions Data Base (OCDB) and apply them to the ideal geometry. The procedures are tested with straight tracks from cosmic-ray data taken in Münster, but can also be used with cosmic tracks taken at CERN or tracks generated in collisions with and without magnetic field [ALN09].

7.1 Accounting for Misalignment in the Track Reconstruction

7.1.1 ALICE Geometry

The geometry of ALICE is based on the ROOT class `TGeo`. It is organized in a tree structure. Each volume can be identified through its volume path, a string containing the names of all physical volumes in the current branch of the tree. The name is composed by module names separated with a slash ('/'), going from the innermost to the outermost containers and from the lowest to the highest level in the geometry tree, starting from the mother volume. For example, the branch of the TRD can be divided into 18 super-module branches, with 5 stack branches each and 6 chamber branches for each stack. Figure 7.1 shows a schematic view of the TRD with its components [ALN09].

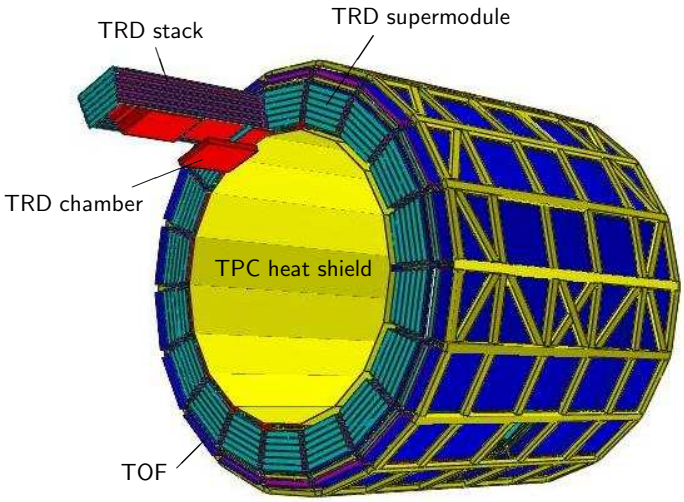

Figure 7.1: Schematic view of the TRD in the ALICE space frame. The detector consists of 18 super-modules. Each SM contains 30 read-out chambers arranged in 5 stacks and 6 layers. The TRD is surrounded by the TOF detector. Inside the TRD, the TPC is placed [TP108].

7.1.2 Alignable Volumes

Each sub-module can be aligned with respect to its reference system, the upper branch of the geometry tree. In the mother systems, the sub-modules are so-called alignable volumes. For example, the TRD chamber of super-module 0, stack 2, and layer 2 (which is plane number 14 in the global system) with the volume path `TRD/sm00/st2/pl4` is alignable to its mother `TRD/sm00/st2`.
In addition, different branches can be aligned to each other. Thus, whole stacks can be aligned to neighbor stacks, and components of the TRD can be aligned to the neighbor detectors of the TRD, the tracking detector TPC [ALN09].

7.1.3 Alignment Constants

The correction to the ideal geometry for each alignable volume in its RS can be expressed by so-called alignment constants. In the alignment framework, there are six constants, three shifts along three axes, x, y and z, and three tilts around the same axes described with three Euler angles Ψ, θ and ϕ. These values describe the corrections in the global ALICE system. The alignment framework also offers the possibility to convert the constants into shifts and rotations in the local geometry system [ALN09]. For TRD chambers, these are the axes r, z and ϕ_r. These axes are shown in Figure 7.2. The origin of the local alignment coordinate system is the midpoint of the chamber.

The r-axis points perpendicular to the sensitive plane of each chamber. The ϕ_r points in direction of y, which is along the short side of the super-module, and the z-axis is the

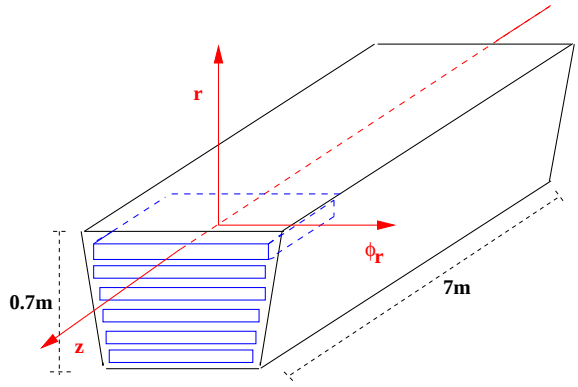

Figure 7.2: Schematic view of a TRD super-module and the axes of the local alignment geometry. The origin of the coordinate system is the midpoint of the chamber.

same as in the global system pointing in direction along the long side of the super-module. The shifts and tilts around the three axes in the local system are shown in Figure 7.3.

7.1.4 AliAlignObjects and the AliGeoManager

The constants assigned to the alignable volume are stored in an alignment object, an instance of the class `AliAlignObj`. The `AliGeoManager` for alignable volumes enables the user to access the different sub volumes and their alignment constants. During alignment procedures, the manager provides a fast iterative access to the volumes and their constants via two look-up tables [ALN09].

7.1.5 Offline Conditions Data Base

The alignment objects can be written to ROOT files, which are part of the Offline Conditions Data Base (OCDB). The OCDB is not a relational database as it would be implemented with e.g. Oracle [Ora09], MySQL [Mys09], etc, but it is a set of entries in the grid framework of CERN, the `AliEn` file catalog. The OCDB points to ROOT files stored in storage elements of the grid containing the calibration and alignment data. From there the information can be retrieved. In combination with the ideal geometry, the alignment information of the OCDB is used during simulation and reconstruction to accounts for the misalignments of the detector components.

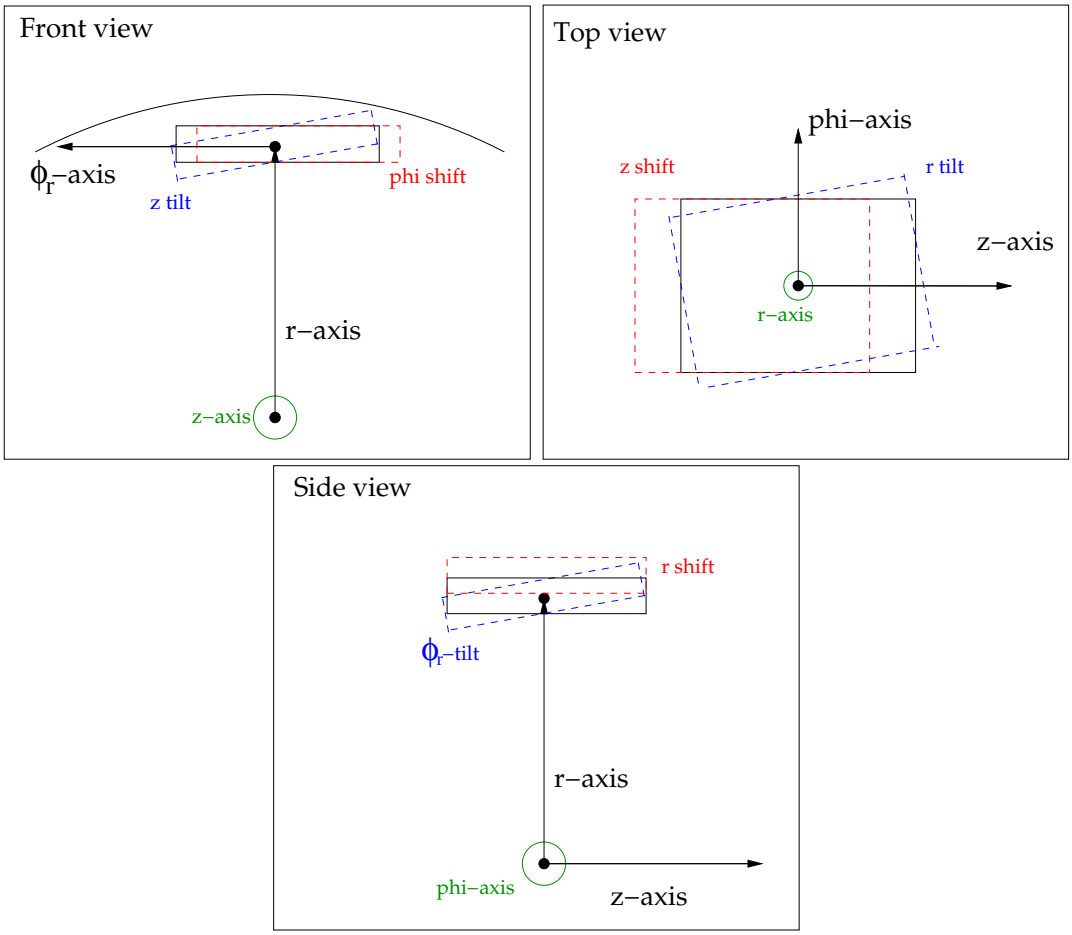

Figure 7.3: The three figures present the 6 possible displacements. Each misalignment can be expressed as a superposition of 6 independent movements. These three shifts (red) and tilts (blue) have to be calculated for all chambers after the assembly. Due to time-driven deformations, the procedure has to be repeated from time to time.

The OCDB is filled with condition objects. Just one example is the information on the alignment, which is updated by survey and alignment procedures, as soon as the reconstruction will start from real data. In addition, other calibration objects are stored in the OCDB, for example drift velocities or the starting time t_0 given by the offset of the trigger signal. Calibration and alignment objects are run dependent objects [OCD09].

7.2 Mechanical Alignment during TRD Assembly

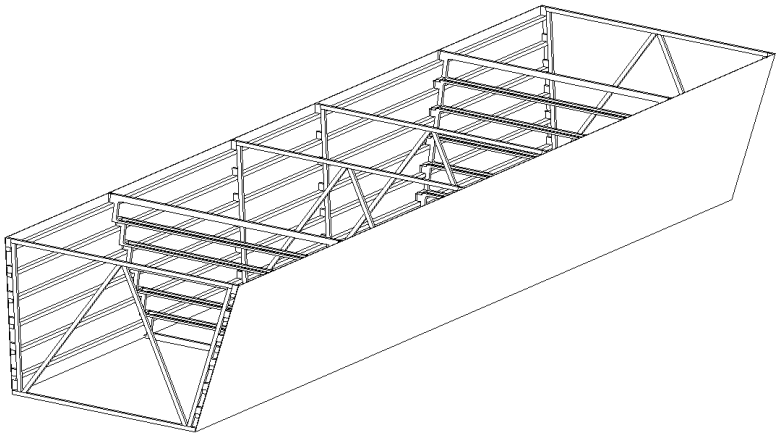

Figure 7.4: Axonometric view of the super-module support structure with side panels [TRD01]. On the side walls so-called chamber ledges are mounted. To these ledges the detector chambers are fixed. Inside of the body the so-called stair frames are placed. These frames are placed between the chambers. The stair design is due to increased chamber length in z-direction with increased layer number.

The shape of the super-module was designed to minimize positioning errors. Its design is shown in Figure 7.4.
The chambers are fixed with six screws, three on each side in ϕ_r-direction, to the chamber ledges. This allows a displacement of less than 1 mm in ϕ_r-direction, which can be minimized by carefully aligning the read out chambers within the super-module hull. The chamber has to be placed with the same gap to the hull in both directions of ϕ_r. The displacement in z-direction is limited by the holes for the screws. The positioning of the holes has an uncertainty of a few tenths of a millimeter. Displacements in direction of r are possible, if the chamber does not lay flat on the chamber ledges. A reason can be a drop of glue, which has to be found and removed before assembly. This can also cause a tilt around all three axes. In addition, the ledges can be displaced, since the accuracy of the hull assembly is limited.
In order to minimize all possible displacements, the error sources come under great scrutiny during the assembly of a chamber. Thus, the first step of the alignment-procedure of the chambers is already done at this point.

7.3 Determination of Misalignment Using Tracks

The official offline framework provides macros and special alignment classes for the determination of the detector misalignment. The schema for the realization of the alignment procedure is presented in Figure 7.5.

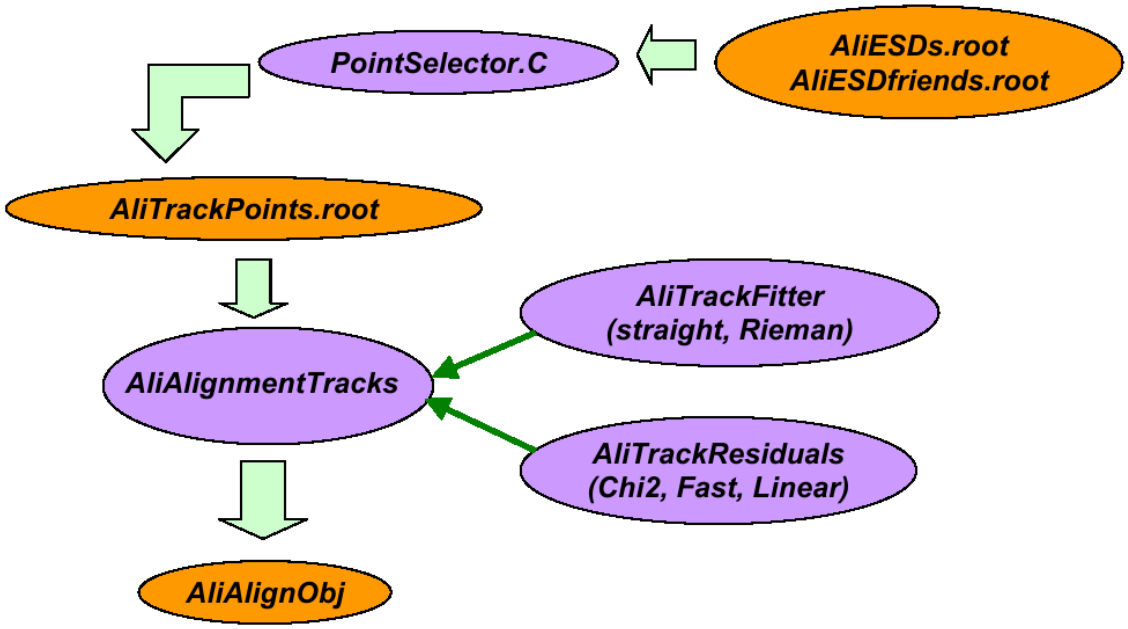

Figure 7.5: Schema of data processing in the alignment procedure [Mis08].

The reconstructed tracks and extra information concerning the tracks are saved in instances of `AliESDs.root` and `AliESDfriends.root`. With the macro `PointSelector.C`, it is possible to select tracks fulfilling specific selection criteria, like a minimum number of associated clusters or tracklets, a maximum amount of deposited energy and so on. Each of the selected tracks is converted into a set of spacepoints stored track-by-track in an `AliTrackPointArray`. These are written to a file called `AliTrackPoints.root`. Each space-point consists of 3 coordinates, their errors, and the index of the associated sub-detector.
With another macro called `align_volume.C`, the space points are converted to `AliAlignmentTracks` and fitted with `AliTrackFitter`, which provides different models for the fit: a straight line fit can be used or a Riemann fit describing the helix shape of tracks of charged particles in a magnetic field. The user can define reference volumes and volumes-to-be-aligned. Thus, a reference system is defined. The volumes will be aligned in this RS. In addition, the user can choose between several minimization methods for the `AliTrackResiduals`, such as a χ^2 minimization, a fast algorithm for minimization, and a linear one.

Running the macro, the chosen minimization is processed. It determines such a transformation of the volumes-to-be-aligned, that the χ^2 between their space points and the track, which is defined by the reference volumes, is minimized. The 6 alignment constants are the results of the minimization and are stored in the objects `AliAlignObj`.

7.4 Sources of Data for TRD Alignment

Different data sets can be used for the alignment of TRD. These are

- cosmic ray data taken in Münster,
- cosmic ray data taken at CERN at Point 2, with and without magnetic field, and
- collision data, with and without magnetic field.

With all data, the relative alignment of the chambers within their RSs of their stacks can be processed. In addition, it is possible to align neighboring stacks to each other, if a sufficient number of tracks with stack crossing are measured. With data taken at CERN, the stacks and the super-modules can be aligned with respect to the whole TRD and the TPC. In addition, a recalculation of the alignment of the chambers in a stack can be performed. As example a cosmic event taken at CERN is shown in Figure 7.6. The magnetic field was switched on. The light blue dots represent clusters in a TRD module.

7.5 Application of the framework to the Setup in Münster

7.5.1 Description and Calibration of Data Set

In the following, the cosmic run 1022 with 25 files is used for the alignment calculations. This run was taken with super-module III. The upper layer of the Cosmic Trigger, which was described in Chapter 5.2, was placed above stack 2. The anode voltage applied in all chambers was 1500 V, and the drift voltage was 1350 V. The gas composition in the detector was Ar/CO_2 (83.5%/16.5%) [Gri09] and the software configuration used in the run is called `p_zs-s16c40n_csmtrk_autotrg`.
The distribution of the integrated charge per pad and the average pulse height distribution of one chamber in layer 2 is presented in the Figures 7.7 and 7.8 for one file of run 1022.
In the following analysis, the alignment of the chambers of stack 2 is described as an example.
For the reconstruction, the data set has to be calibrated. It is important to determine the correct drift velocity of the ionized particles in the drift region. The velocity depends on the gas mixture and the drift voltage. The drift velocity can be estimated using the length of the drift plateau or by comparing the angle of inclination of the track and the

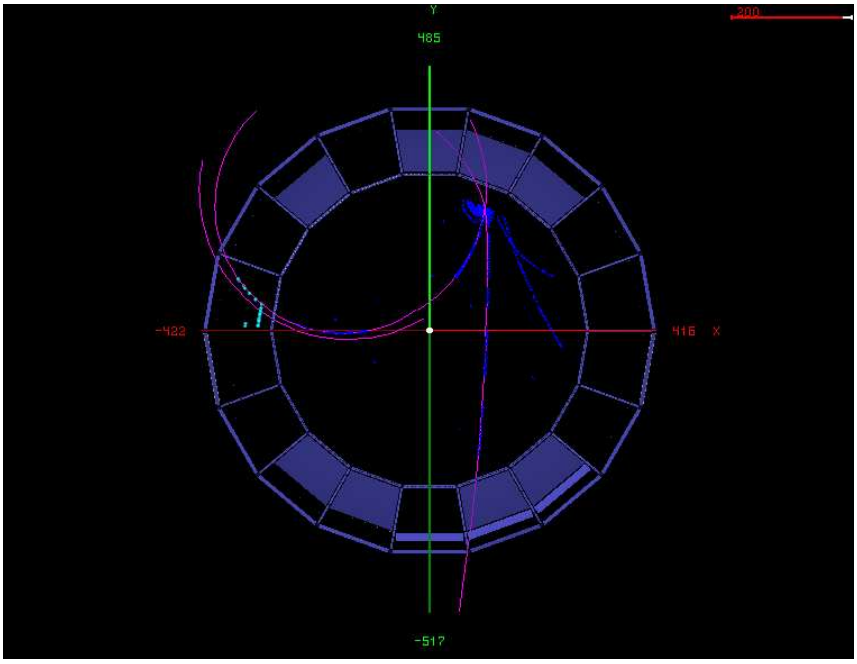

Figure 7.6: A cosmic event taken at CERN (run 62006 at 07-10-08). The detector is projected to the xy-plane. The light blue dots represent clusters found in the TRD.

associated tracklets. With the length of the drift plateau a starting value for the drift velocity is given.

In Figure 7.8, the average pulse height of the chamber in layer 2 and stack 2 is shown. The drift plateau starts in time bin 7 and ends in time bin 20. With a drift length of 3 cm this drift time yields a drift velocity of about $v_{\text{drift}} = 2.3\,\text{cm}\mu/\text{s}$. With velocities distributed around this value, the reconstruction is done for a small amount of files.

If the drift velocity is for example too high, the tracklets are steeper than the track. Only for $\phi = 0°$ the inclinations of both are the same. If the difference ϕ_{track}-$\phi_{tracklet}$ is calculated and plotted as a function of the track angle, the curve has an inclination and is zero at $\phi = 0°$. The value of the drift velocity is the value, where the slope of the curve is zero. Figure 7.9 shows this curve for different drift velocities. The slope of the fits are plotted as function of the drift velocity in Figure 7.10. With a drift velocity of $v_{\text{drift}} = 2.575\,\text{cm}/\mu\text{s}$ the linear fit of the distribution is the flattest or the fit value in Figure 7.10 is almost zero. This drift velocity is used for the reconstruction of the tracks of run 1022.

In each file about 12 000 events are stored. In about $^2/_3$ of the events, tracks are found during reconstruction. In order to avoid mis-usage of track points belonging to other tracks, only events with one reconstructed track are used. This reduces the amount of tracks to a minimum of 6 000 tracks per file. Only about 2 500 of these tracks traverse stack 2

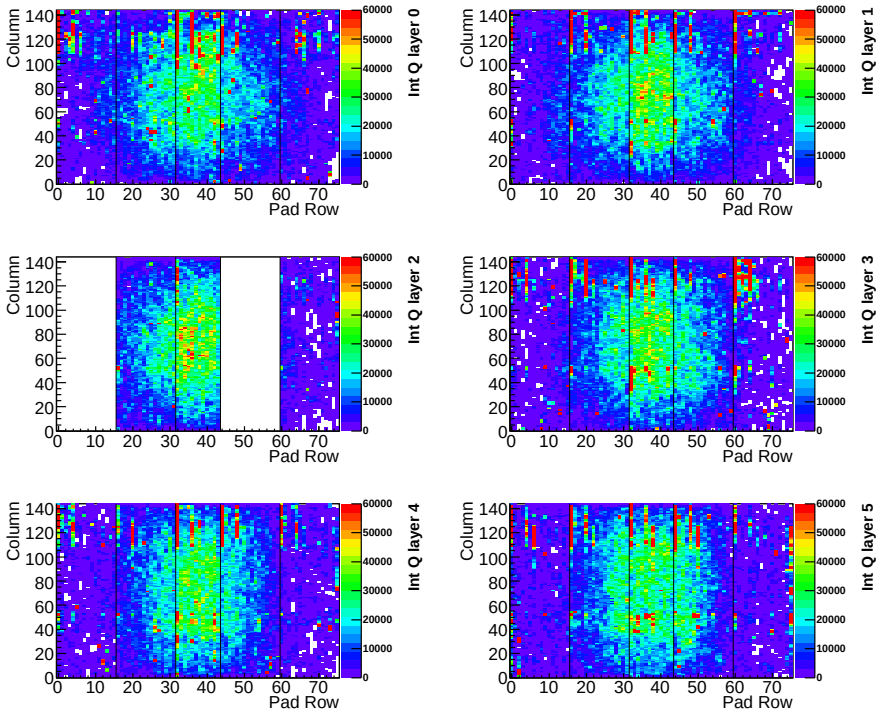

Figure 7.7: Integrated charge per read-out pad (run 1022, file 0).

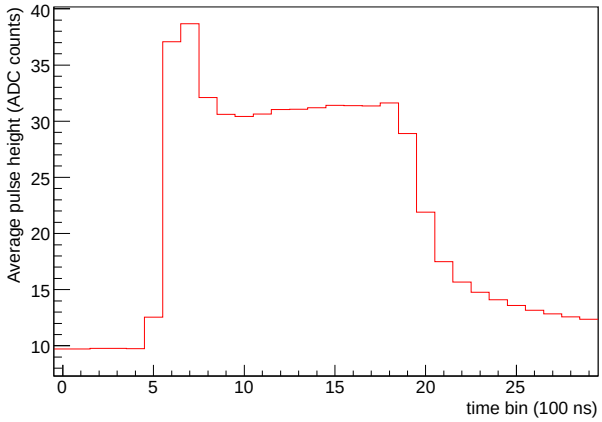

Figure 7.8: Average pulse height distribution of cosmic particles (run 1022, file 0) for the chamber of layer 2 and stack 2. The drift plateau starts in about time bin 7 and stops in time bin 20. With a drift length of 3 cm, this drift time yields a drift velocity of about $v_{\text{drift}} = 2.3\text{cm}/\mu\text{s}$.

completely. The other tracks are detected in the neighbor stack or do stack crossing. Thus, the 25 files of run 1022 provide about 60 000 tracks for the alignment procedure of stack 2.

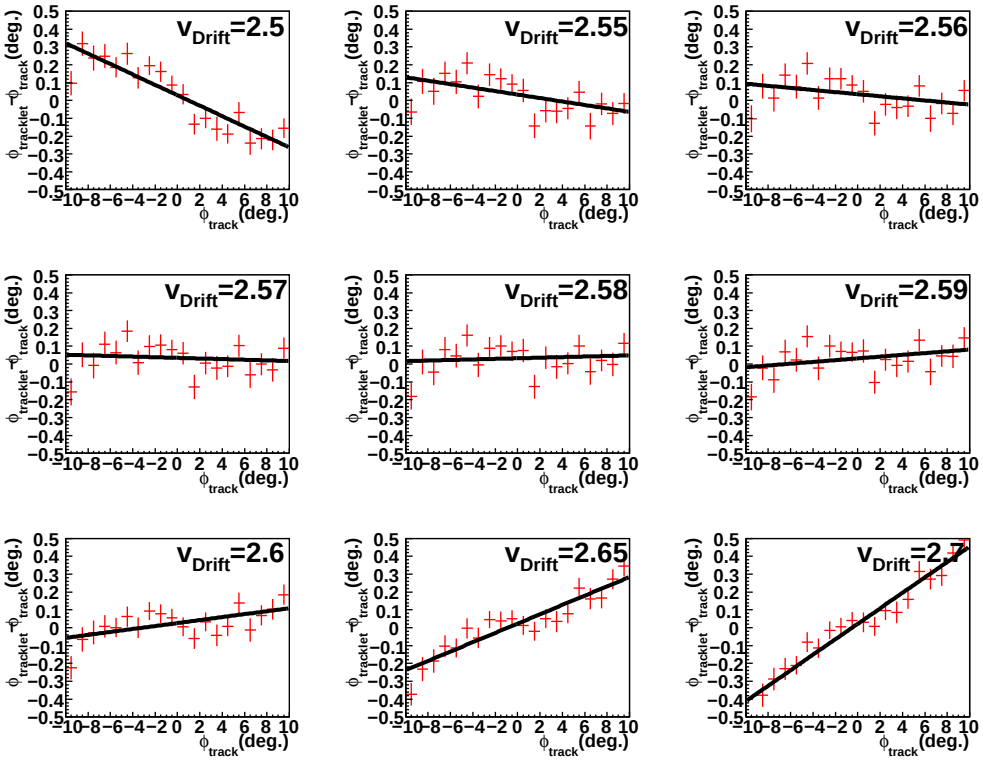

Figure 7.9: Difference of track angle to tracklet angle as a function of the track angles for various drift velocities used for the reconstruction of tracks. The unit of the drift velocity is cm/μs.

7.5.2 Track Properties

The quality of the alignment is directly influenced by the quality of the processed tracks. The quality of the tracks for the alignment is defined by the number of tracklets or clusters composing a track and the shape of the track. Since for cosmic ray data taken in Münster a straight line fit is estimated to describe the trajectory, the fit quality depends on the straightness of the tracks. Curved tracks, such as tracks from multiple scattering particles, have to be excluded.

In order to improve the quality of the used data set, the following track properties are investigated as selection criteria: number of tracklets, number of clusters, the deposited energy of a track, which can be related to the probability for multiple scattering, and a difference between track angle and tracklet angle. In addition, a mis-usage of tracklets belonging to other tracks which are falsely reconstructed as associated tracklets can be suppressed with this cut.

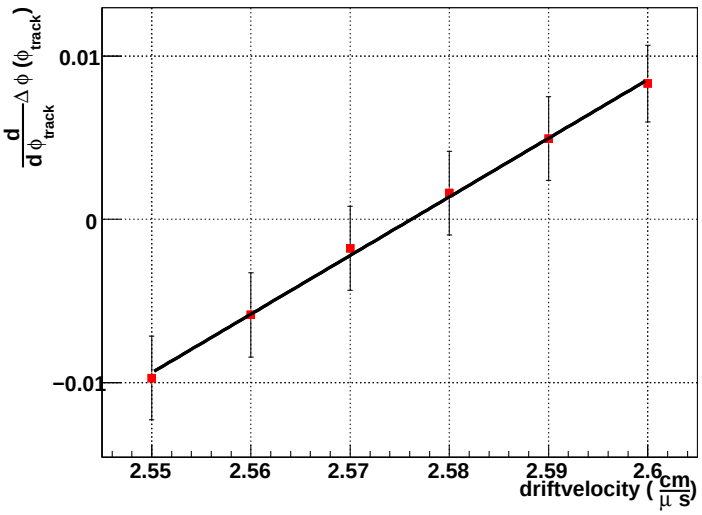

Figure 7.10: The distributions in the Figure 7.9 are fitted with a line fit. The slope is a function of the drift velocity. At about $v_{drift} = 2.575\,cm/\mu s$ the slope is zero.

7.5.3 Choice of a Reference System for Alignment in a Stack

For the alignment of objects, a reference system is necessary. In the Münster setup just the super-module with no other tracking detectors is available. Therefore, chambers of the super-module have to be used as reference.
Without fixation of the alignment constants for the chambers, the stack is not well defined. The calculated position of the stack could drift in the minimization process to each direction. No stable alignment constants can be provided like that. A fixation of one chamber is not enough, either. A stack fixed only in one layer is able to tilt over and rotate around its main axis. Both approaches, no fixation and one chamber as reference system, were tested without providing stable results. The conclusion is to fix two chambers. In the following, the outer two chambers of a stack are completely fixed. These two chambers will be aligned later to the TRD frame. As reference volumes for the reference fit, all chambers of the stack are defined. The alignment procedure iterates over the inner chambers, which are movable in their own alignment step.
This approach is chosen, although it reduces the number of chambers, which can be aligned, because it provides stable alignment constants. But attention has to be paid that misalignments of the outer chambers to each other can worsen the alignment results of all chambers.
In Figure 7.11, the principle of the alignment procedure in one stack is presented. The outer chambers of layer 0 and layer 5 of the TRD super-module are fixed. The inner chambers as volumes-to-be-aligned can be shifted and tilted in different directions.

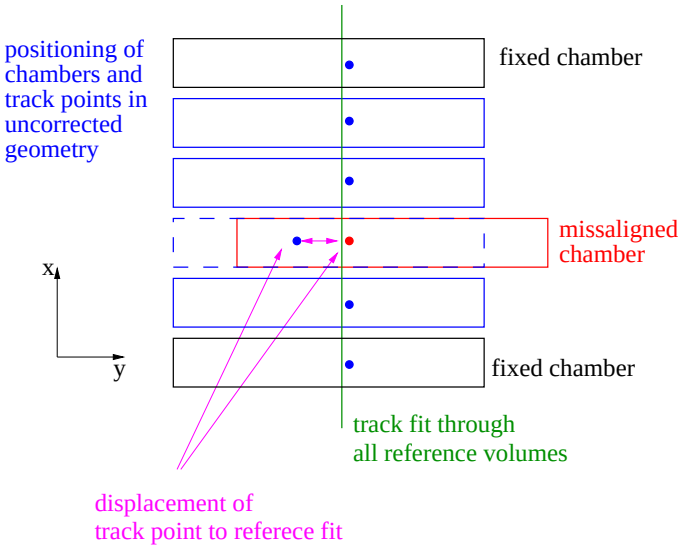

Figure 7.11: One stack of a TRD super-module projected to the xy-plane. The outer chambers are fixed. As example, one chamber is misaligned. Due to the misalignment a corrupted position of the track point is calculated during conversion of signals to space points. By calculating the difference of the positions of the track points to the positions of the reference fit defined by the track points of all reference volumes and minimizing the residuals, a position closer to the real one of the chamber can be found.

7.5.4 Choice of a Minimization

Three types of minimization procedures are available in the official framework. They are called `AliTrackResidualsChi2`, `AliTrackResidualsFast`, and `AliTrackResidualsLinear`. Each of them was tested for the TRD alignment. Since the linear method does not provide stable results for TRD alignment, only the other two methods are used [Mis07].
The computing time for the χ^2 method averages to 34 s for the alignment step of one chamber, for the fast method the computing time is just 3 s. But one major advantage of the χ^2 method is the possibility of fixing alignment constants. In order to leave this option open, the method `AliTrackResidualsChi2` is used in the following analysis.

7.5.5 Evaluation of Success of Alignment

There are two types of values, which can be used to observe the success of the alignment, which are presented in the following.

One control parameter of the alignment process is the distribution of the alignment constants themselves calculated for many data sets. Especially two alignment constants can be employed to evaluate the quality of the given set of data. These are $\phi_{r,\mathrm{shift}}$ and z_{tilt}. These two constants can be converted into a shift in y-direction of the global geometry

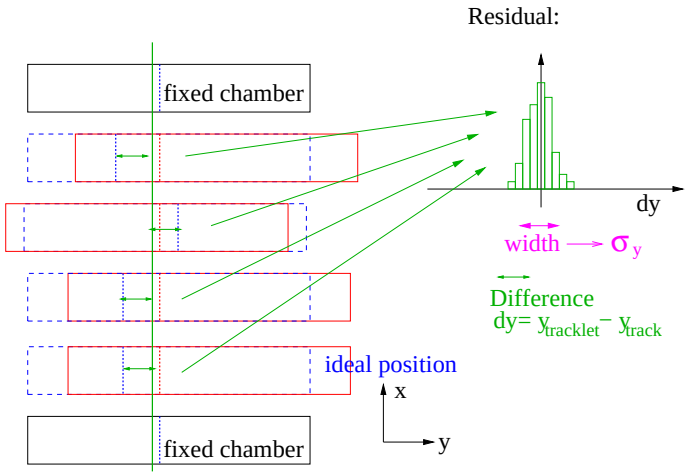

Figure 7.12: The width of the residuals in y-direction is a control parameter of the alignment. It is very small, if the chamber positioning in the corrected geometry is close to the ideal one.

for super-modules placed at $\alpha = 0°$ as seen in Figure 7.2. Since the y-resolution is good compared to the resolution of the other directions and important for the p_T-resolution of the detector, changes in y have to be investigated.
The other value is $\sigma_{y-\text{residuals}}$, which is the width of the residuals in y-direction. With the correct positioning of the chambers, the width should be minimal. For the same reason as before just the y-direction is analyzed. Figure 7.12 shows the principleof this control parameter.

7.5.6 Resulting Misalignments

The resulting misalignment of single chambers can be observed by their alignment constants. The alignment is processed with all files of run 1022. Each results in 6 alignment constants. Since the results differ for different input files, the result can be combined to a mean value of an alignment constant and the width of its distribution.
The 6 mean values and the widths of the alignment constants for each of the 4 inner chambers of stack 2 are shown in Table 7.1. The corrections calculated for the chambers are rather low. The assembly of the super-modules was done with a high precision.
In addition, the width of the residuals in y-direction can be determined. The results for the four chambers are presented in Table 7.2.

	Chamber 13	Chamber 14	Chamber 15	Chamber 16
Volume path	sm00/st2/pl10	sm00/st2/pl11	sm00/st2/pl12	sm00/st2/pl13
ID	20482	22530	24578	26626
$\phi_{r,\text{shift}}$(cm)	0.0370±0.0074	0.0295±0.0110	-0.0151±0.0177	-0.0121±0.0253
z_{shift}(cm)	-0.0330±0.1049	-0.0612±0.1049	0.0502±0.1490	0.1246±0.2050
r_{shift}(cm)	0.0509±0.0244	0.0637±0.0262	0.0630±0.0384	0.0615±0.0536
$\phi_{r,\text{tilt}}$(deg.)	0.0094±0.0655	0.0335±0.0284	0.0578±0.0691	-0.0038±0.0753
r_{tilt}(deg.)	0.0038±0.0007	0.0032±0.0014	-0.0005±0.0016	-0.0001±0.0023
r_{tilt}(deg.)	0.0825±0.0115	0.1066±0.0100	0.1142±0.0239	0.1513±0.0290

Table 7.1: Alignment results for stack 2 of super-module III. The results are calculated with 25 different files. The alignment was processed once for each file. In the volume path the layer number for TRD starts with plane 9 (layer 0) and ends with plane 14 (layer 5).

	Chamber 13	Chamber 14	Chamber 15	Chamber 16
Volume path	sm00/st2/pl10	sm00/st2/pl11	sm00/st2/pl12	sm00/st2/pl13
ID	20482	22530	24578	26626
σ_y(cm)	0.1230±0.0046	0.0895±0.0026	0.1253±0.0026	0.1532±0.0047

Table 7.2: The widths of the residuals calculated for each chamber of stack 2 of super-module III.

7.5.7 Storing misalignments via AliTRDalignment in OCDB

The alignment constants of the aligned volumes can be combined to AliAlignObjects and saved in the OCDB. The file containing the alignment objects is placed at $ALICE_ROOT/TRD/Align/Data and is called RunW_X_vY_sZ.root. W and X define the run range, in which the alignment objects are valid, and Y and Z define the version and the subversion of the information, since the information can be updated. $ALICE_ROOT is the directory, where the used AliRoot version is placed. The ideal geometry and the information in the OCDB are combined to a geometry closer to the real one and are used in the reconstruction.

7.6 Optimization of the Alignment Method

In the following, different criteria are investigated to select data for alignment. With a better data set the result of the alignment should be improved. In the following steps, the width of the residuals σ and all 6 alignment constants $\phi_{r,\text{shift/tilt}}$, $z_{\text{shift/tilt}}$ and $r_{\text{shift/tilt}}$ are calculated. First, this is done to find the optimal number of iterations and the optimal number of tracks for the alignment. After that, the constants and the width of the residuals are analyzed for different data sets. The data sets differ in their composition, characterized by the number of tracklets per track, the number of clusters per track and so on. More tracklets per track provide more information for the alignment. Therefore, they are more useful for the alignment. The sharper the cuts, the fewer tracks are in the file.
In this step, a trade-off has to be made. On the one hand, it is useful to have well defined and straight tracks for the calculation. On the other hand, as many tracks as possible should pass the cut, because a large number of tracks provides a better accuracy. In this context a compromise has to be found defining track properties for the selection. These will be used as cuts in the `PointSelector` process.

7.6.1 Number of Iterations

The alignment is processed several times for each chamber. In each iteration, the alignment constants get more precise. The number of iterations, after which the values have converged sufficiently, are evaluated in the following. Since the data sets provide in average 2500 tracks, the calculated iteration number uses to this number of tracks.
Figure 7.13 shows the alignment constants as a function of the number of iterations averaged over the results of all processed files. The entries of the profile histograms are results for all inner chambers of stack 2 in super-module III, which are the chambers of layer 1 to layer 4. The chambers are called L1S2, L2S2, L3S2, and L4S2 in the following.
The calculation is done 50 times. The means of all alignment constants change more at the beginning of the iterations. At high iteration numbers the means of the constants converge to the final values. In addition, the error bars of the alignment constants are constant at high iteration numbers. The error bars represent the width of the value distribution determined by combining the results for all 25 processed files. This represents how reproducible the results of the procedure are, which gives a hint to the resolution of the detector.
A reasonable number of iterations is given by the condition that no further change of the constants can be noticed. This definition is valid for all alignment constants.
In addition, the width of the residuals in y-direction can be observed. Figure 7.14 shows the σ_y for the four inner chambers. Except for a small increase of σ_y within the first iteration steps, the value stays nearly constant. This value does not give the same good hint to the best iteration step as the change of the alignment constants does. The increase of the σ_y of the chambers L4S2 and L2S2 may be due to an artifact in the minimization

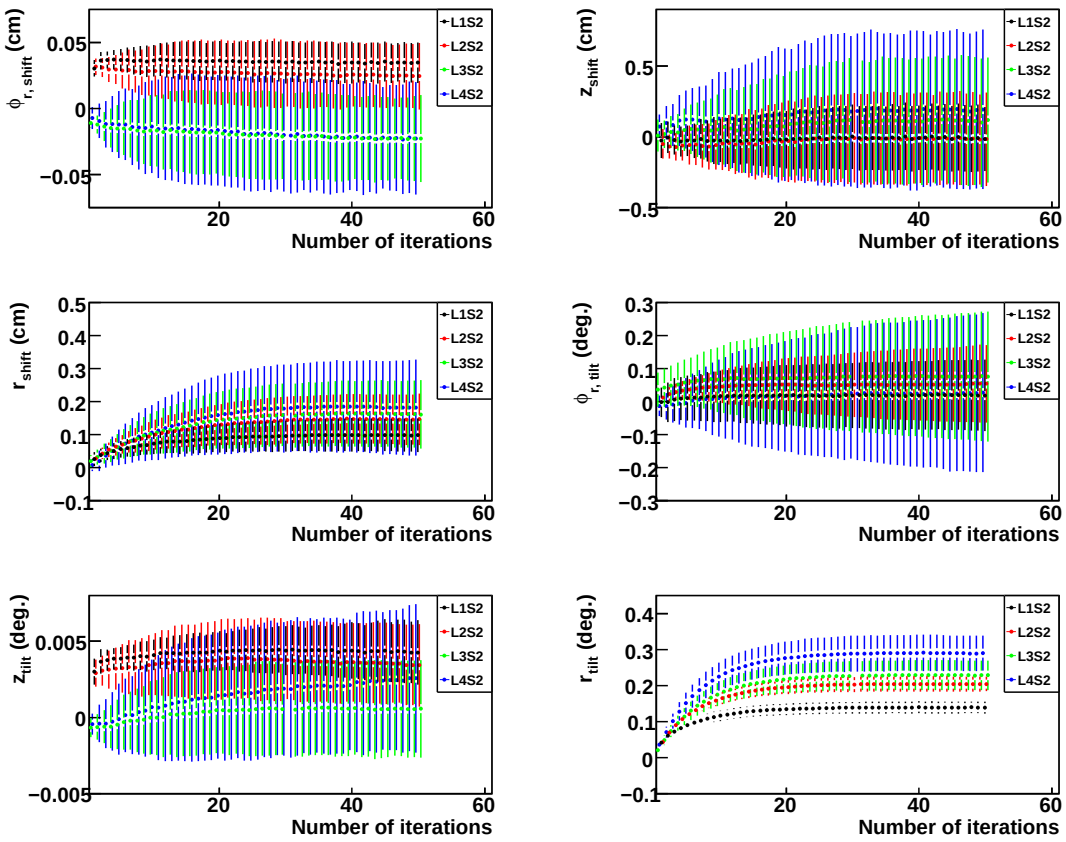

Figure 7.13: Alignment constants as a function of the number of iterations. The results for the inner chambers of stack 2 in super-module III are shown. The error bars represent the RMS of 25 measurements.

process caused by limited statistical accuracy.

For different chambers the σ_y has different values. The residuals of the chamber in layer 4 are much wider distributed than the residuals for layer 2 for example. This can be a hint that fewer tracklets are measured in layers with wide residuals than in layer with narrow residuals. This can be due to different gas mixtures for example. Fewer tracklets are converted to fewer track points which can be aligned to the reference fit of the reference volumes. The chambers would not be that precisely defined. A dependence of the residuals on the number of tracklets per track is investigated in Section 7.6.3.

The information from Figure 7.13 leads to 30 iteration steps as sufficient number for the alignment with cosmic ray data. After that many iterations, no further improvement of the constants within their error bars can be observed. In the following, 30 iteration steps are used for the analysis.

Since the behavior of the constants for different chambers is similar to each other, in the following sections just the constants for one chamber are presented, if necessary.

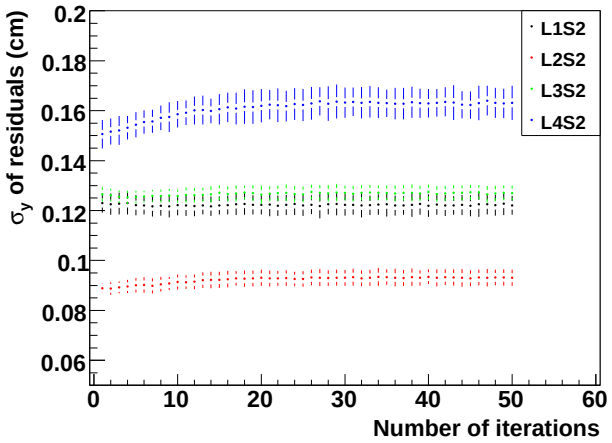

Figure 7.14: The width of the residuals as a function of the number of iterations. The values are averaged for all processed files, but show only the accuracy of the calculation with one file. The minimization method minimizes the χ^2 of the track fit through the track points. The error bars represent the RMS of 25 measurements.

7.6.2 Number of Tracks Used for the Calculation of Selection Criteria

With the Cosmic Trigger in Münster, a higher rate of cosmic particles compared to the cosmic rate in the pit of ALICE can be measured. In Münster the super-modules are placed at ground level, while at P2 most of the particles are stopped in the massive rock between the surface and ALICE. With that high rate of cosmic particles it can be estimated, how many tracks are necessary to find reliable and stable alignment constants. With this number a lower limit for the data taking time, especially for the data taken at P2, can be calculated. Since it is no problem to get many cosmic tracks in Münster, it has to be evaluated, how many tracks are reasonable to process. An optimal number of tracks for the analysis can be derived to reduce computing time.

In Figure 7.15 the width of the residuals in y-direction as a function of the used number of tracks is presented for the inner chambers of stack 2. In the calculation the values from the 30^{th} iteration are employed. The calculation is done with 10 different data sets, which are combined data from the 25 files of run 1022. One file alone offers too few tracks for this analysis.
For all chambers the fluctuation around the mean values of σ_y decrease with increasing number of used tracks. After 2000 processed tracks a state, after which no further improvement is reached.

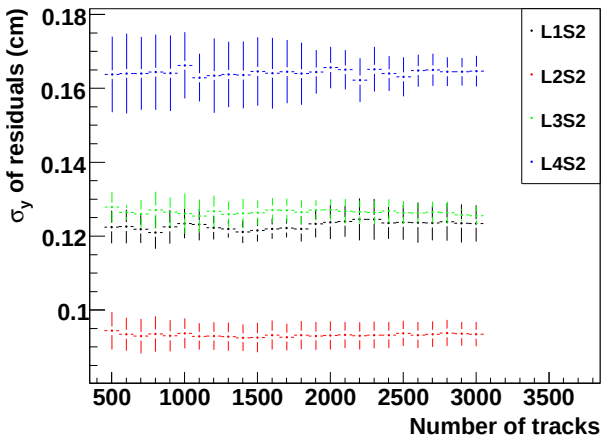

Figure 7.15: Width of the residuals after 30 iterations as a function of used tracks for the 4 inner chambers of stack 2. The error bars represent the RMS of 25 measurements.

In Figure 7.16, the alignment constants of the chamber in stack 2 and layer 2 are plotted versus the number of processed tracks. The constants $\phi_{r,\text{shift}}$, $\phi_{r,\text{tilt}}$, r_{shift} and z_{tilt} show the behavior that their widths decrease with increasing numbers of tracks. The remaining values also vary with the number of tracks, but the distribution gets even wider. As remarked in Chapter 7.5.5, especially the constants $\phi_{r,\text{shift}}$ and z_{tilt} can be employed to evaluate the quality of the given data set, because they directly influence the y-coordinate which has the best resolution. Like σ_y in Figure 7.15, also their distributions get narrow. Since the evolution of the constants' values and distributions is not as clear as the evolution of the σ_y, the optimal number of processed tracks is deduced just by σ_y. Here, a value of 2000 tracks seems to be reasonable.

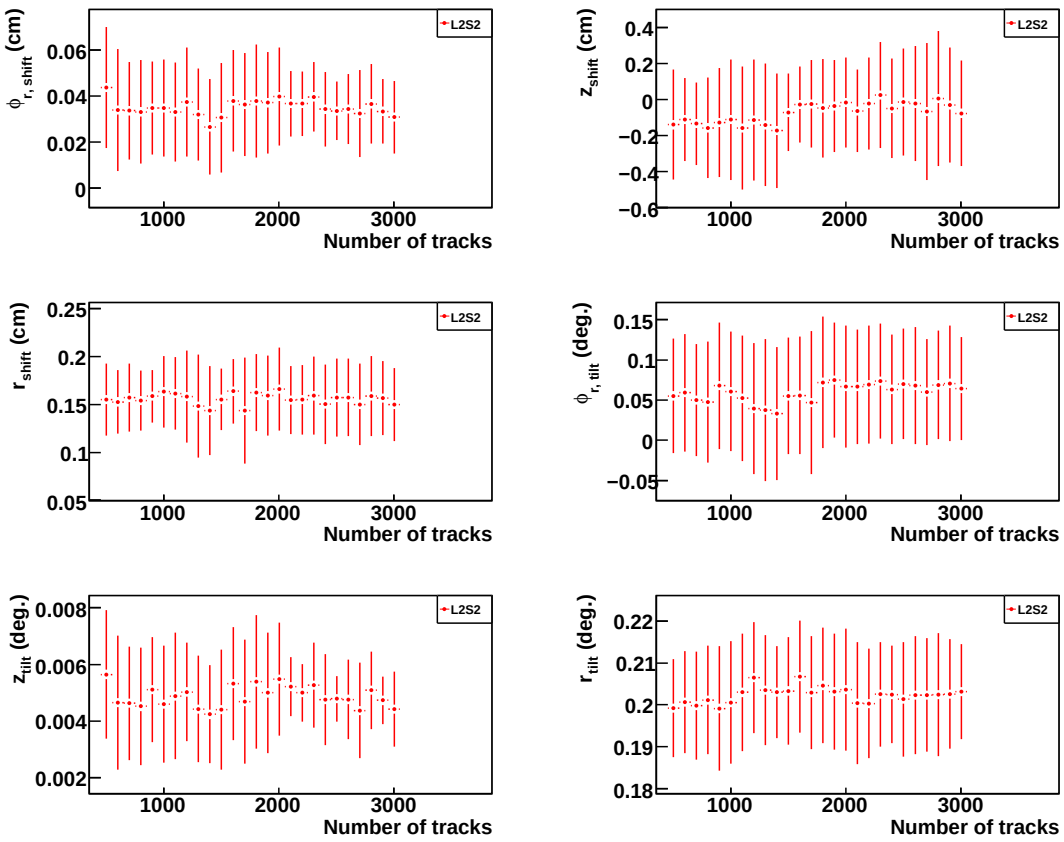

Figure 7.16: Alignment constants after 30 iterations as function of the used tracks for the chamber of stack 2 and layer 2. The error bars represent the RMS of 25 measurements.

7.6.3 Minimum Tracklets Number

Limited by the geometry, a TRD track is composed of 6 tracklets at maximum. A minimum of 4 tracklets is required to build a track. With less than 4 tracklets, one track could be divided into 2 tracks with three tracklets each. This would allow to build two tracks out of one true track by mistake. In Figure 7.17, the number of tracklets per track is presented for cosmic ray data from run 1022.

With a set of 6-tracklet tracks, the quality of the set for the alignment should increase because more tracklets per chamber can be used for the calculation. Each tracklet is converted to a track point in the `PointSelector`. If a set contains a lot of tracks with 4 and 5 tracklets, the real number of track points decreases and the alignment constants could be less stable at a fixed number of used tracks.

Figure 7.17 shows the distribution of tracklets per track in the given data set. The data set provides just about 13 % of tracks with 6 tracklets. A cut on six tracklets would decrease the number of tracks per file to 325. A cut on this value is only reasonable if

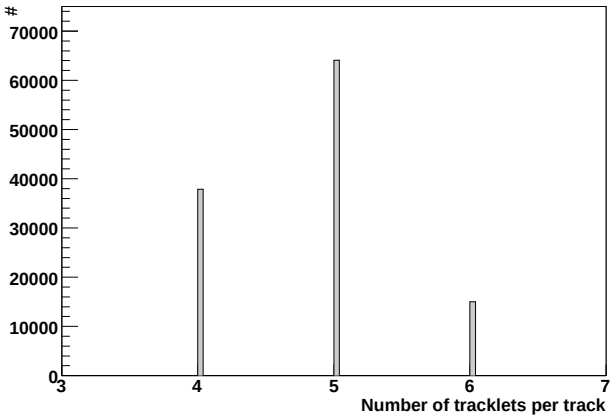

Figure 7.17: Distribution of number of tracklets building one track.

many cosmic tracks are available.

In Figure 7.18, the σ_y of the y residuals is drawn as a function of the minimum number of tracklets in the processed data sets. Figure 7.19 shows the alignment constants as a function of the minimum tracklet number building a track. The used data sets are defined by the cut on the lowest tracklet number that is accepted for track building. For comparison, the same amount of tracks is used for all data sets. That are about 2000 tracks per file.

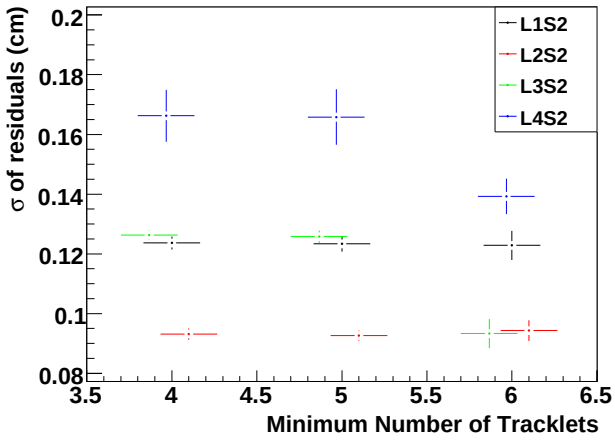

Figure 7.18: Width of residuals as function of the minimum used tracklets for the 4 inner chambers of stack 2. The error bars represent the RMS of 4 measurements.

For a data set consisting of 6-tracklets tracks only, the widths of the residuals differ from the widths calculated with the other data sets. The distribution is shown in Figure 7.18.

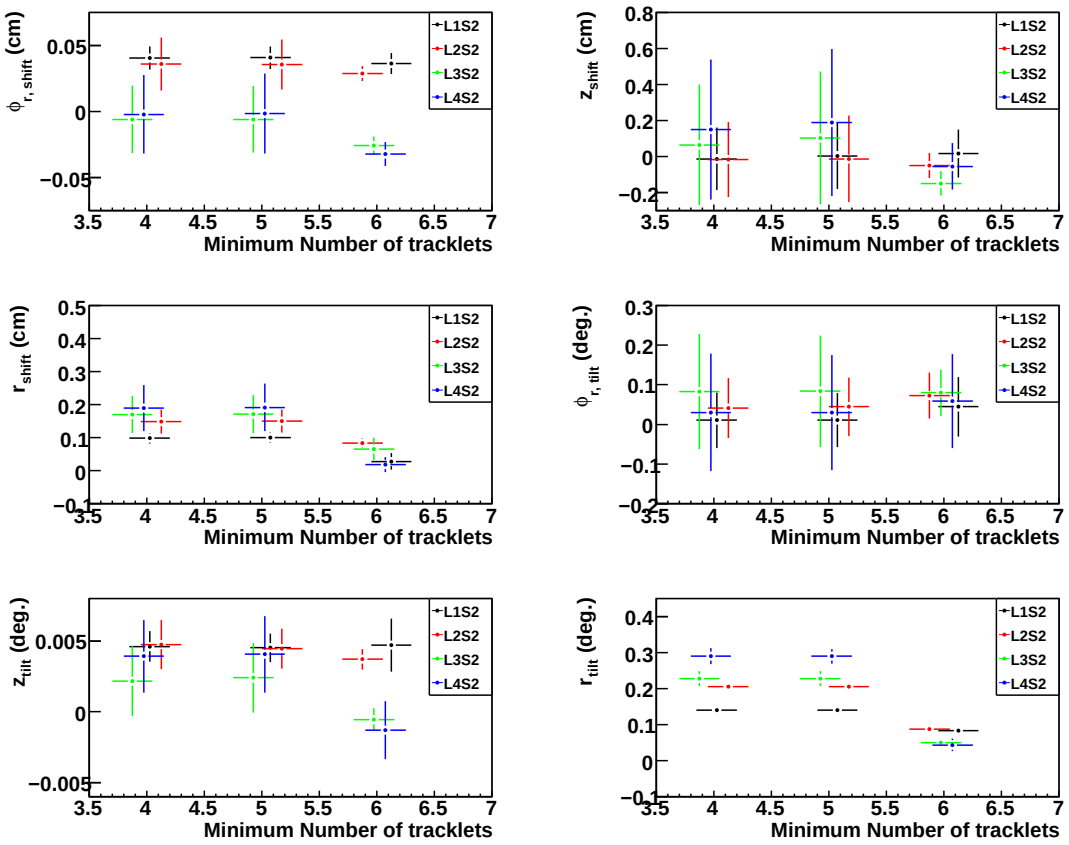

Figure 7.19: Alignment constants as a function of the cut on a minimum of used tracklets for the 4 inner chambers of stack 2. The error bars represent the RMS of 4 measurements.

The widths of the residuals σ_y of the different chambers are closer to each other for the data set defined by 6 tracklets and the value σ_y is lower or stays constant. As already expected, this shows that some chambers are less defined in the alignment with 4 and 5-tracklet tracks, because fewer tracklets were found in special chambers. The width of the residuals could not shrink as fast as for the other chambers, because fewer track points for the calculation were available. In order to compare the alignment results of the chambers to each other, only 6-tracklet tracks should be used.

The evolution of the alignment constants is shown in Figure 7.19. While the width for the data sets with a minimum of 4 and 5 tracklets is similar, it is reduced in the 6-tracklet case for some constants, for the other ones it is constant.
In conclusion, a data set composed of tracks with 6 tracklets provides stable results for the alignment constants. The y residuals are up to 15 % narrower. About 13 % of the cosmic tracks pass this cut. Either many tracks are rejected in order to get stable results, or more tracks with worse properties have to be used. This has to be done, if just a low

amount of events is available. A cut on 6-tracklets is very reasonable for data taken in Münster. However, at least 2000 tracks are essential for the alignment process.

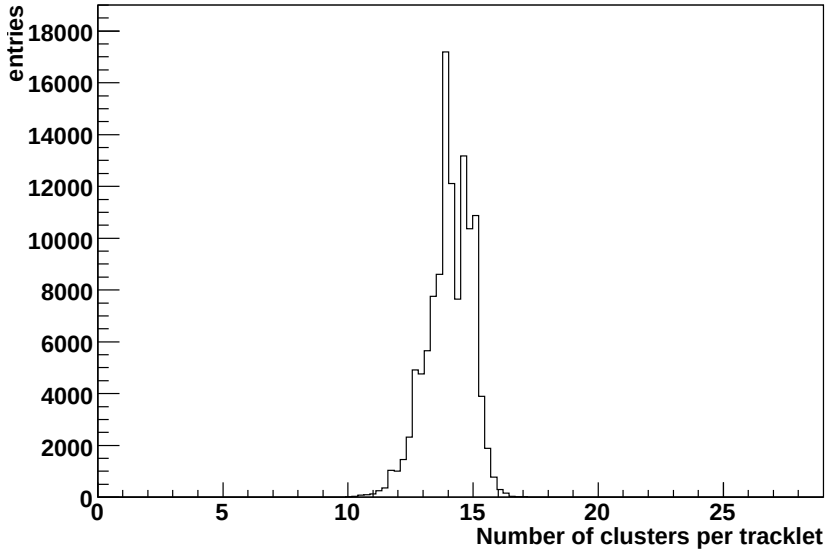

Figure 7.20: Distribution of number of clusters contained in one tracklet.

In Figure 7.20, the number of clusters per tracklet is presented. Since each tracklet is built of an amount of 14 clusters in average, it is possible to replace the cut on the tracklet with a cut on the number of clusters. A certain number of clusters eventually provides a high stability of the constants without rejecting as many tracks as the tracklet cut does. This topic is investigated in the next section.

7.6.4 Minimum Cluster Number

In Figure 7.21, the spectrum of the number of clusters per track is presented for all tracks contained in the input data. The red dashed curve represents the clusters belonging to tracks with just 4 tracklets, the blue line belongs to 5 tracklets and the magenta line is for tracks with 6 tracklets. It can be seen that the number of clusters depends on the number of tracklets per track. The distribution of the cluster number starts with about 40 clusters and ends with 100 clusters per track. The more clusters are used to build one track, the better the track is defined. As discussed in the previous section, the width of the residuals and the alignment constants themselves are calculated with different data sets.

This is shown in Figure 7.22 and 7.23. The shape of the distributions was expected, because similar results were visible as a function of tracklets. A change in the shape of the distributions appears at a value of 75 clusters. Data sets with a minimum number of 75 clusters per track provide more stable constants than the data sets with lower cluster

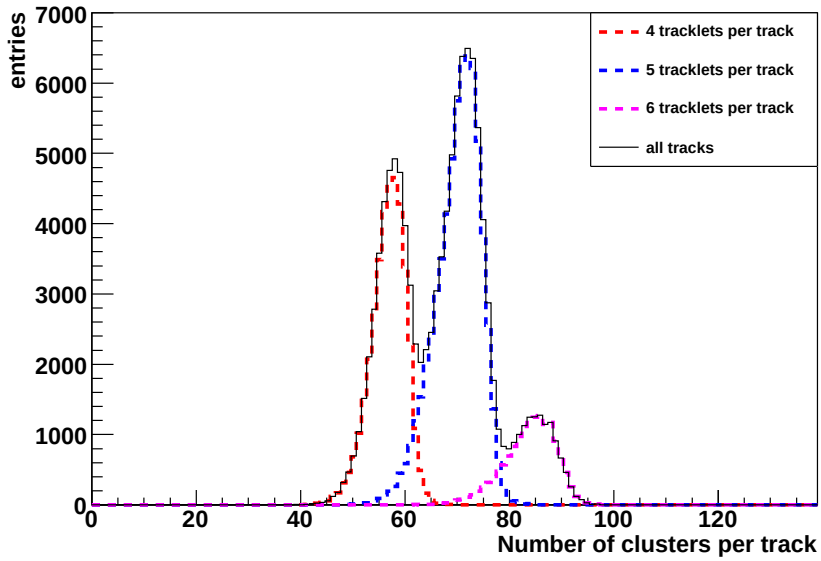

Figure 7.21: Distribution of number of clusters contained in one track.

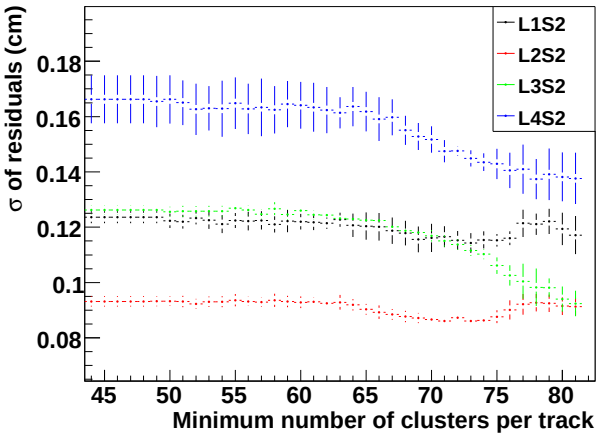

Figure 7.22: Width of residuals as function of the minimum used clusters per track for the 4 inner chambers of stack 2. The error bars represent the RMS of 4 measurements.

numbers.

While the cut on 6 tracklets leaves only 13 % of the tracks, the cut on a minimum of 75 clusters rejects just 81 % of the tracks. The remaining 19 % contain also some tracks with 5 tracklets. But these tracks are populated with many clusters compared to all other tracks with 5 tracklets. Since 5 tracklets generate only 5 track points for the alignment, the data set is not as good as the data set with just 6-tracklet tracks. In order to compare the results for different chambers, each chamber should be defined by the same amount of

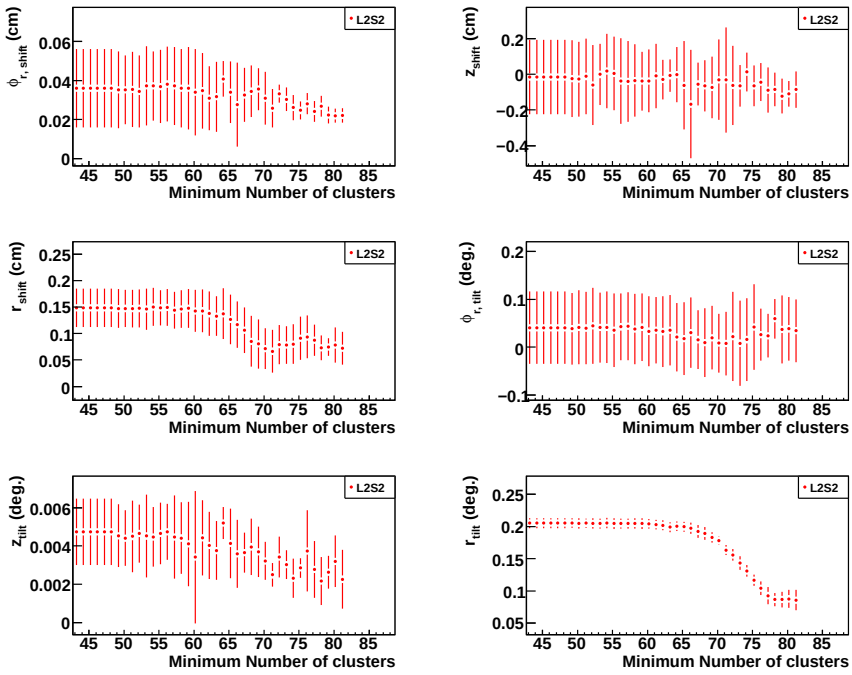

Figure 7.23: Alignment constants as a function of the cut on clusters per track for the chambers of stack 2 and layer 2. The error bars represent the RMS of 4 measurements.

track points.
The cluster cut does not replace the tracklet cut. Thus, in the following, the tracklet cut is applied to the data. The cluster cut is not applied.

7.6.5 Maximum Deposited Energy

For alignment, straight tracks are essential. Thus particles which do multiple scattering with high deflection angles should be rejected. These are low momenta particle. Possibly, low momenta particle could be identified by their energy deposit. After explaining the motivation of a cut to energy deposit in detail, this cut is investigated in the following for this purpose.

Due to multiple scattering of cosmic particles in the detector material, the track of the particles can differ from straight trajectories of the particles in the case of vacuum. For the alignment with cosmic ray data, straight tracks are required since a straight fit is used. A natural idea is to cut on the curvature of the tracks in order to get just the tracks fulfilling the condition of straightness. Due to the misalignments of the chambers, the position of some clusters are displaced to their correct position. The fitted curve through all clusters can have a curved shape, even though the cosmic track was straight. A cut

on the curvature restricts the ability of the alignment to correct the chambers' positions. Such a cut would assume that the chambers are already at the correct position. Thus, other ideas have to be invented to get straight tracks only.

If a charged particle traverses a medium, it will be deflected by many small angle scatters. They origin from multiple Coloumb scattering with nuclei of the medium. The scattering-angle distribution is roughly Gaussian for small deflection angles [Ams08].

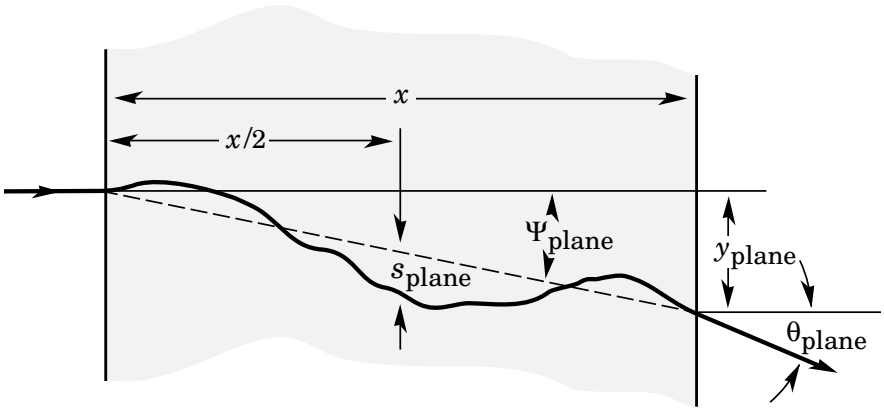

Figure 7.24: Quantities for the description of multiple Coulomb scattering in thin layers. The particle enters the material in the plane of the figure [Ams08].

We define $\theta_0 = \theta_{plane}^{rms}$, which is presented in Figure 7.24, then we can use the Gaussian approximation for the most probably central angular distribution. The width is given by

$$\theta_0 = \frac{13.6\,\mathrm{MeV}}{\beta cp} \cdot z\sqrt{x/X_0}[1 + 0.038 \ln x/X_0]. \tag{7.1}$$

Here p, β and z represent the momentum, the velocity, and the charge number of the incident particle [Ams08]. Since these are mainly muons from cosmic radiation, the charge is $z = 1$. The thickness of the scattering medium in radiation length is x/X_0. In this context, the radiation length is the mean distance that is needed for a high energy particle to lose $\frac{1}{e}$ of its energy by bremsstrahlung [Ams08]. For muons crossing a TRD chamber, an estimation of the scattering-angle can be made. The mean momentum of a single charged muon on earth surface is $4\,\mathrm{GeV}/c$ as explained in Chapter 5.1.3. β is almost 1. The radiation length of the whole TRD is $x/X_0 = 25.7\,\%$ [TP108]. For one TRD layer, this results in $x/X_0 = 4.3\,\%$. With all these values, θ_0 is

$$\theta_0(p\,\mathrm{MeV}/c) = \frac{13.6\,\mathrm{MeV}}{1 \cdot c \cdot p\,\mathrm{MeV}/c} \cdot 1\sqrt{0.043}[1 + 0.038 \cdot \ln 0.043] \tag{7.2}$$

$$= \frac{1}{p} \cdot 6.2 \cdot 10^{-4}\,\mathrm{rad}, \tag{7.3}$$

with p in units of MeV/c. For higher particle momenta, the scattering angle is smaller. For two momenta, the angles are calculated:

$$\theta_0(4\,\mathrm{GeV}/c) = 0.035^\circ, \tag{7.4}$$

$$\theta_0(500\,\mathrm{MeV}/c) = 0.284^\circ. \tag{7.5}$$

Particle with low momenta have larger deflection angles in each detector layer. Due to this deflection, it is possible that the reconstructed tracks get a curved shape. These tracks should be rejected.

The possibility of a particle with very low momenta to have a huge energy deposit is high. The energy loss $\mathrm{d}E/\mathrm{d}x$ of a particle in a medium can be described with the Bethe-Bloch equation. The behavior of the function is shown in the left panel of Figure 7.25.

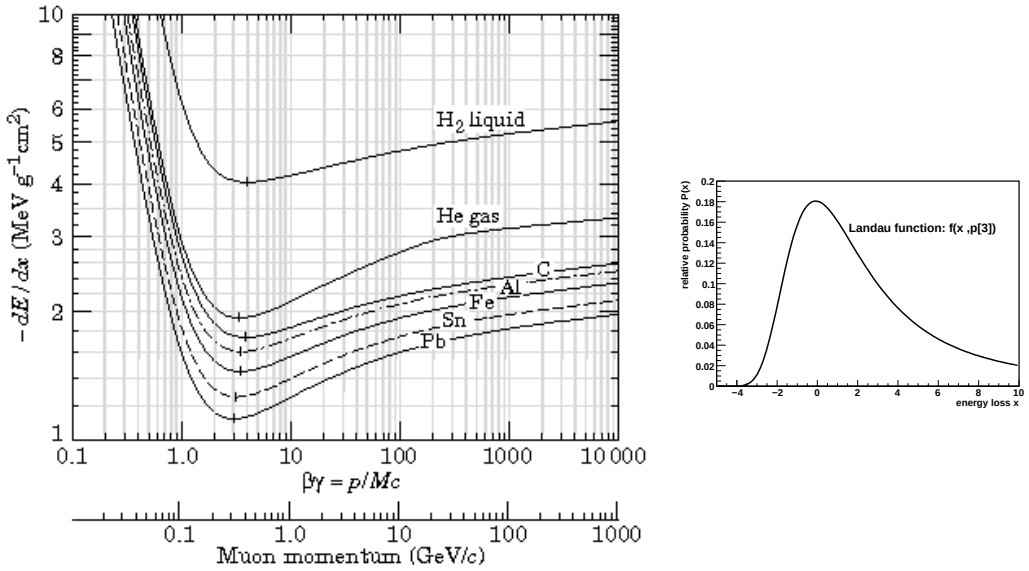

Figure 7.25: Left panel: mean energy loss rate in liquid (bubble chamber) hydrogen, gaseous helium, carbon, aluminum, iron, tin, and lead. Radiative effects, relevant for muons and pions, are not included. They become significant for muons in iron with $\beta\gamma \gtrsim 1000$, and at lower momenta for muons in high-Z absorbers [Ams08]. Right panel: an example for a landau distribution.

The momentum of particles can be described in units of $\beta\gamma = p/(mc)$. The mass of a muon is $m = 105.6\,\mathrm{MeV}/c^2$. Thus a 4 GeV/c muon has a $\beta\gamma$ of

$$\beta\gamma = \frac{p}{m \cdot c} = \frac{4000\frac{\mathrm{MeV}}{c}}{105.6\frac{\mathrm{MeV}\cdot c}{c^2}} = 37.8. \tag{7.6}$$

Starting at low momenta, the muons lose in average the most energy. The energy loss is minimal for $\beta\gamma = 3$ or $p = 300\frac{\mathrm{MeV}}{\mathrm{c}}$ and increases with increased momentum again. At

each given momentum the energy loss is distributed like a Landau distribution. A Landau distribution is shown in the right panel of Figure 7.25. Thus also particles with momenta around 300 MeV/c could deposit a huge amount of energy, but the probability to deposit much energy is higher at lower momenta.
In order to reject a large amount of particles with low momenta, a cut on deposited energy can be applied. But one has to be aware of that also a few high momenta particles could be rejected like that. In the following, the deposited energy of a track is used as selection criterion for the used tracks.

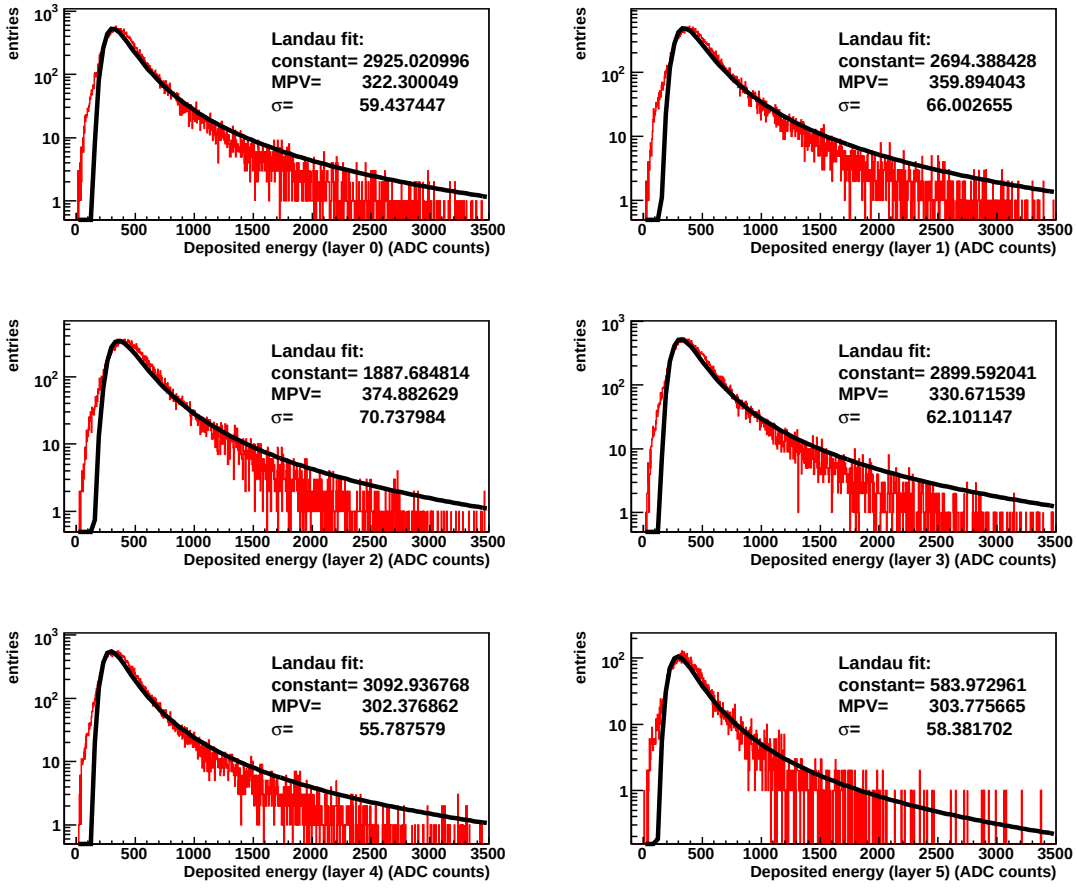

Figure 7.26: Distribution of deposited charge in the six TRD layers.

In Figure 7.26 the deposited energy of a particle for each layer is shown. The distribution of deposited energy can be fitted with a Landau distribution. Since the measured energy deposit is generated of a mixture of particles species in a wide range of momenta, the Landau fit does not exactly describe the distribution. In Figure 7.27 the sum of the energy deposits of the particles normalized to the most probable values of the deposit per layer is plotted.
The sum of all normalized energies deposited by a particle should not be too high, because

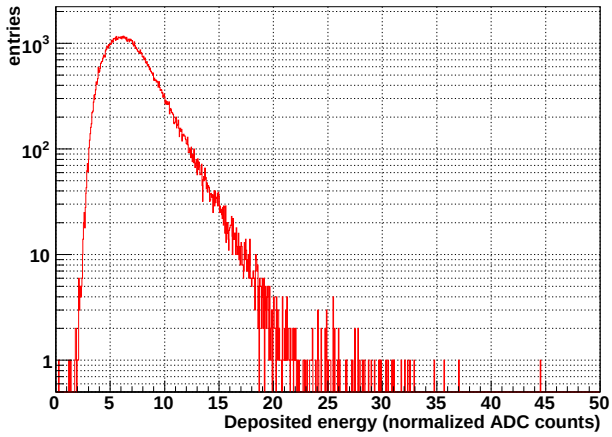

Figure 7.27: Distribution of the sum of the normalized deposited charge of all TRD layers. The deposited charges of the layers are normalized to the most probable value of their Landau distributions. The results of the layers are added.

this can be a sign for multiple scattering. Since also particles with high momenta, which scatter but only with small angles, can be rejected like that, the following analysis is just a test. If more particles with low momenta are rejected by a cut to the deposited energy, which would result in improved alignment results, the cut should applied. Otherwise, another approach has to be found.

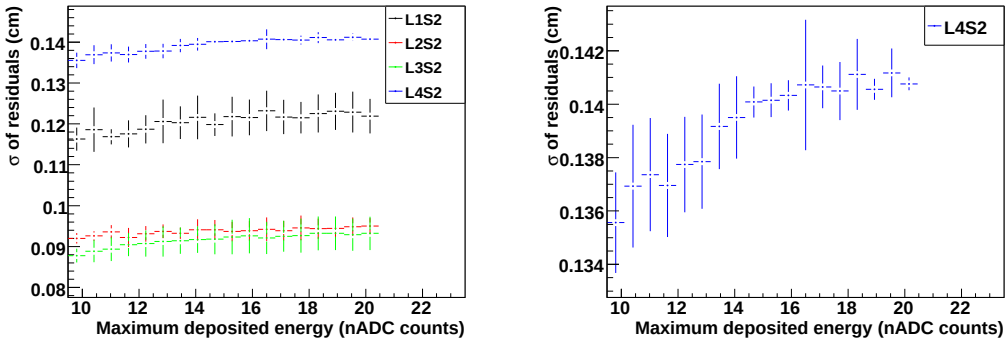

Figure 7.28: Width of residuals as function of the used maximum deposited energy per track for the 4 inner chambers of stack 2 and of the chamber of stack 2 and layer 4 alone. The error bars represent the RMS of 4 measurements.

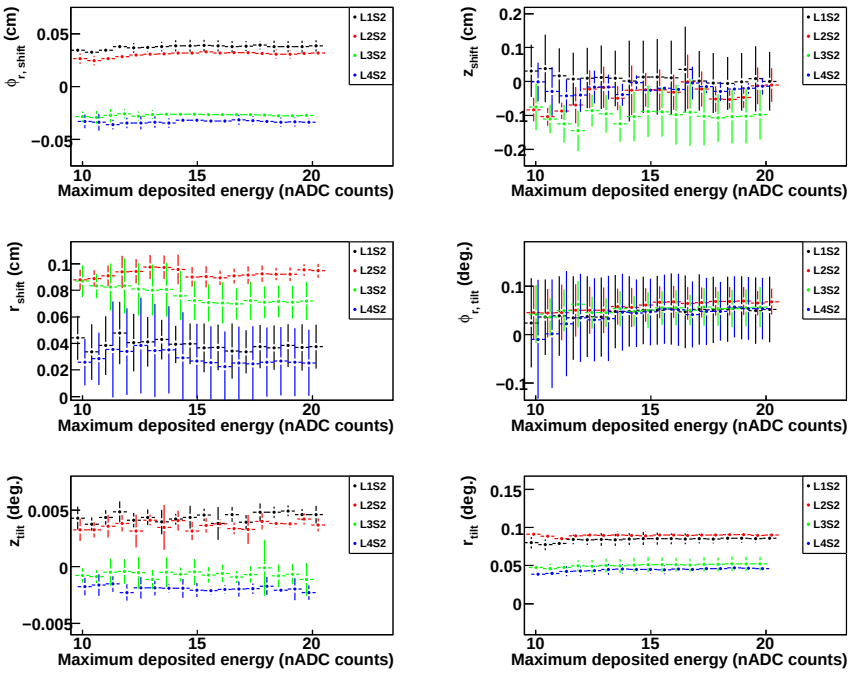

Figure 7.29: Alignment constants as function of the maximum deposited energy per track for chambers of stack 2 and layer 4. The error bars represent the RMS of 4 measurements.

For the analysis only tracks with an energy deposit much larger than the most probable value of the distribution are cut. In Figure 7.28 the width of the y residuals is shown. The lower the maximum deposited energy, the lower is the value of σ_y. But by rejecting for example 25 % of all data with a cut on 10 normalized ADC counts, only a reduction of up to 7 % of the σ_y is reached. The alignment constants shown in Figure 7.29 stay nearly the same for the different data sets.
Since the improvement is low by cutting to this measure, another approach to suppress such tracks from multiple scattering is tested in the next section.

7.6.6 Maximum Difference Between ϕ_{track} and ϕ_{tracklet}

As discussed before, for the alignment procedure straight tracks are essential. With increased difference between the track angle and the angle of the tracklet, the probability of the track to be straight decreases. Since the inclination of the tracklet and the track depends strongly on the drift velocity, this was calibrated before reconstruction.
In Figure 7.30, the distributions of the angles ϕ of tracks and tracklets, the difference of both as a function of the track angle, and the distribution of the difference is presented. Only the angle ϕ is analyzed, because this is the angle in direction of y, which is the crucial direction for the p_{T} resolution. The spectrum of $\phi_{\text{track}} - \phi_{\text{tracklet}}$ has a range of $\pm 10°$. The maximum allowed value of the difference has to be evaluated, such that many tracks are left after cutting, but candidates with sharp bends are rejected.

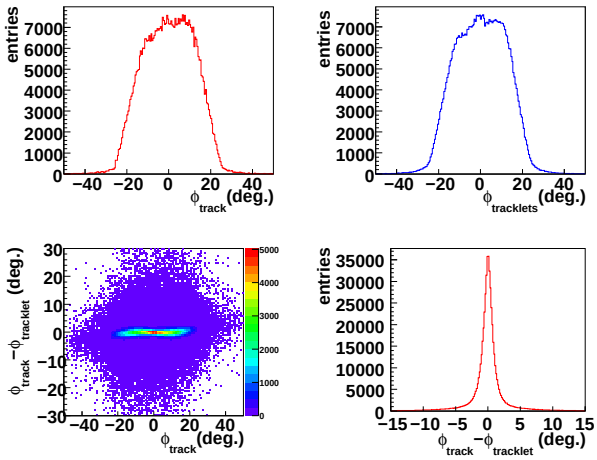

Figure 7.30: Distribution of the track angle ϕ provided by the TRD track and the tracklet. Moreover a correlation and the difference between the values are presented.

In the Figures 7.31 and 7.32 the results are presented as function of the maximum allowed difference $\phi_{\text{track}} - \phi_{\text{tracklet}}$. A range of $\Delta\phi = 10°$ is used for the analysis, because the major part (98 %) of the tracks have a $\Delta\phi$ in this range.
With decreased difference in ϕ, the width of the residuals σ_y gets smaller. The sharper the cut, the narrower is the distribution of the residuals. But the amount of tracks is reduced not as much as in the approach dealing with deposited energy. For example a cut on ± 5 % decreases the width of the y residuals to about 90 % of its start value, while the low amount of only 8 % of the remaining tracks are rejected. A cut on $\Delta\phi = 5°$ can be applied.
Combined with the cut on 6 tracklets per track, now a fraction of about 12 % of the starting data set passes the cuts.

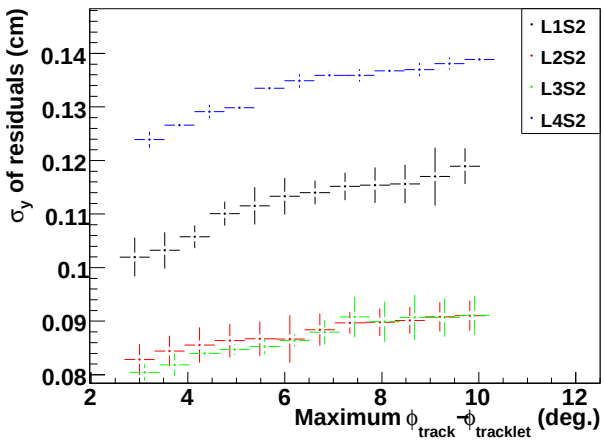

Figure 7.31: Width of residuals as function of the used data set with maximum difference in track angle to tracklet angle for the 4 inner chambers of stack 2. The error bars represent the RMS of 4 measurements.

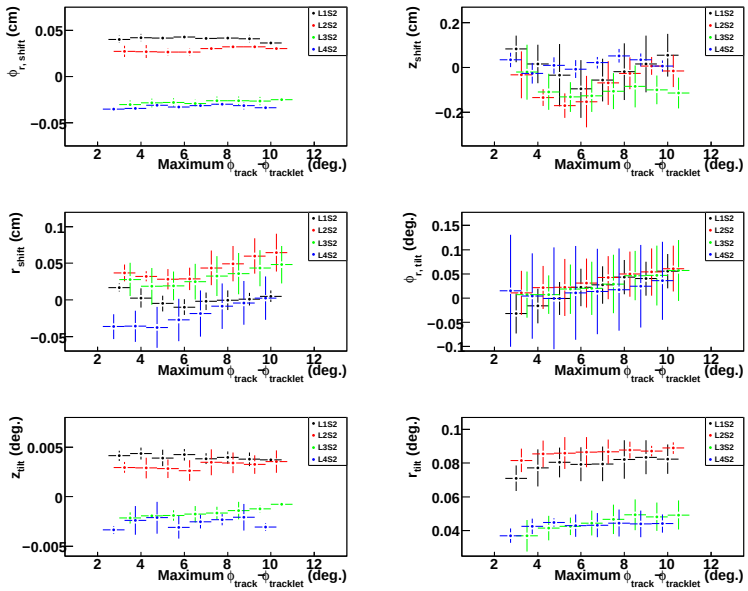

Figure 7.32: All 6 alignment constants as a function of the used data set with a cut on the maximum difference in track angle to tracklet angle for the 4 inner chambers of stack 2. The error bars represent the RMS of 4 measurements.

7.6.7 Final Determination of Number of Tracks

The applied cuts reduce the amount of tracks to just about $\sim 12\,\%$ of the tracks of the start data set. Therefore, it is necessary to recalculate the number of tracks needed for the calculation:

the data set used to evaluate the number of tracks needed for the alignment was corrupted by tracks, which would not pass the cuts described before. Eventually the number of needed tracks is lower for the improved data set. This is tested in a new iteration of the calculation of the used number of tracks. The results are presented in the Figures 7.33 and 7.34. Already with 1500 tracks passing the described cuts, stable results can be provided. This is visible in the distribution of σ and of the alignment constants.
One file of cosmic data in the raw-format with optimized zero suppression contains about 2500 tracks of particles traversing the stack completely for the analysis of the inspected stack. After all cuts almost 300 tracks are left. Thus five files combined to one data set contain enough tracks for the alignment of the TRD chamber of one stack.
This result is valid just for an iteration number of 30. If more or fewer calculations are processed, the number of tracks has to be calculated again for this new approach.

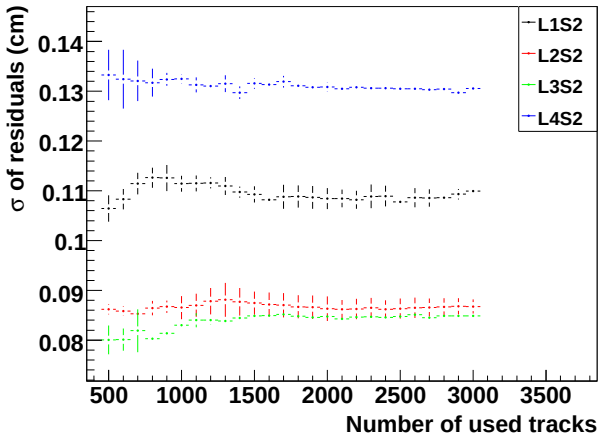

Figure 7.33: All 6 alignment constants as function of the used number of tracks (after adjustment) for the 4 inner chambers of stack 2. The error bars represent the RMS of 4 measurements.

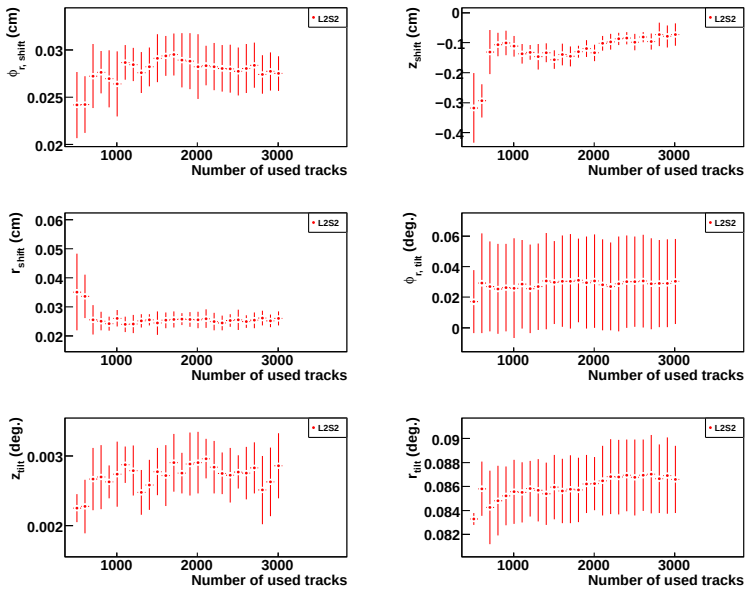

Figure 7.34: Width of residuals as function of the used number of tracks (after adjustment). The error bars represent the RMS of 4 measurements.

7.6.8 Summary of Values for Optimization

The optimized cut values determined in this section are presented in Table 7.3.
In order to improve the quality of the data set for the alignment, four properties of the tracks were investigated as cut values. It is important that no cut should be applied which reduces the ability of alignment with the available data set.
A cut of 6 tracklets were applied. Only with six tracklets per track all chambers have the same amount of track points defining the chamber positions. This cut reduces the amount of tracks to 13 % of the data. A cluster cut is not able to fulfill the condition of defining each chamber with the same amount of track points, while providing more tracks as the tracklet cut. The cluster cut is not applied. For huge data sets, it is possible to add a cut on the number of clusters. Thus, not only the tracks are well defined by 6 tracklets, but also the used tracklets are well defined by many clusters.
The cut on the energy deposit per track, which can be related to a probability of multiple scattering of the particles, is not applied, because an improvement of the y-residuals of 7 % can only be reached by a cut rejecting 25 % of the remaining tracks. The other approach to suppress tracks which are curved by multiple scattering is done via a comparison of the track angle and the tracklet angle. If the difference of both values is too large, the track is rejected. The residuals are 10 % narrower wit a cut to $\Delta\phi = 5°$ while rejecting 8 % of the remaining tracks. In conclusion, about 12 % of the reconstructed tracks are used in the following for the alignment.

Numbers and Cuts	Value	Left Fraction of Data	Reduction of σ_y
Number of Tracks (before)	2000	-	-
Number of iterations	30	-	-
Minimum tracklets number	6	13 %	up to 15 %
(Minimum clusters number)	(75)	(19 %)	-
(Maximum deposited energy)	(10 nADC)	(75 %)	(up to 7 %)
Maximum difference $\Delta\phi$	5°	92 % of 13 % $\approx$ 12 %	up to 10 %
Number of Tracks (after)	1500	-	-

Table 7.3: Evaluated numbers and cuts. The last column represents the reduction of the width of the residuals compared to the previous step of the analysis.

	Chamber 13	Chamber 14	Chamber 15	Chamber 16
Position	sm00/st2/pl10	sm00/st2/pl11	sm00/st2/pl12	sm00/st2/pl13
ID	20482	22530	24578	26626
$\phi_{r,\mathrm{shift}}$(cm)	0.0313±0.0025	0.0136±0.0032	-0.034±0.0030	-0.0347±0.0038
z_{shift}(cm)	-0.1228±0.0189	-0.3478±0.0692	-0.0511±0.1055	-0.1041±0.0331
r_{shift}(cm)	0.0174±0.0052	0.0639±0.0176	0.0948±0.0102	0.0087±0.0206
$\phi_{r,\mathrm{tilt}}$(deg.)	0.0484±0.0077	0.0425±0.0050	0.0489±0.0084	0.0493±0.0157
r_{tilt}(deg.)	0.0032±0.0002	0.0018±0.0007	-0.0014±0.0003	-0.0017±0.0004
r_{tilt}(deg.)	0.0878±0.0058	0.1086±0.0053	0.0706±0.0086	0.0914±0.0061

Table 7.4: Alignment results for stack 2 of super-module III.

7.7 Alignment Results

With the applied cuts, the alignment constants are calculated for all remaining tracks. The 6 values for each of the 4 chambers are shown in Table 7.4. These values, without their error bars, are saved in OCDB as described in Section 7.5.7. In addition, the width of the residuals in y-direction can be determined again. The results for the four chambers are presented in Table 7.5. Moreover, the widths of the residuals before optimization of the data set are presented here.

	Chamber 13	Chamber 14	Chamber 15	Chamber 16
Volume path	sm00/st2/pl10	sm00/st2/pl11	sm00/st2/pl12	sm00/st2/pl13
ID	20482	22530	24578	26626
σ_y(now)(cm)	0.1041±0.0003	0.0819±0.0026	0.0995±0.0036	0.1424±0.0028
σ_y(before)(cm)	0.1230±0.0046	0.0895±0.0026	0.1253±0.0026	0.1532±0.0047
improvement (%)	15.4	8.5	20.6	7.1

Table 7.5: The widths of the residuals calculated for each chamber of stack 2 of super-module III before optimization and after optimization. The improvement in % is presented, too.

7.8 Offline Reconstruction with Corrected Geometry

With the correction of the positioning of the inner chambers of stack 2 added to the OCDB via `AliAlignObjects`, the reconstruction of the previously used run is done again. The performance of the alignment can be tested by comparing the resolution of the detector using the ideal geometry and in comparison the compound of ideal geometry and OCDB information during the reconstruction. Here both entries of the OCDB, the entries calculated without optimized data set and with optimized data set, are used.
The results of all three calculations are shown in Figure 7.35. For all three reconstructed data sets, the cluster resolution in y-direction is calculated. The resolution is better after the alignment of the chambers, even though just the inner chambers of this stack are aligned. Even better is the resolution after optimizing the cuts. The value of σ_y decreases within the two steps, alignment without and with optimization. The distribution of the resolution can be fitted as introduced in Chapter 6.6. The fit to the resolution of tracks at $\phi = 0°$ has a value of $306 \pm 2\,\mu$m for the data without alignment corrections. The fit of the data after alignment shows a minimum at $274 \pm 2\,\mu$m. The fit to the data processed with optimized alignment has a minimum at $249 \pm 3\,\mu$m.
The alignment is successful and increases the resolution of the detector. Optimizing the data set increases the success of the alignment, too.

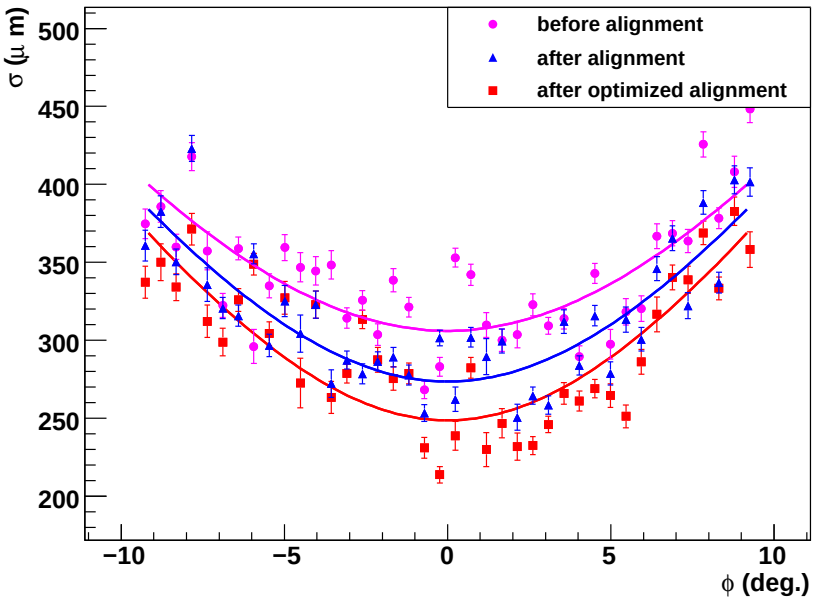

Figure 7.35: The resolution of the tilted pad corrected y-coordinate. The red points are calculated using the ideal geometry. The blue points are calculated with the alignment results stored in the OCDB. The resolution is improved after alignment of the chambers.

7.9 Summary of Alignment and Outlook

In this chapter the alignment of TRD chambers with cosmic ray data has been presented and tested. The alignment is an important calibration step, which is crucial for the detector resolution in position and transverse momentum.
The alignment of the chambers is expressed by shifts and tilts of each chamber in its reference system, which is here the stack. The adjustments are added to the ideal geometry via the OCDB. This results in a geometry that reproduces the real geometry more closely.
Criteria for the data selection were found to improve the results of alignment.
If the alignment constants are saved in the OCDB and are used for the reconstruction of cosmic data, the performance of the alignment can be tested by comparing the resolution of the detector before the alignment and afterwards. The test is successful and shows that the resolution of the detector is about 10 % better with the aligned geometry. After optimization of the data set used for the alignment the resolution is about 19 % better.

So far, the alignment of chambers within the reference system of their stack is realized. In addition, the alignment of stacks to each other with stack-crossing tracks should be added by extending the used procedure.

Fixing the chambers of layer 0 and layer 5 provided a stable reference system, but misalignments of these chambers relative to each other could contaminate the results. First tests with releasing degrees of freedoms for these chambers have started. An optimal alignment of the outer chambers should be achieved that misalignments of the outer chambers to each other do not constrict the proper alignment of the inner chambers.
Correlations between the alignment constants have been observed. Instead of 6 independent alignment constants, two groups of correlated constants were found. This correlations can be used ti fix some constants, reducing calculating time without suppressing physical results.
The alignment correction can be implemented in the `libTRD` which is a database stored in the read-out chambers. With the improved position information stored in the chambers, a improved trigger decision will be provided.
The alignment constants calculated for the Münster setup are used as starting point of the alignment processes with collision data and cosmic data taken at CERN.

8. Summary

The Transition Radiation Detector (TRD) is a central component of the heavy-ion experiment ALICE at the Large Hadron Collider (LHC). The cylindrical detector consists of eighteen super-modules, which undergo final assembly in the institute for nuclear physics at Münster university.
One super-module contains thirty independent detector chambers. As part of the assembly process, tracks of cosmic rays are recorded and reconstructed to perform a first calibration pass.
Due to limited accuracy during assembly and due to time-dependent deformations, the real position of the chambers can differ from their positions in the ideal geometry. In order to minimize the loss of accuracy during conversion of detector signals into spatial positions, the deviations have to be corrected. The detector efficiency and the precision of the reconstructed tracks and vertices are increased by the corrections of this misalignments.
For the purpose of observing the improvement of the combined geometry, a method has been developed to calculate the cluster resolution, which is a measure of correct positioning of the chambers. The data used in this calculation is taken from a so-called debug stream in the recorded data of the reconstruction.
The alignment procedures of the official framework were applied to the data taken in Münster. So-called alignment constants, three for shifting and tilting each, were calculated for the volumes to be aligned. The corrected positions of these volumes were calculated by χ^2-minimization of their position information to a reference fit which is defined by the reference volumes.
Caused by the choice of a reference system for the Münster setup, only the chambers from layer 1 to 4 could be analyzed. The remaining chambers of layer 0 and 5 were fixed and have to be aligned later within ALICE to other tracking devices. As proof of concept, the alignment constants of the inner chambers of stack 2 of super-module III have been calculated.
The alignment framework allows to store the calculated alignment constants in the Offline Conditions Data Base (OCDB). The information of this OCDB and the ideal geometry were combined. The calculated tracking resolution after applying the corrections to the geometry is about 10 % better than it was before.
In order to improve the tracking resolution even more, the data set used for the alignment was optimized by selecting well-defined tracks. The improvement was monitored via the alignment constants and the width of the residuals between the position information of the alignable volumes and the reference fit. Only tracks fulfilling calculated cut values were used for a repeated alignment of the chambers. The resulting tracking resolution is about

19 % better than the resolution for the uncorrected geometry case.
As soon as collision data are available, the calculated alignment constants will be cross checked and will be updated. In addition, the alignment constants of the chambers in layer 0 and layer 5 need to be calculated.

Danksagung

Abschließend möchte ich allen herzlich danken, die zum Gelingen dieser Arbeit beigetragen haben.
Allen voran danke ich Herrn Prof. Dr. J. P. Wessels für die Aufnahme in die Arbeitsgruppe, für das spannende Thema, die Möglichkeit an Konferenzen teilzunehmen und spannende Reisen zu den Forschungszentren CERN und GSI zu unternehmen.
Weiterhin gilt mein großer Dank Dr. Thomas Dietel, der mich während meiner Diplomarbeit immer unterstützt hat, mir viel beigebracht hat und geduldig für alle Fragen offen war.
Dr. Dariusz Miskowiec vom Forschungszentrum GSI in Darmstadt danke ich für die vielen Erklärungen und die schöne Zusammenarbeit zum Thema *Alignment*.
Dr. Alexandru Bercuci und Markus Fasel (GSI) danke ich für die Zeit, in der sie mir das *Stand-Alone Tracking* in AliRoot erklärt haben.
Den Technikern des Instituts Wolfgang Verhöven, Nobert Heine und Helmut Baumeister danke ich für die Anleitung in technischen Fragen.
Für das Korrekturlesen meiner Arbeit danke ich Dr. Thomas Dietel, Dr. Christian Klein-Bösing, Dr. Dariusz Miskowiec, Baldo Sahlmüller, Alexander Wilk, Christoph Baumann, Melanie Klein-Bösing, Bastian Bathen, Markus Fasel, Dr. Matus Kalisky, Maria Bregen-Meiners, Cornelia Petrovic und Henriette Gatz. Meiner ganzen Arbeitsgruppe danke ich für die tolle Arbeitsatmosphäre. Für die gute Zusammenarbeit beim Supermodul-Bau danke ich Dr. Thomas Dietel, Helge Grimm, Uwe Westerhoff und Svenja Wulff.
Meinen Bürokollegen Robert Lüchtenborg, Ansgar Kumpmann, Stefan Korsten, Michal Kowalik und Sebastian Klamor danke ich für die gute Stimmung und die freundschaftliche Hilfe. Meiner Bürokollegin und Mitstreiterin Svenja Wulff möchte ich besonders danken: Es hat Spaß gemacht mit dir gemeinsam die Diplomarbeit zu bewältigen.
Für ein gute Zeit im Studium möchte ich meinen Kommilitonen danken: Irina, Clemens, Felix, Johannes, Florian, Markus, Henrik, Henriette und Connie, danke!
Meinem Physiklehrer Carl-Wilhelm Burges-Hohenschwert danke ich für den tollen Physikunterricht, der mein Interesse an der Physik bestärkt hat.
Meinen Freunden aus Gescher, besonders Caroline, Katrin, Thekla, Theresia, Anne, Angela, Michael, Henrik, Stefan und Anne-Katrin sowie meinen Mitbewohnerinnen und Mit-

bewohnern möchte ich für die schöne Zeit danken, die wir in den letzten Jahren verlebt haben.
Danke an Tobias.
Meiner Mutter Edith, meinem Vater Willi und meinen Schwestern Kerstin und Annegret danke ich für den vielen Zuspruch. Meinen Eltern danke ich, dass sie mir das Studium ermöglicht haben und volles Vertrauen in mich gesetzt haben.

Bibliography

[Abr00] M. Abreu *et al. Physics Letters B* **477**.

[Adc05] K. Adcox *et al. Nuclear Physics A* **757** (2005) 184.

[Adl04] C. Adler *et al. Nuclear Instruments and Methodes in Physics Research A* **540** (2004) 140.

[ALI09] http://aliceinfo.cern.ch/, 2009.

[ALN09] http://pcaliweb02.cern.ch/Offline/Activities/Alignment.html, 2009.

[Ams08] C. Amsler *et al. Physics Letters B* **667**.

[And04] A. Andronic. *Nuclear Instruments and Methodes* **522** (2004) 40.

[Bat07] B. Bathen. diploma thesis, 2007.

[Bel04] I. Belikov *et al. Computing in High Energy Physics and Nuclear Physics* (2004) 399.

[Ber09] A. Bercuci. personal communications, 2009.

[CDS09] cdsweb.cern.ch, 2009.

[Eck05] V. Eckardt *et al. Physik Unserer Zeit* **3** (2005) 126.

[Fas08] M. Fasel. *Stand-alone tracking in the ALICE Transition Radiation Detector.* Project Proposal, 2008.

[Gre66] K. Greisen. *Physical Review Letters* **16** (1966) 748.

[Gri09] H. Grimm. diploma thesis, 2009.

[Hop04] M. Hoppe. diploma thesis, 2004.

[Hri06] P. Hristov. *AliRoot Primer.* CERN, 2006.

[LHC08] *LHC, the guide.* CERN, 2008.

[Mat86] T. Matsui *et al. Physics Letters B* **178**.

[Mis07] D. Miskowiec. *TRD Alignment with AliAlignmentTracks*. Talk at ALICE Offline Week, 2007.

[Mis08] D. Miskowiec. *TRD Alignment with Muenster Cosmics*. Talk at TRD status meeting, 2008.

[MK02] T. Mayer-Kuckuk. *Kernphysik - Eine Einführung*. B. G. Teubner GmbH, Stuttgart, 2002.

[Mys09] http://www.mysql.com, 2009.

[OCD09] http://aliceinfo.cern.ch/Offline/Activities/ConditionDB.html, 2009.

[Ora09] http://www.oracle.com/index.html, 2009.

[PIH09] http://www.physi.uni-heidelberg.de/Galerie/allpics.php, 2009.

[Pov04] B. Povh *et al. Teilchen und Kerne*. Springer-Verlag Berlin Heidelberg, 2004.

[PPR04] *ALICE: Physics Performance Report, Volume I+II*. CERN, 2004.

[Sta07] J. Stachel *et al. Nature* **448** (2007) 302.

[TP108] *ALICE Technical Paper I - 2008*. CERN, 2008.

[TRD99] *A Transition Radiation Detector for Electron Identification with the ALICE Central Detector*. CERN, 1999.

[TRD01] *ALICE - Technical Design Report of the Transition Radiation Detector*. CERN, 2001.

[Web96] H. Weber. http://th.physik.uni-frankfurt.de/ weber/, 1996.

[Wil06] A. Wilk. *Nuclear Instruments and Methodes* **A563** (2006) 314.

[Wul09] S. Wulff. diploma thesis, 2009.

Eigenständigkeitserklärung

Ich versichere, diese Arbeit selbständig verfasst und keine anderen als die angegebenen Hilfsmittel und Quellen benutzt zu haben.

Münster, 16. Februar 2009

Eva Sicking